

DISSERTATION

CHARACTERISTICS OF CURRENT AND FUTURE FLOOD-PRODUCING STORMS IN
THE CONTINENTAL UNITED STATES

Submitted by

Erin M. Dougherty

Department of Atmospheric Science

In partial fulfillment of the requirements

For the Degree of Doctor of Philosophy

Colorado State University

Fort Collins, Colorado

Summer 2020

Doctoral Committee:

Advisor: Kristen Rasmussen

Russ Schumacher

Eric Maloney

Ryan Morrison

Copyright by Erin Dougherty 2020

All Rights Reserved

ABSTRACT

CHARACTERISTICS OF CURRENT AND FUTURE FLOOD-PRODUCING STORMS IN THE CONTINENTAL UNITED STATES

Understanding the changes to extremes in the hydrologic cycle in a future, warmer climate is important for better managing water resources and preventing detrimental impacts to society. The goal of this dissertation is to contribute to this understanding by examining the precipitation characteristics of flood-producing storms in the current climate over the continental United States (CONUS) and how these will change in a future, warmer climate. Numerous storm types are responsible for floods over the CONUS, so quantifying how their characteristics will change among a large number of flood-producing storms in the future provides a spectrum of possible changes and impacts to flood-prone regions across the country.

To understand flood-producing storms in the current climate over the CONUS, a climatology of these storms from 2002–2013 is created by merging storm reports, streamflow-indicated floods, and Stage-IV precipitation data (Chapter 2). From this climatology, it is observed that flash flood-producing storms preferentially occur in the warm-season in the Mississippi River Basin, with intense rain rates and short durations. Slow-rise floods occur mostly during the cool-season, concentrated in the Ohio River Valley and Pacific Northwest, and are long-duration, low-intensity rainfall events. Hybrid floods, having characteristics of both flash and slow-rise flood-producing storms, tend to occur in the spring and summer notably in the central CONUS and Northeast, with moderate durations and rain rates. Examining these floods on a sub-basin scale in the Wabash and Willamette basins, precipitation and instantaneous streamflow correlations are spatially variable, with strong positive correlations in areas of complex terrain and urbanization (Chapter 3). These studies show that in the current climate, flood-producing storm precipitation characteristics and

their hydrologic response is nuanced, which is critical to document in order to understand their behavior in a future climate.

A subset of nearly 600 flash flood-producing storms from the Chapter 2 climatology are examined using high-resolution convection-permitting simulations over the CONUS to understand how these historical storms might change in a future, warmer climate (Chapter 4). Both precipitation and runoff show widespread increases in the future over the CONUS, increasing by 21% and 50%, respectively, with maximum hourly rain rates becoming more intense by $7.5\% \text{ K}^{-1}$. In California, 45 flood-producing storms associated with atmospheric rivers also display a future increase (decrease) in precipitation (snow water equivalent) leading to increased runoff, particularly over the Sierra Nevada Mountains, implying a shift in future water resources in California (Chapter 5). In the Mississippi River Basin—a flash flood hotspot in the CONUS—nearly 500 flash flood-producing storms exhibit a 17% average increase in precipitation and 32% average increase in runoff primarily associated with warm-season convection, and to a lesser extent, tropical cyclones (Chapter 6). When stratified by vertical velocity, the storms with the strongest vertical velocity in the current climate exhibit the greatest (least) increase (decrease) in future rainfall (vertical velocity), suggesting a potential role of storm dynamics in modulating future rainfall changes.

ACKNOWLEDGEMENTS

I owe a great deal of thanks and gratitude to my advisor, Dr. Kristen Rasmussen, who has supported me in every aspect during my graduate career. Without your career and life advice, along with the endless opportunities for growth you provided, I would not have enjoyed or learned so much during my Ph.D. I will miss our long research conversations, as they always left me re-inspired about research!

I would like to thank my Ph.D. committee members, Dr. Russ Schumacher, Dr. Eric Maloney, and Dr. Ryan Morrison, for your insightful feedback and helpful guidance—I have learned so much from each of you over the years. A special thanks goes out to Dr. Morrison for collaborating on the CSU Water Center project in an interdisciplinary team and for your hydrologic expertise. I would also like to thank those who made contributions to this dissertation with their helpful discussions and providing additional data, including Dr. Roy Rasmussen, Dr. Andreas Prein, Dr. Andrew Newman, and Kyoko Ikeda from NCAR.

Thank you to my lab group, both past and former, for the countless scientific discussions and feedback. A special thanks to Jeremiah Piersante and Zach Bruick for geeking out about storms with me, for your friendship, and making the third floor fun. To the rest of the graduate students in the department—a huge thank you for the incredible support and for all the amazing adventures. You all have easily made my time at CSU some of the best years I will look fondly back upon, and continually inspire me to be a better person and scientist.

I would like to thank those before my time at CSU as well, including Dr. Kristen Corbosiero and Dr. John Molinari. Thank you for the mentorship during my M.S. at University at Albany and supporting my change in educational plans. In addition to being great scientists, you are great people who have constantly supported me through my academic career.

I would also not be where I am without my SOARS family, so thank you to Rebecca Haccker, Dr. Rebecca Batchelor, and the past and present cohort. This group inspired me to go to graduate school, supported me throughout this journey, and have provided lifelong friendships.

Lastly, I am deeply grateful for my friends and family, for all their love and continually believing in me. A special thanks goes out to Kelsey Everard for commiserating over graduate school with me and for all the outdoor adventures. To my running friends, thank you for keeping me sane during this marathon that is graduate school and always reminding me of the life outside graduate school. To Dr. Andrew Winters, thank you for your unconditional love, support, and understanding. Finally, to my family, thank you for encouraging me to be continually curious, hungry to learn, and supporting all my crazy dreams.

This research was supported in part by Colorado State University Water Center grant #130116. Additional support for this research was also made possible from the Cheyenne supercomputer, the Pangeo community platform (pangeo.io/index.html), NCEI Storm Events data (<https://www.ncdc.noaa.gov/stormevents/>), Stage-IV precipitation data (<https://data.eol.ucar.edu/dataset/21.093>), and the CONUS PGW convection-permitting simulations (<https://rda.ucar.edu/datasets/ds612.0/>) run by the Research Applications Lab (RAL) at NCAR.

DEDICATION

To my parents, for imparting their love of learning on me.

TABLE OF CONTENTS

ABSTRACT	ii
ACKNOWLEDGEMENTS	iv
DEDICATION	vi
LIST OF TABLES	ix
LIST OF FIGURES	xi
Chapter 1	Introduction 1
1.1	Motivation 1
1.2	Dissertation outline 3
Chapter 2	Climatology of Flood-Producing Storms and Their Associated Rainfall Char- acteristics in the United States 6
2.1	Introduction 6
2.2	Data and methods 11
2.2.1	<i>NCEI Storm Events Database</i> 11
2.2.2	<i>Merging storm reports with the Shen et al. (2017) database</i> 13
2.2.3	<i>Stage IV precipitation data</i> 15
2.3	Results 17
2.3.1	<i>Seasonal and geographical distribution of floods</i> 17
2.3.2	<i>Rainfall characteristics of flood-producing storms</i> 25
2.3.3	<i>Comparison of rainfall characteristics in flood-producing storms</i> 29
2.4	Conclusions 32
Chapter 3	The Role of Precipitation in Flood Occurrence and Distribution in Topo- graphically Variable Basins 36
3.1	Introduction 36
3.2	Methods 38
3.2.1	<i>Flood data</i> 38
3.2.2	<i>Description of river basins</i> 39
3.3	Results 41
3.3.1	<i>Flood rainfall and streamflow in the Wabash Basin</i> 41
3.3.2	<i>Flood rainfall and streamflow in the Willamette Basin</i> 44
3.4	Discussion 47
3.5	Conclusions 50
Chapter 4	Changes in Future Flash Flood-Producing Storms in the U.S. 51
4.1	Introduction 51
4.2	Data and Methods 53
4.2.1	<i>Convection-Permitting Simulations</i> 53
4.2.2	<i>Flash flood cases</i> 57
4.2.3	<i>Comparison of observed and simulated flood rainfall</i> 59

4.2.4	<i>CTRL and PGW synoptic conditions in the Arkansas flash flood of 2008</i>	64
4.2.5	<i>Flash flood storm calculations</i>	65
4.3	Results	68
4.4	Conclusions	77
Chapter 5	Future Changes in the Hydrologic Cycle Associated with Flood-Producing Storms in California	80
5.1	Introduction	80
5.2	Data and Methods	84
5.2.1	<i>Convection-permitting simulations</i>	84
5.2.2	<i>Cool-season climatology</i>	87
5.2.3	<i>Cool-season floods</i>	87
5.3	Results	91
5.3.1	<i>Cool-season climatology</i>	91
5.3.2	<i>Cool-season flood-producing storms</i>	97
5.4	Conclusions	102
Chapter 6	Flash Flood-Producing Storms in a Current and Future Climate in the Mississippi River Basin	105
6.1	Introduction	105
6.2	Data and Methods	108
6.2.1	<i>Convection-permitting simulations</i>	108
6.2.2	<i>Flash flood cases</i>	111
6.2.3	<i>Identification of tropical cyclone-related floods</i>	113
6.2.4	<i>Categorization of flash flood convective strength</i>	116
6.3	Results	118
6.3.1	<i>Future changes in all flash flood-producing storms</i>	118
6.3.2	<i>Future changes in flash flood-producing storms by convective strength</i>	125
6.4	Conclusions	132
Chapter 7	Conclusions	135

LIST OF TABLES

2.1	The number of flash, slow-rise, and hybrid flood-producing storms for events (episodes) in the NCEI Storm Event Database in the left (right) column that match flooded stream gauge locations from the Shen et al. (2017) database. The row labeled “all” is the sum of flood episodes for all flood types.	13
2.2	Percentage of flood causes comprising each type of flood, where boldface values indicate the largest percentage and italic values indicate the second largest percentage. Flood causes only include post-2006 NCEI Storm Events data and exclude missing data from the calculation.	19
2.3	Seasonality of long-duration (>250 h) slow-rise flood causes in the northern Great Plains and lower Mississippi Valley for causes that comprise over 25% of the total. The peak season for each flood cause in each region is bolded.	28
4.1	Mean values of flash flood area-averaged rainfall, maximum hourly rain rate, duration, area, and runoff in a current (CTRL) and future (PGW) climate, the difference (PGW-CTRL), percent change (% change), and percent change per degree of warming (% K^{-1}) in a future climate. Values in the parentheses indicate the 95% confidence interval (CI) of the mean values for % change and % K^{-1} after bootstrapping.	60
5.1	Future percent change in precipitation, snow water equivalent (SWE), and runoff in 45 flood-producing storms in California from 2002–2013. The future percent change is $PGW-CTRL/CTRL * 100$ in different California regions (North, Central, South). . . .	98
5.2	As in Table 5.1, but for the raw future change (PGW–CTRL) in temperature, precipitation, SWE, and runoff.	99
6.1	Names and years of hurricanes that were associated with flash flood events in the Mississippi River Basin from the Chapter 2 climatology. The number of unique flood events associated with the hurricane is shown, as well as an indication if the CTRL simulations of the hurricane compared well to both observations from the Extended Best Track dataset and PGW simulations.	116
6.2	Mean values of rainfall characteristics for all 484 flash flood-producing storms in the Mississippi River basin for CTRL and PGW simulations, the future difference (PGW-CTRL), future percent difference (% change), and future percent difference per degree of warming (% change K^{-1}). Also shown is the % change K^{-1} for storms with the highest and lowest area-average rainfall accumulation (top 25% and lowest 25%, respectively; last two columns).	121
6.3	As in Table 6.2, but only for flash flood-producing storms associated with the hurricanes listed in Table 6.1 (n=19).	124

6.4 Percent future change ($(PGW-CTRL/CTRL)*100$) in storm characteristics among three different categories of average (temporal and spatial) vertical velocity (w) in flash flood-producing storms in the Mississippi River basin. Weak storms have average vertical velocities $<0.03 \text{ ms}^{-1}$, 0.03 ms^{-1} < moderate $<0.06 \text{ ms}^{-1}$ and strong $>0.06 \text{ ms}^{-1}$. Values in parentheses show the future % change per degree of warming and bold numbers indicate the maximum value for each variable. 126

6.5 As in Table 6.4, except for changes in updraft and downdraft characteristics. 126

LIST OF FIGURES

2.1	An example of the methodology used to identify flood-producing storm rainfall from Stage IV rainfall data. A flash flood in Virginia occurred from 0300 to 1600 UTC 7 Oct 2006, with its flood centroid shown by the star, flooded stream gauges from the Shen et al. (2017) database in red dots, and largest contiguous area of Stage IV accumulated precipitation (shaded; mm) over the 75th percentile outlined in black, as identified from an object-identifier tool in Python.	17
2.2	Number of flood episodes per month summed from 2002 to 2013, where cyan represents flash floods, dark blue represents hybrid, and gray represents slow-rise floods. . .	18
2.3	Number of flash flood events per state (fill; normalized by state area) and locations of USGS gauge-indicated floods from the Shen et al. (2017) database (black dots) over the CONUS from 2002 to 2013 for (a) winter (DJF), (b) spring (MAM), (c) summer (JJA), and (d) fall (SON).	21
2.4	As in Figure 2.3, but for slow-rise floods.	22
2.5	As in Figure 2.3, but for hybrid floods.	23
2.6	Number of (a) flash, (b) slow-rise, and (c) hybrid flood events per state (fill; normalized by state area) and locations of USGS gauge-indicated floods from the Shen et al. (2017) database (black dots) over the CONUS from 2002 to 2013.	24
2.7	Flash flood (a) episode count, (b) average rain accumulation, (c) average area, and (d) average duration (h) per Stage IV grid cell from 2002 to 2013. Values in (a)–(c) are on logarithmic scales, while those in (b) and (c) have been normalized by a scaling factor (number of flood events in Stage IV grid cell/total number of flood events).	26
2.8	As in Figure 2.7 but for slow-rise floods.	27
2.9	Cause of long-duration (> 250 h) slow-rise floods in the (a) northern Great Plains (n=82) and (b) lower Mississippi Valley (n=23) from post-2006 NCEI Storm Events data. The size of different colors in the circle shows the percentage of each flood cause (green= heavy rain, blue=heavy rain on snowmelt, purple=ice jam, orange= dam release, and red=heavy rain over burn area).	28
2.10	As in Figure 2.7 but for hybrid floods.	29
2.11	Boxplots of (a) rainfall accumulation normalized by flood area (mm km^{-2}), (b) maximum rain rate (mm h^{-1}), (c) flood duration (h), and (d) flood area (km^2) for flash (red box), slow-rise (cyan box), and hybrid flood episodes (purple box). Black dots indicate outliers.	31
2.12	Average rain rate (mm h^{-1}) as a function of the log of duration (h) for flash (red dots), slow-rise (blue dots), and hybrid (purple dots) floods, where the size of the dot represents the area of the flood.	32
3.1	The two basins used for analysis in study. The Willamette basin (a) is located in Oregon, next to the Coastal (Cascade) Mountains to the west (east) and is characteristic of the Pacific Northwest (black outline). The Wabash basin (b) is located in Indiana and parts of Illinois and Ohio and is characteristic of a relatively flat river basin in the Midwest (black outline).	40

3.2	a) Seasonality of flash (red) and slow-rise (blue) floods in the Wabash basin by month. b) as in a), but for the Willamette basin. Floods are identified using a flood database from Chapter 2.	40
3.3	a) Number of flash flood episodes in the Wabash basin. b) Average flash flood rainfall in the Wabash basin. c) and d), as in a) and b), respectively, except for slow-rise floods. Black dots show average flood discharge (normalized by catchment area), where larger dots = higher discharge ($\text{m}^3 \text{s}^{-1} \text{km}^{-2}$). The black arrow shows the general north-to-south direction of river flow.	42
3.4	Correlation matrix of flood frequency (rain_ct), gauge elevation (elevation), flood average discharge (discharge), and flood average rainfall (rain) averaged across the entire Wabash basin for a) flash floods and b) slow-rise floods.	44
3.5	Correlation between average discharge and average rainfall at each stream gauge for a) flash floods, and b) slow-rise floods. Blue lines depict major rivers, while grey contours depict topography (darker contours=higher topography).	44
3.6	a) Number of slow-rise flood episodes in the Willamette basin. b) Average slow-rise flood rainfall in the Willamette basin. Black dots show average flood discharge (normalized by catchment area), where larger dots = higher discharge ($\text{m}^3 \text{s}^{-1} \text{km}^{-2}$). The black arrow shows the general south-to-north direction of river flow.	45
3.7	As in Figure 3.4, but for the Willamette basin.	46
3.8	Correlation between average discharge and average rainfall at each stream gauge for slow-rise floods. Blue lines depict major rivers, grey contours depict topography (darker contours=higher topography), and grey triangles show dams > 30 m height, where the size of the triangles indicate the relative dam height	47
4.1	Elevation (m) over the domain of the 4-km convection-permitting simulations described by Liu et al. (2017) used in this study. While parts of Canada and Mexico are included in this domain, the present study focuses only on the continental United States.	54
4.2	Seasonality of the most intense flash flood-producing storms in the continental United States from 2002–2013.	58
4.3	Histogram of differences between simulated (CTRL) and observed (Stage-IV) rainfall a) duration (h), b) duration (%), c) area-averaged rainfall (mm), and d) area-averaged rainfall (%) in the top 25% most intense flash flood-producing storm over the U.S. The left column (a and c; blue coloring) shows the absolute difference, while the right column (b and d; red coloring) shows the percent difference. A positive difference indicates that CTRL data overestimates flash flood duration or rainfall.	59
4.4	Total accumulated rainfall (mm) for a flash flood-producing storm in the south-central U.S. that occurred from 07 UTC 01 May–21 UTC 02 May 2011, in a) the full Stage-IV data, b) Stage-IV without the erroneous rainfall data, c) CTRL, and d) PGW simulations. In a), the erroneous rainfall data in the northeast part of the domain aligns with a river forecast boundary line (not shown).	61
4.5	Probability density function of the structural similarity index (Wang et al., 2004) between Stage-IV and CTRL (grey) and CTRL and PGW (red) flash flood accumulated rainfall in 584 flash flood-producing storms over the continental U.S. A value closer to 1 indicates greater similarity.	63

4.6	Flash flood accumulated rainfall in a) CTRL simulations and b) PGW simulations for a flood that occurred in eastern Texas, with the flood centroid shown by the black star. This flash flood had the lowest structural similarity index of all flash floods between the CTRL and PGW simulations of 0.66.	63
4.7	Flash flood accumulated rainfall from 02–16 UTC 03 March 2008 in a) CTRL simulations and b) PGW simulations for the Arkansas floods of 2008.	65
4.8	F500 hPa geopotential height (blue contours; m) and winds (barbs; each half barb=5 kts, full barb=10 kts, and flags=50 kts) for a) CTRL simulations and b) PGW simulations, as well as mean sea-level pressure (black contours), 10 meter winds (barbs), and precipitable water (mm; shading) in c) CTRL simulations and d) PGW simulations at 00 UTC 03 March 2008. The orange star indicates the flood centroid of the Arkansas floods of 2008.	66
4.9	Occurrence of flash flood-producing storms in the a) CTRL simulations and b) PGW simulations, where darker colors indicate a higher occurrence of flash flood rainfall. Areas without shading do not indicate a lack of flash flood-producing storms in that region, but rather that the top 25% of flash flood-producing storms do not occur in that region. Note that the distribution of storms is similar in the CTRL and PGW simulations.	68
4.10	Amount of rainfall per flash flood-producing storm (mm storm^{-1}) for 584 storms in a) CTRL simulations, b) PGW simulations, and c) the PGW-CTRL difference where blue (red) represents an increase (decreases) in future rainfall per storm.	69
4.11	As in Figure 4.10 but for flash flood runoff (mm storm^{-1}).	70
4.12	The percent future change in a) area-averaged flash flood rainfall and b) runoff, separated by region. West is west of -103°W (or west of Texas), Central is from -103° to -87°W (roughly from Texas to Illinois), and East is east of -87°W (roughly east of Illinois). Boxes show the interquartile range (IQR; first (Q1) through third (Q3) quartile, or 25th–75th percentile), whiskers denote the “minimum” ($Q1-1.5*IQR$) and “maximum” ($Q3 + 1.5*IQR$), and diamonds indicate outliers. Notched lines in the middle of the box indicate the median value, with the size of the notches showing the 95% confidence interval. A positive percent change (i.e., above the dashed horizontal line at zero) indicates a future increase in rainfall or runoff.	72
4.13	As in Figure 4.12, except for the change in runoff efficiency (runoff/precipitation), where values above the dashed line at 1 indicate a future increase in runoff efficiency (increases in runoff exceed increases in precipitation), values between 0 and 1 indicate a future decrease in runoff efficiency (increases in precipitation exceed increases in runoff), and values below 0 indicate a decrease in either future runoff or precipitation.	73
4.14	Probability distribution function of a) maximum hourly rain rates (mm h^{-1}) in CTRL (blue) and PGW (red) flash flood-producing storms, b) the percent change per Kelvin ($\% \text{ change K}^{-1}$) in maximum hourly rain rates of PGW flash-flood producing storms compared to CTRL. The dotted line is located at 0 to distinguish between the future percent increase and decrease per Kelvin.	75
4.15	As in Figure 4.14, except for the area (km^2) of flash flood-producing storms.	76
4.16	The future change in temperature (K) versus the future change in area (%) in flash flood-producing storms, where the vertical (horizontal) line denotes zero to show where future increases in temperature (area) occur.	76

4.17	Composite area-averaged rainfall accumulations in all 584 flash flood-producing storms averaged in CTRL simulations (left) and PGW simulations (right). The x and y-axes are arbitrary and provide the size of the rainfall (km).	79
5.1	The study domain over California and its elevation to highlight the complex terrain. Also shown are boxes around three different regions in California—Northern California (purple), Central California (red), and Southern California (pink).	84
5.2	Probability density function of the structural similarity index from Wang et al. (2004) used to compute the structural differences in rainfall accumulation among 45 cool-season floods in California in CTRL vs. PGW simulations. The mean value is indicated by the dashed vertical line.	90
5.3	The accumulated rainfall in a) CTRL simulations and b) PGW simulations for a slow-rise flood that occurred from 0000–2200 UTC 20 January 2010. This flood had the lowest structural similarity index among all 45 cool-season floods in California of 0.88.	90
5.4	Average cool-season (October–April) precipitation over California in a) CTRL simulations, b) PGW simulations, and c) PGW-CTRL difference, where blue indicates increased PGW precipitation and red indicates a decrease.	92
5.5	As in Figure 5.4, but for snow water equivalent (SWE).	93
5.6	As in Figure 5.4, but for runoff.	94
5.7	PGW–CTRL difference in cool-season precipitation, runoff, and SWE shown in Figure 5.4–Figure 5.6, as a function of altitude over California.	96
5.8	Seasonality from October–May of percent future change in precipitation (turquoise), SWE (purple), and runoff (green). The dashed line at zero indicates no change, while values above (below) the line indicate a future percent increase (decrease). Note that the percent change is computed as $PGW-CTRL/CTRL * 100$	97
5.9	As in Figure 5.4, but for average precipitation in 45 cool-season flood-producing storms in California between 2002–2013.	98
5.10	As in Figure 5.5, but for average SWE in 45 cool-season flood-producing storms in California between 2002–2013.	100
5.11	As in Figure 5.6, but for average runoff in 45 cool-season flood-producing storms in California between 2002–2013.	101
5.12	PGW-CTRL differences in precipitation (red dots) and SWE (blue dots) 45 flood-producing storms in California as a function of altitude. Turquoise (dark blue) colored-dots indicate SWE changes in storms where the temperature is below (above) freezing (273 K) in the PGW simulations.	101
5.13	As in Figure 5.11, but for integrated water vapor transport (IVT).	102
6.1	Location of 484 flash flood-producing storms (white circles) in the Mississippi River Basin from 2002–2013 identified by Chapter 2 from a combination of NCEI storm reports, flooded stream gauges from Shen et al. (2017), and Stage-IV precipitation data. The Mississippi River and its major tributaries are indicated by the thick black lines, while shading shows elevation.	113
6.2	The seasonality of flash flood-producing storms shown in Figure 6.1.	114

6.3	Example of the methodology used to classify a flash flood-producing storm as having a tropical storm influence. In this case, the domain of a flash flood-producing storm is outlined by the red box, while the 34-kt wind radii (storm center) of Hurricane Katrina (2005) are shown by the turquoise ellipses (black dots). Any flash flood-producing storm, such as this example, where the 34-kt wind radii intersects the flood domain <24 h prior to the flood was classified as having a tropical influence.	115
6.4	Distribution of the spatially and temporally averaged vertical velocity (w) within the heavy rainfall region of flash flood-producing storms in the Mississippi River Basin. Weakly forced flash flood producing storms have their average $w < 0.03 \text{ m s}^{-1}$, moderately forced $>0.03 \text{ m s}^{-1}$ and $<0.06 \text{ m s}^{-1}$, and strongly forced storms $>0.06 \text{ m s}^{-1}$	118
6.5	Distribution of the occurrence of flash flood-producing storm precipitation in the a) CTRL simulations and b) the PGW simulations.	119
6.6	Rainfall per flash flood-producing storm (mm storm^{-1}) in the a) CTRL simulations, b) PGW simulations, and c) PGW-CTRL difference, where blue (red) indicates a future increase (decrease) in mm storm^{-1}	120
6.7	As in Figure 6.6, but for runoff per storm.	122
6.8	As in Figure 6.5, but only for flash flood-producing storms with a tropical storm influence.	123
6.9	As in Figure 6.6, but only for flash flood-producing storms with a tropical storm influence.	123
6.10	Boxplots of average vertical velocity (w) in weak (blue), moderate (purple), and strong (red) flash flood-producing storms. Boxes with lighter (darker) shades indicate storms in the CTRL (PGW) simulations.	125
6.11	As in Figure 6.10, but for maximum instantaneous vertical velocity.	127
6.12	As in Figure 6.10, except for spatially and temporally averaged updrafts (defined as $w > 1 \text{ m s}^{-1}$, above the dashed line) and downdrafts ($w < -1 \text{ m s}^{-1}$, below the dashed line).	128
6.13	As in Figure 6.10, but for area-averaged rainfall.	129
6.14	As in Figure 6.10, but for volumetric rainfall.	129
6.15	PDF of the future (PGW-CTRL) change in a) average vertical velocity (w ; m s^{-1}) and b) area-average rainfall (%) in weak (blue), moderate (purple), and strong (red) flash flood-producing storms. The dashed line at zero distinguishes a future increase/decrease in (w) and rain, with anything to the right of the zero line indicating a future increase. Colored dashed lines indicate the median of the distribution.	130

Chapter 1

Introduction

1.1 Motivation

Extremes in the hydrologic cycle cause massive disruptions to society resulting in economic loss, damage to infrastructure, and loss of human life. Floods are one extreme that pose a substantial risk to the continental United States (CONUS), with an estimated 41 million people and \$2.9 trillion of gross domestic product exposed to a 1-in-100-year flood in 2010 (Wing et al., 2018). Historically, floods have accounted for over \$123.5 billion in adjusted losses between 1980–2018 (A. B. Smith, 2019). Due to their complex nature requiring interactions between atmospheric, hydrologic, and land-surface processes, forecasting floods remains extremely challenging (J. M. Fritsch & Carbone, 2004; Herman & Schumacher, 2018a; Sukovich et al., 2014). Conditions such as antecedent soil moisture, soil type, topography, land-use, atmospheric moisture, and storm characteristics all must be considered when predicting or analyzing such events (Berghuijs et al., 2016; Davis, 2001; Kumar et al., 2014; Saharia et al., 2017a; A. Schroeder et al., 2016b). However, precipitation is a major contributor to floods, with forecasters relying on precipitation and other key atmospheric variables to predict these events (Davis, 2001; Doswell et al., 1996; A. J. Schroeder et al., 2016a).

A key step toward improving the predictability of extreme rainfall and flooding was led by Maddox et al. (1980, 1979), who used pattern recognition of synoptic regimes associated with floods in the CONUS. Flash floods were classified based on their association with four common atmospheric patterns—synoptic, frontal, mesohigh, and Western events. The Western events were further broken down into four categories—Type I and Type II events associated with a 500 mb short-wave trough embedded in a longwave ridge, Type III events with strong synoptic forcing and stable airmasses characteristic of atmospheric rivers, and Type IV events characteristic of the Southwest monsoon (Maddox et al., 1980). Doswell et al. (1996) expanded upon the work by Maddox et al.

(1980, 1979) to show that certain atmospheric “ingredients” are useful for forecasting flash floods. These ingredients are represented by the following equation:

$$P = \bar{R}D \quad (1.1)$$

Where P is rainfall accumulation, \bar{R} is the average rain rate, and D is the rainfall duration. Based upon Eqn. 1.1, factors that maximize rain rates or durations lead to heavy rainfall. High rain rates are maximized due to high precipitation efficiency, ample moisture, and sustained lift, while long duration rainfall is promoted by slow system movement or repeated initiation of convective cells upstream of their predecessors (or “backbuilding”; Schumacher & Johnson, 2005). Recent floods in the CONUS exemplify the importance of these ingredients manifest in various ways. In the Colorado floods of 2013, stationary synoptic conditions resulted in a persistent cutoff low-pressure system that allowed for continual easterly (upslope) flow of anomalous moisture up the Rocky Mountains and nearly a week of heavy rainfall (Gochis et al., 2015). Several cases of extreme rainfall and flash flooding in the central CONUS were associated with quasi-stationary mesoscale convective systems (MCSs) that persisted due to continual lift from a mesoscale convective vortex interacting with a low-level jet and the reversal of wind shear with height (Schumacher, 2009; Schumacher & Johnson, 2008, 2009).

Studies using high-resolution convection-permitting simulations show that this key ingredient in floods—heavy precipitation—will change in a future, warmer climate. Future convective storms (K. L. Rasmussen et al., 2017), MCSs (Prein et al., 2017b, 2017c), and hurricanes (Gutmann et al., 2018) are all projected to be more intense in a future climate in the CONUS, in part due to increased water vapor holding capacity as explained by Clausius Clapeyron theory whereby water vapor increases by 7% per degree of warming. Additionally, precipitation extremes are projected to intensify in a future climate (Ban et al., 2015; Dai et al., 2017; Kendon et al., 2012; Prein et al., 2017a), which suggests that future flood risk will increase as well. While studies by Hirabayashi et al. (2013) and Wing et al. (2018) generally show this expectation to be true, they either underestimate the rainfall driving floods due to using coarse global climate model (GCM) data that does

not properly represent storm dynamics (Hirabayashi et al., 2013), or do not incorporate a climate change effect (Wing et al., 2018). Thus, there has been a dearth of studies that investigate future changes in precipitation specifically associated with a large number of flood-producing storms using high-resolution convection-permitting simulations.

Due to this limited understanding of floods in a future climate, the aim of this dissertation is to analyze how flood-producing storms might change in a future climate over the CONUS. The focus on the storms associated with floods is due to the dramatic future changes expected in storm-related precipitation and the importance of precipitation in forecasting floods. Therefore, this dissertation focuses on the changes in precipitation characteristics and storm-scale aspects (vertical velocity, moisture transport) associated with floods using convective-permitting simulations, rather than a full hydrologic analysis, though it is acknowledged that changes in the full water budget (i.e., soil moisture and evapotranspiration) will play an important role in modulating future flood occurrence. However, runoff is integrated into the examination of flood-producing storms in a future climate in order to gain a more comprehensive understanding of how changes in flood precipitation could affect the hydrologic response. By documenting the precipitation characteristics in hundreds of current flood-producing storms and examining how they could change in a future climate over the CONUS, this dissertation advances the understanding of changes in hydrometeorological extremes in a future, warmer climate. Such research is critical for improving crumbling water infrastructure (Vano et al., 2019), planning for future water resources, and protecting communities over the CONUS against future flood-related risks.

1.2 Dissertation outline

To fully characterize the details of flood-producing storms, published results include a CONUS-wide analysis of flood-producing storms in the current climate (Ch.2–3), changes to these storms in the future (Ch.4), and future changes to specific types of flood-producing storms in certain regions (Ch.5–6). The regional perspective focuses on flood-prone regions in the CONUS and the types of storms that generate such high-impact floods in an attempt to understand the

atmospheric processes that might change and how this could affect the hydrologic impacts. Understanding these regional changes in the context of CONUS-wide changes in future flood-producing storms provides examples of the possible future impacts flood-producing storms could have in a warmer climate.

Chapter 2 (Dougherty & Rasmussen, 2019)¹ provides a climatology of flood-producing storms over the CONUS from 2002–2013 by merging flood reports, streamflow data, and high-resolution precipitation data. This climatology shows that flash flood-producing storms preferentially occur in the warm-season in the Mississippi River Basin, with intense rain rates and short durations; slow-rise flood producing storms tend to occur in the cool-season with hotspots in the Ohio River Valley and Pacific Northwest, and are long-duration low-intensity rainfall events; hybrid flood-producing storms occur in the spring and summer mostly in the central CONUS and Northeast, with moderate rain rates and durations.

Chapter 3 (Dougherty et al. 2020) is unpublished work that is part of a larger project done in conjunction with civil engineers at CSU. This chapter examines the rainfall-streamflow relationship in flood-producing storms between two different river basins in the CONUS to better understand the link between the atmospheric and hydrologic components of floods. Within the larger project, results from this work are incorporated into a study on environmental justice in relation to flood risk over the CONUS.

Chapter 4 (Dougherty and Rasmussen 2020a)² is a novel study investigating changes in nearly 600 flash flood-producing storms in a future climate over the CONUS using convective-permitting simulations. Both precipitation and runoff increase over most of the CONUS in future flood-producing storms, suggesting these storms might become more intense in a warmer climate.

¹The research presented in Chapter 2 have already been presented in *Monthly Weather Review* as Dougherty and Rasmussen (2019).

²The results presented in Chapter 4 are currently accepted into *The Journal of Hydrometeorology* pending major revisions.

Chapter 5 (Dougherty, Sherman, and Rasmussen 2020)³ uses convective-permitting simulations to examine future changes to water budget components (precipitation, snow water equivalent, and runoff) in the cool-season and within 45 flood-producing storms in California. In both the cool-season climatology and individual flood-producing storms, precipitation (snow water equivalent) increases (decreases) leading to more future runoff, which has major implications for California's water resources.

Chapter 6 (Dougherty and Rasmussen 2020b, in prep.)⁴ analyzes future changes in nearly 500 flash flood-producing storms in the Mississippi River Basin using convective-permitting simulations. In addition to examining changes in precipitation and runoff in a future climate, changes in vertical velocity in these mainly convective storms are examined with regard to future changes in precipitation. While precipitation increases in most future storms, those storms with the strongest vertical velocity in the current climate exhibit the largest increase in precipitation in the future.

³The results presented in Chapter 5 are currently accepted into *The Journal of Hydrometeorology* pending major revisions.

⁴The results presented in Chapter 6 plan to be submitted to *The Journal of Hydrometeorology* by summer 2020.

Chapter 2

Climatology of Flood-Producing Storms and Their Associated Rainfall Characteristics in the United States⁵

2.1 Introduction

Floods are a major hazard across the world and are one of the deadliest weather-related natural disasters in the continental United States (CONUS; Ashley & Ashley, 2008a). Well-known floods such as the Rapid City, South Dakota, flood of 1972 and Big Thompson flood of 1976 resulted in 220 and 144 fatalities, respectively (Maddox et al., 1978). The more recent Colorado flood of 2013, which was a result of 450 mm of rain that fell in a week over the Front Range of Colorado, led to 8 fatalities and over \$2 million (U.S. dollars) in damage (Gochis et al., 2015). Flooding from Hurricane Harvey (2017) in the Houston, Texas, area resulted in record rainfall (1548.7mm) from a tropical cyclone in the CONUS and is the second costliest storm in U.S. history (\$125 billion in damage; Blake & Zelinsky, 2018). These examples illustrate that despite occurring in different locations and due to different causes, floods in the CONUS result in tremendous amounts of damage.

Estimates of flood exposure over the past several decades show an increasing trend in urban areas such as Atlanta, Georgia (Ferguson & Ashley, 2017); New York City, New York; and Miami, Florida (Qiang et al., 2017), despite a decreasing trend nationwide (Qiang et al., 2017). Though estimates of current nationwide flood exposure might not agree, studies show that future flood exposure (Wing et al., 2018), and disaster probability (Freeman & Ashley, 2017) will increase over

⁵This chapter has been published by the American Meteorological Society in *Monthly Weather Review*: Dougherty, E. and K. L. Rasmussen, 2019: Climatology of Flood-Producing Storms and Their Associated Rainfall Characteristics in the United States. *Mon. Wea. Rev.*, 147(11), 3861–3877. ©2019 American Meteorological Society. Used with permission.

the CONUS under various growth scenarios. Additionally, given the projected increased intensity of extreme precipitation over the CONUS in a future climate (Allen & Ingram, 2002; Kirtman et al., 2013; Prein et al., 2017c), it is suggested that the U.S. population is becoming increasingly vulnerable to flood-associated risks. Thus, it is critical to better understand the characteristics of floods across the CONUS in order to identify which regions are most vulnerable to floods in a current climate, so that these risks can be better estimated in the future climate.

The cause of floods involves complex hydrologic, geomorphologic, and atmospheric interactions, and is defined by the National Weather Service (NWS) as “the inundation of normally dry area caused by an increased water level in an established watercourse, or ponding of water, that poses a threat to life and property” (NWS, 2007). This definition can include flash floods, slow-rise floods, and coastal floods, amongst others. Though predicting floods is complicated, NWS forecasters rely on key atmospheric variables to indicate where anomalous precipitation is probable to issue flood watches and warnings (A. J. Schroeder et al., 2016a). Similar conditions between high-impact floods, like the Big Thompson (1976) and Rapid City (1972) floods, both of which involved orographic lift of unstable and anomalously moist air up the edge of high terrain (Maddox et al., 1978), suggested that certain atmospheric “ingredients” are necessary to produce floods. However, prior studies primarily relied on pattern recognition of synoptic and mesoscale conditions to understand factors leading to flooding (Funk, 1991; Maddox et al., 1979), rather than a more comprehensive view of numerous ingredients that could cause floods (Doswell et al., 1996). These ingredients were explicitly outlined in the Doswell et al. (1996) “ingredients-based approach” for flash flood forecasting, which emphasized that for floods to occur, multiple ingredients are necessary. Ingredients leading to high rainfall accumulation include high rainfall rates and long duration, as given by the following equation:

$$P = \bar{R}D \quad (2.1)$$

where P is the rainfall accumulation, \bar{R} is the average rainfall rate, and D is the rainfall duration (Doswell et al., 1996). High rain rates are due to factors that enhance precipitation efficiency,

including ample moisture and a lifting mechanism, while long-duration rainfall can be caused by quasi-stationary convective and/or synoptic systems (Doswell et al., 1996). These ingredients, particularly anomalously high precipitable water, were present in the Big Thompson and Rapid City floods (Caracena et al., 1979; Maddox et al., 1978), as well as a majority of urban flash floods over the CONUS (A. Schroeder et al., 2016b).

Case studies of floods around the world have additionally exemplified the importance of how the Doswell et al. (1996) ingredients manifest in different ways. A flash flood in Leh, India, in August 2010 was the result of upslope flow of moist, conditionally unstable air along a steep edge of the Himalayas and anomalous quasi-stationary synoptic conditions over the Tibetan plateau with an associated easterly low-level jet that combined to form a series of mesoscale convective systems (MCSs) propagating over the Himalayas (K. L. Rasmussen & Houze Jr, 2012). In Pakistan, long-lived flooding from July to August 2010 was due to a quasi-stationary synoptic pattern and channeling of anomalous moisture into the region toward the Himalayan barrier that caused prolonged stratiform precipitation (R. Houze Jr et al., 2011). The Colorado flood of 2013 and Uttarakhand, India, floods in June 2013 similarly involved upslope flow of moist air over a prolonged period of time (several days to weeks), but these floods were characterized by stratiform rainfall with embedded weak to moderate convection, unlike the previous U.S. flash flood cases (Gochis et al., 2015; R. Houze Jr et al., 2017). Therefore, similar “ingredients” defined by Doswell et al. (1996) are responsible for a variety of flood types around the world.

From a climatological perspective, heavy rainfall has been utilized as a proxy for flooding in the CONUS, as suggested by Doswell et al. (1996). Maddox et al. (1979) utilized National Oceanic and Atmospheric Administration (NOAA) storm data to examine atmospheric regimes associated with flash floods, highlighting the importance of fronts, synoptic systems, and thunderstorm outflow boundaries for triggering intense rainfall. Brooks and Stensrud (2000), Schumacher and Johnson (2006), Kunkel et al. (2012), and Stevenson and Schumacher (2014) developed climatologies of heavy rain events over the CONUS using data from rain gauges and Stage IV precipitation data. These studies found that heavy rainfall peaked in the summer (Brooks & Stensrud, 2000;

Maddox et al., 1979; Schumacher & Johnson, 2006; Stevenson & Schumacher, 2014), and were due to mesoscale convective systems (MCSs) in the central United States (Kunkel et al., 2012; Schumacher & Johnson, 2006), the monsoon in the Southwest (Kunkel et al., 2012), extratropical cyclones in the Pacific Northwest (Kunkel et al., 2012), and tropical cyclones in the eastern United States (Kunkel et al., 2012; Schumacher & Johnson, 2006). Though these heavy rainfall climatologies provide a sense of probable flood occurrence over the CONUS, precipitation is not the only contributor to floods, with soil moisture storage capacity also being an important factor (Berghuijs et al., 2016), in addition to underlying geomorphology and hydrologic processes.

Given the complexity and risk of flooding in the CONUS (Ashley & Ashley, 2008a), various CONUS-wide flood databases and climatologies have been developed that include numerous parameters, in addition to precipitation. Examination of factors in conjunction with precipitation is necessary to gain a comprehensive understanding of floods, since floods are caused by rain interacting with varying terrain gradients, soil types, vegetation, land use, and antecedent soil moisture conditions (Davis, 2001). Gourley et al. (2013) created the Flooded Locations and Simulated Hydrographs (FLASH) database that combines U.S. Geological Survey (USGS) streamflow observations, NWS storm reports, and two-years' worth of survey responses that documents flash floods. Shen et al. (2017) also created a comprehensive database of over 0.5 million floods over the CONUS from 2002 to 2013 using USGS streamflow measurements to identify floods and Stage IV rainfall to provide contributing rainfall information. A number of studies have utilized these databases, especially the FLASH database. Saharia et al. (2017a) used the FLASH database (Gourley et al., 2013) to identify flash flood hotspots based on discharge peaks in the CONUS and to characterize floods more broadly in the CONUS based on season, climatic region, and basin geomorphology (Saharia et al., 2017b). Michaud et al. (2001) and B. K. Smith and Smith (2015) also used discharge to identify flash floods in the CONUS, based on discharge peaks in small-basins (10–200 km²) and unit discharge exceeding 1 m³ s⁻¹ km⁻², respectively. Ashley and Ashley (2008b) used the National Centers for Environment Information (NCEI; formerly National Climatic Data Center) Storm Report data to identify deadly floods in the CONUS from 1996 to 2005

and their associated synoptic and mesoscale environments. Despite different flood identification metrics, these studies (and others) identify similar regional flood patterns over the CONUS: floods in the East have high discharge and precipitation, mainly associated with warm-season convective rainfall (Michaud et al., 2001; Saharia et al., 2017a; B. K. Smith & Smith, 2015) or hurricanes (Ashley & Ashley, 2008b); Western floods occur in steeper sloped basins in the winter for the West Coast (B. K. Smith & Smith, 2015; Villarini, 2016) due to extratropical cyclones (Ashley & Ashley, 2008b; Saharia et al., 2017a) and summertime in the Southwest (Michaud et al., 2001; Villarini, 2016) due to the monsoon (Ashley & Ashley, 2008b; Saharia et al., 2017b).

While previous flood and heavy rainfall climatologies over the CONUS document various aspects of flooding (streamflow, extreme rain rates, fatalities), an important perspective related to the meteorological characteristics associated with specific floods is missing in the literature. Thus, the primary goal of the current study is to produce a climatology of rainfall characteristics in flood-producing storms in the CONUS. While flood databases like Shen et al. (2017) provide a thorough documentation of floods in the CONUS, the focus is more on hydrologic processes, as one flood event in their database could have multiple peaks in streamflow over a period spanning months (Mei & Anagnostou, 2015), likely involving numerous meteorological systems. Other databases, like the comprehensive FLASH database (Gourley et al., 2013), only consider flash floods, and this study seeks to examine different flood types. The heavy rainfall climatologies are helpful from a forecasting-perspective, but do not translate directly to floods due to factors in addition to rainfall, such as terrain gradients, soil moisture, storm characteristics, and land use, needed for a flood to occur. Thus, this study fills a gap by examining the rainfall characteristics associated with flood-producing storms using the NCEI Storm Events Database, which identifies where flooding (as defined by the NWS) actually occurred and groups these floods by the associated meteorological system. The NCEI database integrated with the Shen et al. (2017) gauge-identified floods and Stage IV precipitation data provides a method of identifying floods from flood reports and stream gauges, and analyzing their associated rainfall characteristics over the CONUS from 2002 to 2013. Though the focus of this study is on the rainfall characteristics of floods, it is acknowledged that

hydrologic, topographic, and land-use factors are vital for producing floods, and were inherent in generating the floods used in this database. Examination of these non-atmospheric factors is beyond the scope of the study, although their effects may be implicitly included in the methodology by matching precipitation associated with flood reports with peaks in streamflow consistent with river flooding. Note that throughout the manuscript, “floods” and “flood-producing storms” is used interchangeably.

The understanding gained from this climatology of the duration, rainfall accumulation, seasonality, and spatial occurrence associated with flood-producing storms is vital to increase awareness of rainfall-associated flood risks specific to individual regions. Additionally, this study provides a necessary first step in understanding the overall climatology of flood-producing storms over the CONUS to enable future research investigating how flood-producing storms may change in a future climate using high-resolution, convection-permitting simulations from Liu et al. (2017). Results from this climatology in conjunction with future research on flood-producing storms in a future climate will provide insights on current and future flood risk.

2.2 Data and methods

2.2.1 *NCEI Storm Events Database*

The NCEI Storm Events Database is a documentation of notable meteorological events from January 1950– September 2017, available from the NCEI website.⁶ NCEI receives details on the location, date, and time of these events primarily from NWS, as well as other outside sources, including media and law-enforcement. The events in the database include blizzards, hurricanes, hail, and floods, among a long list of others, and this study utilizes flood reports from 2002 to 2013. NCEI makes a distinction between flash floods and floods in the database. According to guidelines provided by NWS (NWS, 2007), flash floods are defined by “a rapid and extreme flow of high water into a normally dry area, or rapid water level rise in a stream or creek above a predetermined flood level, beginning within six hours of the causative event (e.g., intense rainfall, dam failure,

⁶<https://www.ncdc.noaa.gov/stormevents/>

ice jam–related),” while floods are defined by “the inundation of a normally dry area caused by an increased water level in an established watercourse, or ponding of water, generally occurring more than six hours after the causative event, and posing a threat to life or property.” For this reason, floods will be called slow-rise floods from this point forward, due to their longer temporal nature.

Note that the above NWS flood definitions are used primarily as a forecasting tool, thus, the flood classification in this study is not confined to the specific definition (or duration) given that a single flood episode can be composed of numerous storm reports (or events) and can be a mix of flash and slow-rise floods. This fact necessitated the creation of a separate category of floods–hybrid floods–when reports (or events) within the same episode were labeled as both flash and slow-rise floods. Though a single hybrid flood episode might be more or less flash or slow-rise in nature, having characteristics of both at any point makes these floods uniquely different in character and merits its own category, due to unique storm characteristics. An example of such a hybrid flood is the Colorado flood of 2013 (Gochis et al., 2015), which was a high-impact flood along the Front Range of Colorado that was both long-duration (nearly a week long), with “flashier” bouts of intense convection within stratiform rainfall, thus reported as both a flash and slow-rise flood.

Due to the somewhat subjective nature of these flood reports, there are limitations in using the NCEI Storm Events Database. Inaccuracies of these reports are acknowledged by NCEI, particularly when derived from sources beyond NWS. Other sources of error in this database include population biases and differences in reporting by NWS Weather Forecast Offices (WFOs). When examining the same dataset, Ashley and Ashley (2008a) found that eastern CONUS displayed more flood fatalities than the western CONUS, which they partially attributed to higher population in the East. It is an often-cited limitation of the Storm Events Database that report biases occur due to differences in population density by region, urban versus rural areas, and at night (Barthold et al., 2015; Herman & Schumacher, 2018b). Additionally, the issuance of warnings and report encoding is known to differ by NWS WFOs, with some WFOs preferring to encode an event as flash flood rather than a flood (Herman & Schumacher, 2018b; Nielsen et al., 2015).

Table 2.1: The number of flash, slow-rise, and hybrid flood-producing storms for events (episodes) in the NCEI Storm Event Database in the left (right) column that match flooded stream gauge locations from the Shen et al. (2017) database. The row labeled “all” is the sum of flood episodes for all flood types.

	Events	Episodes
Flash floods	15 932	2808
Slow-rise floods	10 614	1638
Hybrid floods	11 120	1113
All	37 666	5559

Despite the limitations of the Storm Events Database, this database is advantageous for the purposes of our study—to understand rainfall characteristics in flood-producing storms. First, the NCEI Storm Events Database contains a large sample of floods over the CONUS, with over 35 000 flood reports from 2002 to 2013 (Table 2.1). Second, Herman and Schumacher (2018b), who studied flash flood verification over the CONUS, state that these flood reports, while underreported, likely have few false alarms. This provides confidence that the large sample of flood reports in the NCEI database capture actual flood occurrence, as opposed to peaks in streamflow or rainfall, which may or may not result in a flood. Finally, the database provides a meteorological-centric viewpoint of floods through the grouping of numerous flood reports (or “events”) in a given location with a single flood episode, based on being associated with the same meteorological system (as defined by NWS; see NWS, 2007). This is critical to the goal of the present study in taking a storm-centric viewpoint of the rainfall associated with floods (similar to Ashley & Ashley, 2008b, though they examined flood fatalities), and is major reason for using this database over others. The flash, slow-rise, and hybrid floods from the NCEI database were examined over their entire storm life cycle, and were matched to the Shen et al. (2017) database to associate flood reports to streamflow-identified floods.

2.2.2 Merging storm reports with the Shen et al. (2017) database

Shen et al. (2017) developed a comprehensive flood database over the CONUS from 2002 to 2013 using a characteristic point method (CPM) described by Mei and Anagnostou (2015). The

CPM is an automated method used to identify flood events by the rising and recessing branches of a hydrograph using instantaneous USGS streamflow values. Only peak streamflow values between the rising and recessing branches of the hydrograph that exceed the 80th percentile are utilized. Shen et al. (2017) additionally used basin-averaged Stage IV precipitation to associate the peak in streamflow with flood-triggering precipitation.

While the Shen et al. (2017) flood database is thorough and comprehensive, it does not meet the goals of the present study to focus on the rainfall input to floods from a storm-perspective. This was evident when examining the Shen et al. (2017) database (<http://ucwater.engr.uconn.edu/fedb>) that contained a nearly 2-yr-long flood from August 2007 to June 2009 in Wisconsin, with precipitation averaged over a 2-yr period. Clearly, no single storm or rain-producing system lasts for two years, with typical life spans of rain-producing systems on the order of hours (thunderstorms), days (mesoscale convective systems), to weeks (hurricanes and extratropical cyclones). Thus, while the Shen et al. (2017) database is useful in identifying peaks in streamflow, including multiple closely spaced peaks (Mei & Anagnostou, 2015) that explain the 2-yr long flood in their database, it does not fit the precise needs of the present study.

However, to provide confidence that the NCEI Storm Reports used to identify floods in this study had a streamflow response, NCEI Storm Reports beyond three days and 200 km of gauge-identified floods by Shen et al. (2017) were excluded. A three-day period was chosen to account for a lag between start times in the Shen et al. (2017) database (based on the rising branch of the hydrograph) and the NCEI database (when the flood was reported, i.e., due to a rise in streamflow above a predetermined flood level or flow of water onto normally dry land; NWS, 2007). A buffer of 200 km was selected based on average distances across various river basins, including the South Platte (Colorado), Wabash (Indiana), and Willamette (Oregon) basins, providing confidence that the flood indicated by the Shen et al. (2017) database and the storm reports were in the same river basin, and thus, most likely associated with the same event. Matching the NCEI Storm Reports with floods from Shen et al. (2017) resulted in 15 932 (2808) flash flood events (episodes), 10614 (1638) slow-rise flood events (episodes), and 11 120 (1113) hybrid flood events (episodes;

Table 2.1). Among the hybrid floods, 6786 (61%) of events were labeled as flash floods and 4334 (39%) were labeled as slow-rise floods, giving a slight bias toward flash floods in this category.

2.2.3 Stage IV precipitation data

The lack of rainfall information in the storm report data was mitigated by the use of Stage IV precipitation data (Nelson et al., 2016). This data is available at a 4-km hourly resolution since 2001, and is a multisensor (radar-estimated rainfall combined with rain gauge data) precipitation analysis (MPE) produced by twelve River Forecast Centers (RFCs) over the CONUS. Regional MPEs are quality controlled by RFCs and merged into a national product by the National Centers for Environmental Prediction (NCEP; Lin & Mitchell, 2005). Though errors exist in Stage IV data—discontinuities across RFC boundaries, sparser coverage over the western CONUS due to less radar coverage and rain gauges, and quality control issues at the hourly time scale—Stage IV data is considered the benchmark precipitation estimate over the CONUS used to validate other precipitation data and high-resolution simulations (Beck et al., 2019; Nelson et al., 2016; Prein et al., 2017c; K. L. Rasmussen et al., 2017). This high-resolution, MPE dataset is necessary for studying rainfall associated with floods, as flood-producing rainfall can be transient and small-scale, especially in flash floods (Davis, 2001). Despite these deficiencies, spatial patterns of flash flood rainfall characteristics in Stage IV hourly data compare quite well to TRMM 3B42 rainfall, providing confidence that physical rainfall characteristics are captured, and not just artifacts of these errors.

To gather Stage IV data associated with floods identified from the Storm Events Database (section 2a), the location and duration of the reported flood episode was utilized. The centroid of each flood episode was calculated based on geographic information obtained from merging the storm reports with county shapefiles.⁷ Hourly (every third hourly) Stage IV rainfall data were obtained over a radius of $\pm 5^\circ$ from the episode centroid for flash and hybrid (slow-rise) floods, in order to capture the entire storm system's contribution to the reported flood. A sensitivity test was

⁷https://www.census.gov/geo/maps-data/data/cbf/cbf_counties.html

conducted for varying radii, and at smaller radii, the flood-contributing rainfall was cut off, hence the use of the $\pm 5^\circ$ radius. It is possible that even at this large of a domain, some rainfall could be missed, due to flood waves propagating downstream from the causative event. Every third hourly Stage IV rainfall file for slow-rise floods was utilized rather than every hourly file due to the long-duration of these floods that resulted in an unmanageable amount of data at the hourly scale. Note that when hourly Stage IV files were not available (i.e., for the Pacific Northwest RFC; Nelson et al., 2016.), six hourly files were used instead, which constituted 60 slow-rise flood episodes. These Stage IV files were analyzed for the duration of each episode, which was provided in the storm report data-base, plus a buffer ± 1 (6) hours for flash (slow-rise and hybrid) floods to take into account possible rainfall occurrence before and/or after the start of the reported flood event. The temporal buffers were chosen based on the observation that flash floods are generally more transient, due to their convective nature (Davis, 2001).

Given the large domains over which rainfall data was analyzed, the flood-contributing rainfall likely associated with each flood was isolated through an object-identifier tool in Python. This tool identified the largest contiguous precipitation area where the flood domain precipitation accumulation met or exceeded the 75th percentile. This method locates and isolates the maximum precipitation accumulation and the surrounding high accumulation for all floods, irrespective of the size of the precipitation swath—this allows for isolated convective rainfall to be captured, as well as larger-scale synoptic rainfall from MCSs, fronts, or extratropical cyclones. Such an example of this method isolating the heavy flash flood rainfall from lighter nonflash flood rainfall is shown in Figure 2.1, and similarly isolates the maximum rainfall in slow-rise (not-shown), and hybrid floods (not shown).

Various rainfall metrics were calculated for each flood episode, including accumulated rainfall, area, and duration of the largest contiguous rainfall area exceeding the 75th percentile of accumulation. These quantities were then averaged over the 12-yr period for 1) each Stage IV 4-km grid cell and 2) all episodes by flood type. The number of floods per grid cell was also summed over

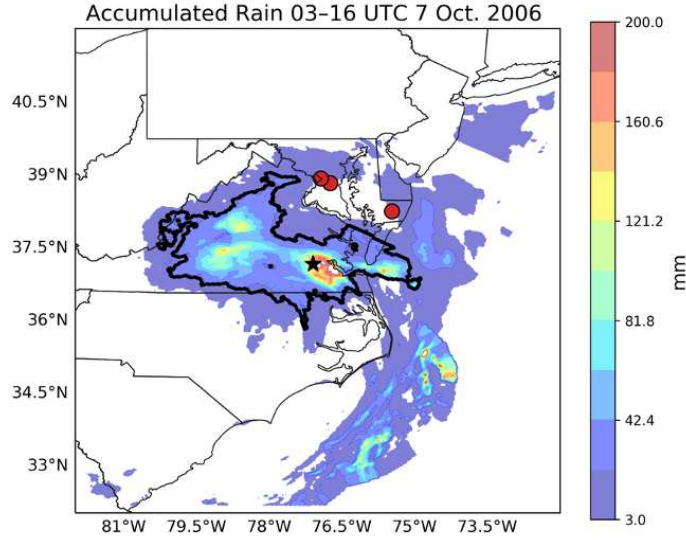


Figure 2.1: An example of the methodology used to identify flood-producing storm rainfall from Stage IV rainfall data. A flash flood in Virginia occurred from 0300 to 1600 UTC 7 Oct 2006, with its flood centroid shown by the star, flooded stream gauges from the Shen et al. (2017) database in red dots, and largest contiguous area of Stage IV accumulated precipitation (shaded; mm) over the 75th percentile outlined in black, as identified from an object-identifier tool in Python.

the entire 12-yr period to find the episode frequency. This calculation allowed for variables to be multiplied by a scaling factor similar to K. L. Rasmussen et al. (2016):

$$F = \frac{N_f}{N_t} \quad (2.2)$$

where F is the scaling factor, N_f is the number of flood episodes per Stage IV grid cell, and N_t is the total number of flood episodes over the CONUS. These normalized variables allowed for a spatial comparison of flood characteristics over the CONUS, despite different episode frequencies.

2.3 Results

2.3.1 Seasonal and geographical distribution of floods

The number of flood episodes per month is shown in Figure 2.2 which has similarly been shown in previous studies, though only for flash floods (Brooks & Stensrud, 2000; Maddox et al., 1979; Schumacher & Johnson, 2006). Flash floods display a warm-season maximum from

May to August. An absolute maximum occurs in July, which is consistent with findings of heavy rainfall seasonality from Maddox et al. (1979), Brooks and Stensrud (2000), Schumacher and Johnson (2006), and Stevenson and Schumacher (2014). A spring to early summer maximum (March–June) is seen for slow-rise floods, which is associated with rain-on-snow events that occur in the spring as precipitation falls as rain on melting snow (Ashley & Ashley, 2008b; McCabe et al., 2007). Hybrid floods display a maximum in May–July due to synoptic rainfall and MCSs (Ashley & Ashley, 2008b; Kunkel et al., 2012; Schumacher & Johnson, 2006). The consistency of the seasonal distribution of floods with the literature, particularly the agreement between flash flood seasonality with previous climatologies, provides confidence in the flood-producing storm climatology developed herein.

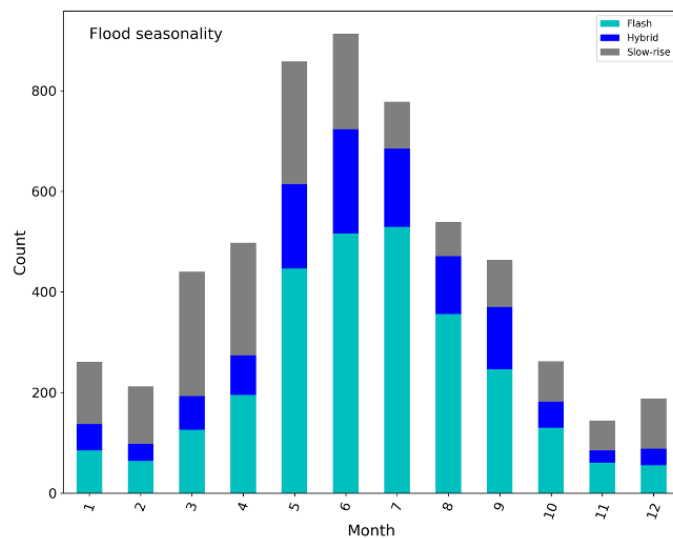


Figure 2.2: Number of flood episodes per month summed from 2002 to 2013, where cyan represents flash floods, dark blue represents hybrid, and gray represents slow-rise floods.

The reason for the varying seasonality of different flood types is generally linked to different underlying causes. Post-2006, the NCEI Storm Events database attributed causes to flood reports, as shown in Table 2.2. Note that the percentages are the percent of flood causes post-2006 excluding missing data (thus adding up to ~100% for each flood type). The leading cause for all floods is heavy rain, comprising 94.8% of flash floods, 74.5% of slow-rise floods, and 89.0% of hybrid

floods. This result is not surprising, given that heavy rainfall is a necessary ingredient for flooding (Doswell et al., 1996), though the nature of heavy rainfall likely differs between flood types. The second largest contributing cause to each flood type is heavy rain over a burn area for flash floods (2.2%), heavy rain-on-snowmelt for slow-rise floods (20.7%), and heavy rain from a tropical system for hybrid floods (3.9%). The heavy rain on snowmelt supports the springtime maximum for slow-rise floods (Figure 2.2), while the heavy rain from a tropical system explains some of the summertime maximum in hybrid floods.

Table 2.2: Percentage of flood causes comprising each type of flood, where boldface values indicate the largest percentage and italic values indicate the second largest percentage. Flood causes only include post-2006 NCEI Storm Events data and exclude missing data from the calculation.

Flood type	Dam/ levee break	Heay rain	Heavy rain/ burn area	Heavy rain/ snowmelt	Heavy rain/ tropical system	Ice jam	Planned dam release
Flash	0.7	94.8	2.2	0.5	1.7	0.1	0.1
Slow-rise	0.4	74.5	0.3	<i>20.7</i>	2.4	2.4	0.3
Hybrid	3.2	89.0	0.3	2.5	3.9	0.4	0.7

To extend the seasonal analysis of floods beyond Figure 2.2, the spatial distribution of each flood type is examined by season (Figure 2.3–Figure 2.5). Events per state from the NCEI Storm Events Database are summed over the 12-yr period and normalized by state area, to account for differing state sizes. Flash floods in the winter (Figure 2.3a) are confined mostly to the Gulf Coast, Southeast, Ohio River valley, and California. This distribution is due to increased north and northeast moisture transport from the Gulf of Mexico in the Southeast and Ohio River valley (Trenberth, 1999), while the California maxima is attributed to atmospheric rivers (ARs) that affect the West Coast during the winter (M. D. Dettinger et al., 2011a; Saharia et al., 2017a; Young et al., 2017). Transitioning to spring (Figure 2.3b), flash flood occurrence spreads northward and eastward, covering much of the eastern United States, as warm-season convection begins and synoptic systems frequent this area (Maddox et al., 1979). By summer (Figure 2.3c), flash floods are nearly ubiquitous over the entire CONUS, highlighting the predominant role of warm-season

convection in causing flash floods, as shown in Figure 2.2 and other studies (Davis, 2001; Maddox et al., 1979; Schumacher & Johnson, 2006). This result is expected, as most of the country is generally warm enough to support convection in the summer. The maximum in flash floods in the Midwest and plains is due to MCSs, which contribute 30%–70% of warm season rainfall to these regions (J. Fritsch et al., 1986) and are frequently associated with flooding (Ashley & Ashley, 2008b; Kunkel et al., 2012; Michaud et al., 2001; Schumacher & Johnson, 2006). During the summer, the North American monsoon is also at its peak (Adams & Comrie, 1997), which explains the flash flood maximum in the Southwest seen in Figure 2.3c and observed in other studies (Ashley & Ashley, 2008b; Kunkel et al., 2012; Saharia et al., 2017b). By fall (Figure 2.3d), flash floods transition to the South (similar to the winter), clustered in the Southeast, Gulf Coast, East, and Ohio River valley. Remnants of the North American monsoon signal is seen by the maximum in the Southwest. These seasonality results are broadly consistent with heavy rainfall analyses over the CONUS (Brooks & Stensrud, 2000; Kunkel et al., 2012; Maddox et al., 1979; Schumacher & Johnson, 2006), and flood climatologies (Ashley & Ashley, 2008b; Michaud et al., 2001; Saharia et al., 2017b, 2017a; B. K. Smith & Smith, 2015), with minor discrepancies attributed to different data utilized in the present study.

Slow-rise floods exhibit a noticeably different seasonality than flash floods (Figure 2.4), likely owing to different underlying causes (Table 2.2). During the winter (Figure 2.4a), slow-rise floods are clustered in the Northeast and Ohio River valley, where heavy rainfall from fronts and extratropical cyclones frequently occur (Kunkel et al., 2012; Schumacher & Johnson, 2006). A secondary wintertime maximum is observed on the West Coast, which is affected by flooding from ARs and extratropical cyclones (M. D. Dettinger et al., 2011a; Kunkel et al., 2012; Saharia et al., 2017b; Young et al., 2017), as well rain-on-snow events (Ashley & Ashley, 2008b; McCabe et al., 2007). The West Coast AR signal fades slightly by springtime (Figure 2.4b), while the north-central and upper Midwest display maxima, due to the occurrence of rain-on-snow events during the spring (Ashley & Ashley, 2008b; Berghuijs et al., 2016; McCabe et al., 2007; Michaud et al., 2001; Villarini, 2016), consistent with Table 2.2 and Figure 2.2. The Northeast maximum remains

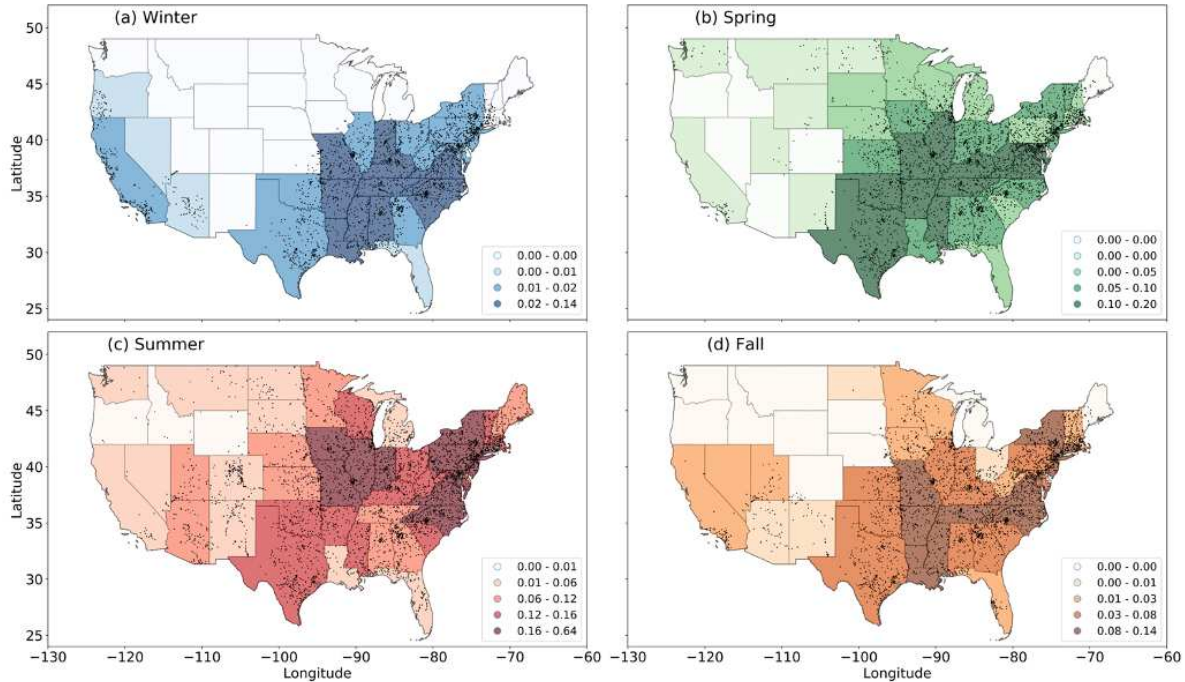


Figure 2.3: Number of flash flood events per state (fill; normalized by state area) and locations of USGS gauge-indicated floods from the Shen et al. (2017) database (black dots) over the CONUS from 2002 to 2013 for (a) winter (DJF), (b) spring (MAM), (c) summer (JJA), and (d) fall (SON).

in the spring, as synoptic systems still frequent this area (Kunkel et al., 2012). By the summer (Figure 2.4c), the distribution of slow-rise flood events is less straightforward. A maximum along the eastern U.S. coastline is due to tropical systems (Ashley & Ashley, 2008b; Kunkel et al., 2012; Schumacher & Johnson, 2006; Villarini et al., 2014), while maxima in the upper Midwest and Ohio River valley are the result of synoptic systems or long-lived MCSs (Ashley & Ashley, 2008b; Kunkel et al., 2012; Schumacher & Johnson, 2006). The less apparent slow-rise flooding in the Intermountain West is explained by rain-on-snow events in the Rocky Mountains, which occur later in the season due to a longer snowfall season than other areas (McCabe et al., 2007), and upslope convection (Ashley & Ashley, 2008b). During the fall (Figure 2.4d), the distribution of slow-rise floods is similar to winter, as ARs begin affecting the West Coast, and frontal systems, as well as tropical cyclones frequent the eastern United States (Ashley & Ashley, 2008b; Kunkel et al., 2012; Schumacher & Johnson, 2006).

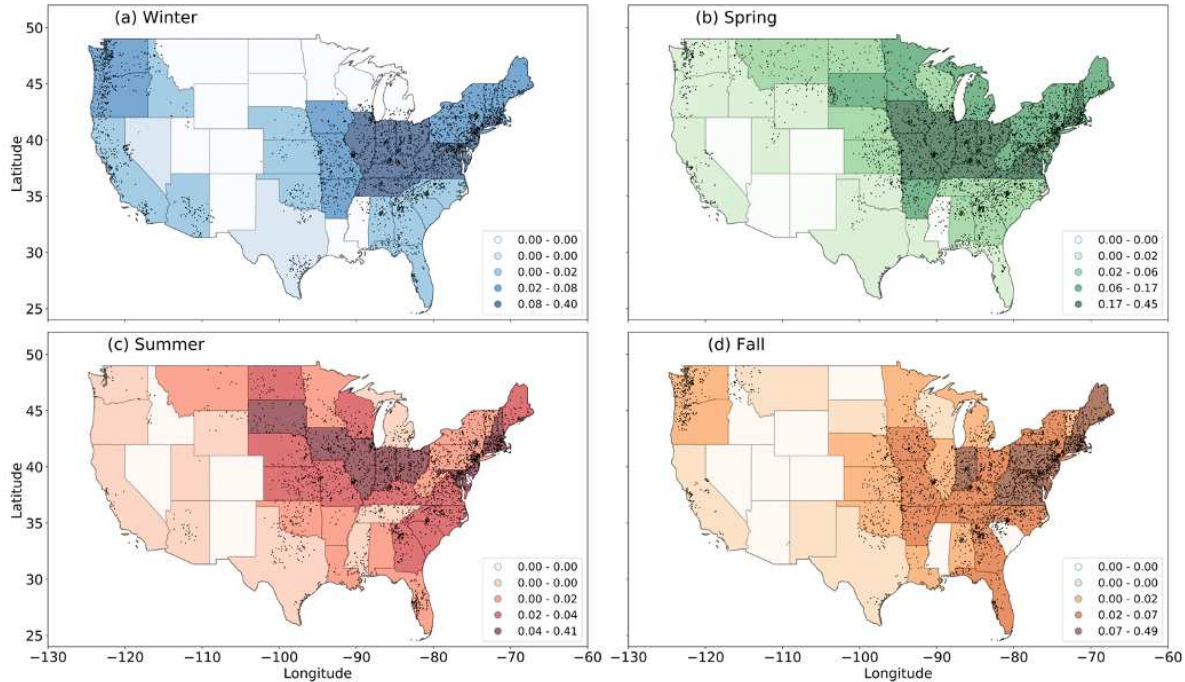


Figure 2.4: As in Figure 2.3, but for slow-rise floods.

Hybrid flood seasonality (Figure 2.5) is less intuitive than slow-rise or flash floods, given that it has characteristics of both. Despite the lack of clarity of results, hybrid floods are nonetheless important to consider, as some high-impact floods, such as the Colorado flood of 2013 (Gochis et al., 2015), fall into this category. During the winter (Figure 2.5a), hybrid floods occur from the Southeast to Ohio River valley and Northeast, as well as the Southwest. This pattern appears to be more similar to the flash flood wintertime distribution (Figure 2.3a; also consistent with Table 2.2) and is attributed to the same causes. The springtime pattern of hybrid floods (Figure 2.5b) appears to be a blend between the flash and slow-rise distribution (Figure 2.3b and Figure 2.4b), thus displaying influences of rain-on-snow floods in northern and mountainous regions, as well as the start of warm-season convection in the Midwest. Springtime West Coast maxima are attributed to late-season ARs (M. D. Dettinger et al., 2011a; Young et al., 2017). Summertime hybrid floods also show similarities to flash and slow-rise floods, with some East Coast locations displaying maxima, as well as the upper Midwest, and plains. This suggests that synoptic events, MCSs, and TCs that have “flashier” elements than slow-rise floods account for this spatial distribution. By

fall (Figure 2.5d), hybrid floods occur most notably in the mid-Atlantic and Ohio River valley, highlighting the predominance of tropical cyclones [viz., Hurricanes Irene (2011), Hanna (2008), Gustav and Ike (2008); NHC] and frontal influences (Ashley & Ashley, 2008b; Kunkel et al., 2012; Villarini et al., 2014).

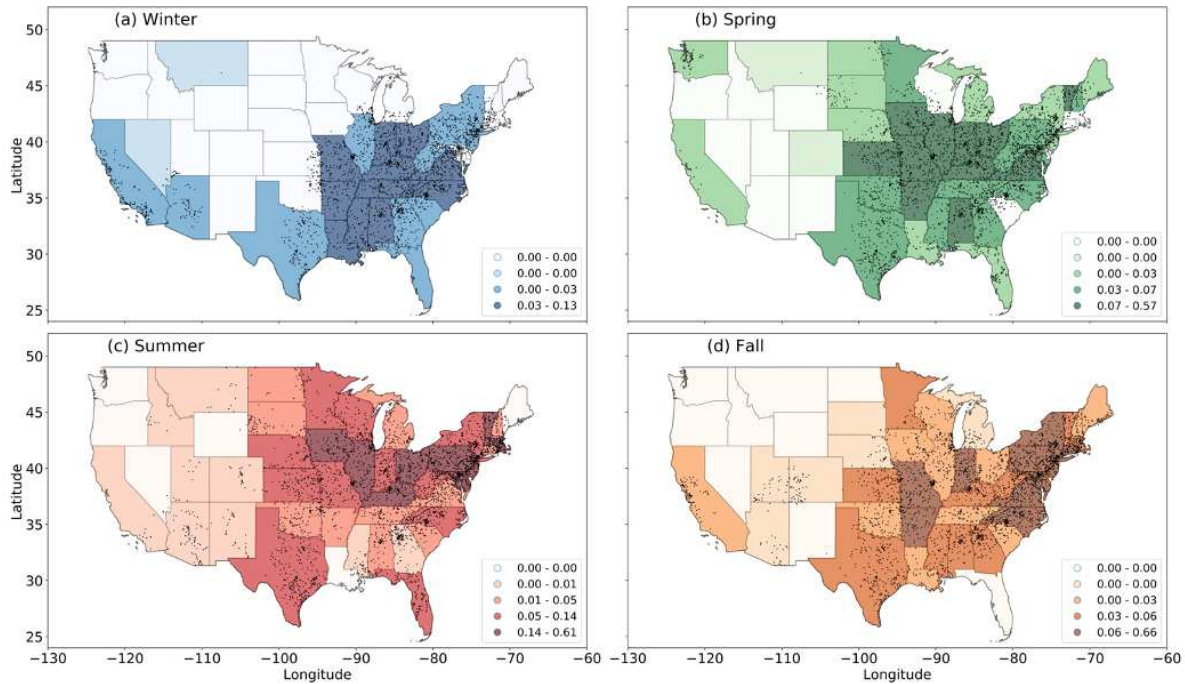


Figure 2.5: As in Figure 2.3, but for hybrid floods.

The total flood events per state from Figure 2.3–Figure 2.5 are shown in Figure 2.6. Flash floods (Figure 2.6a) occur mostly to the east of the Rockies, with a secondary maximum in the Southwest. This result is reflective of the warm season convective and Southwest monsoon signals from Figure 2.3. Slow-rise floods (Figure 2.6b) show more of a northern maximum compared to flash floods, with most events clustered in the Northeast, Ohio River valley, upper Midwest, and Pacific Northwest. The northern maximum appears to be a result of the winter and springtime rain-on-snow events, while the Pacific Northwest maximum is attributed to ARs (Figure 2.4). The distribution of hybrid floods (Figure 2.6c) is less straightforward, predominantly occurring in the mid-Atlantic, Ohio River valley, and plains. This suggests that hybrid floods experience the same

flood-producing storms as both flash and slow-rise floods, but are distinguished by longer durations than flash floods and more convective characteristics than slow-rise floods, as will be shown in the following section.

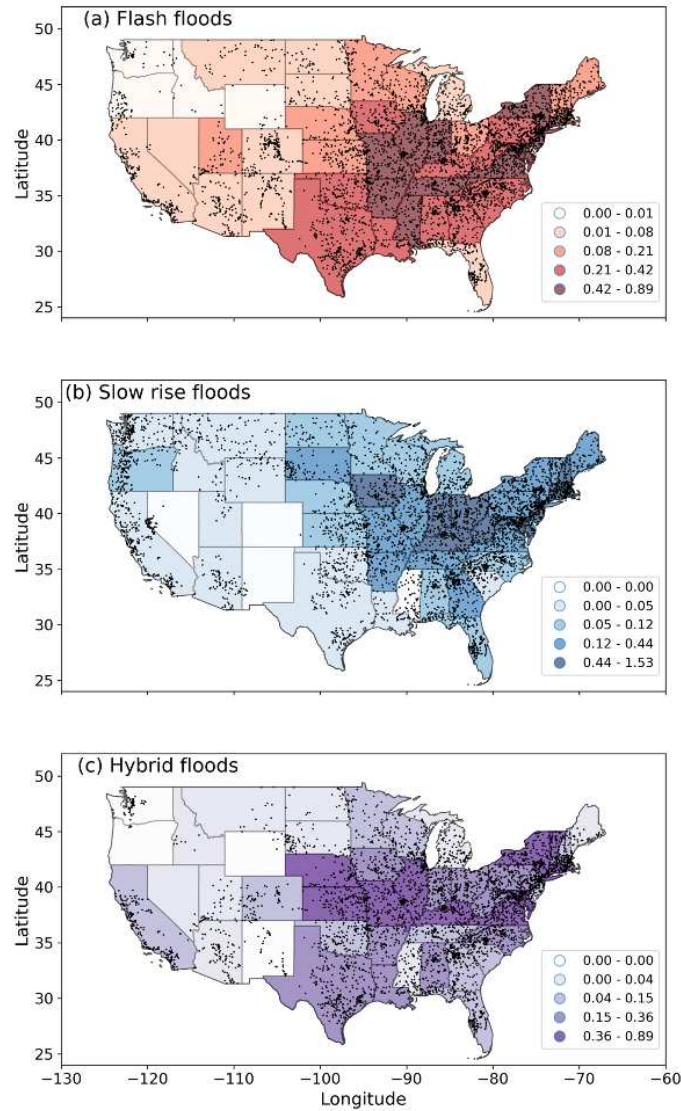


Figure 2.6: Number of (a) flash, (b) slow-rise, and (c) hybrid flood events per state (fill; normalized by state area) and locations of USGS gauge-indicated floods from the Shen et al. (2017) database (black dots) over the CONUS from 2002 to 2013.

2.3.2 Rainfall characteristics of flood-producing storms

In addition to examining when and where floods occurred, it is important to consider the distribution of rainfall characteristics over the CONUS using Stage IV rainfall data, especially since rainfall characteristics are lacking in the NCEI Storm Events Database. The episode frequency, average rainfall accumulation, area, and duration per Stage IV grid cell ($\sim 4 \text{ km} \times 4 \text{ km}$) for 12 years over the CONUS for each flood type is shown in Figure 2.7, Figure 2.8, and Figure 2.10. The qualitative distribution rather than the quantitative value is more important to focus on for these results to compare regions with differing flood rainfall characteristics.

Flash flood rainfall characteristics (Figure 2.7) show that flash floods frequently occur in the Mississippi and Ohio River Valleys (Figure 2.7a), where there is also the highest average rainfall accumulation (Figure 2.7b), largest average area (Figure 2.7c), and moderate durations (15–24h; Figure 2.7d). Given the proximity to major rivers such as the Mississippi and Ohio Rivers, along with persistent moisture source from the Gulf of Mexico, and frequent year-round convection (Schumacher & Johnson, 2006; Figure 2.3), this result is consistent with expectations and with previous work (Michaud et al., 2001; Saharia et al., 2017a). Missouri and Arkansas stand out as notable hotspots for flash flood frequency and rainfall accumulation, which is unsurprising, due to the number of devastating floods in this location associated with MCSs (Ashley & Ashley, 2008b; Schumacher & Johnson, 2008, 2009). Notice that a secondary maximum in flash flood rainfall characteristics occurs in the Southwest, where, despite flash floods being only moderately frequent (Figure 2.7a) with low average rainfall accumulation (Figure 2.7b) and a small average area (Figure 2.7c), they are associated with long-lived storms (over 24 h; Figure 2.7d). These long-lived storms occur in January and from July–October, during the monsoon (not shown), and could be due to terrain-enhanced and terrain-locked precipitation (Neiman et al., 2004), as well as repeated convective initiation over the terrain. Maddox et al. (1979) and Michaud et al. (2001) similarly found that western flash flood events were less frequent and had lower rainfall amounts, but were shorter in duration, which is inconsistent with our results. Our results include all flash floods in the Southwest, whereas Maddox et al. (1979) only considered 31 floods in the western

CONUS that fit pattern recognition of synoptic conditions causing floods, while Michaud et al. (2001) only considered small basin ($< 200 \text{ km}^2$ in area) floods. Both Maddox et al. (1979) and Michaud et al. (2001) are thus more limited in scope, while results from this study characterize the full spectrum of flash floods, which likely explains the discrepancy of long-duration events in the Southwest with previous studies (Maddox et al., 1979; Michaud et al., 2001).

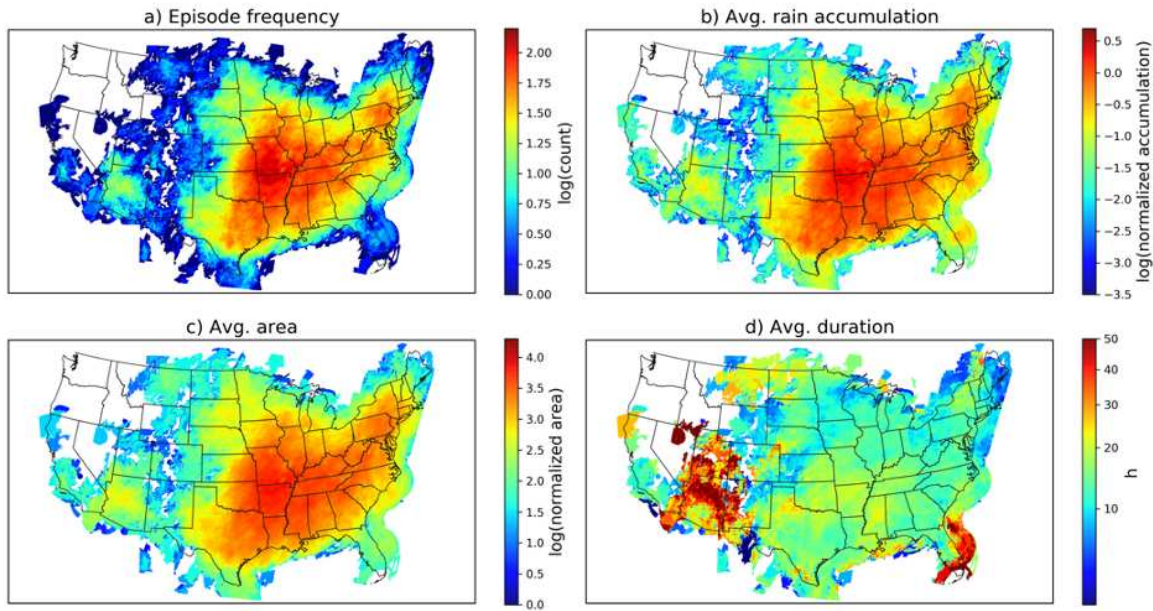


Figure 2.7: Flash flood (a) episode count, (b) average rain accumulation, (c) average area, and (d) average duration (h) per Stage IV grid cell from 2002 to 2013. Values in (a)–(c) are on logarithmic scales, while those in (b) and (c) have been normalized by a scaling factor (number of flood events in Stage IV grid cell/total number of flood events).

Similar to the distribution of storm reports (Figure 2.4), maximum values in slow-rise flood rainfall characteristics (Figure 2.8) display a northern shift compared to flash floods. Slow-rise floods in the Northeast, Ohio River valley, and the upper Midwest are the most frequent (Figure 2.8a), have the highest average rainfall accumulation (Figure 2.8b), and largest area (Figure 2.8c), with variable durations from 50 to 250 h (Figure 2.8d). These regions displayed year-round flooding (Figure 2.4), due to frequent synoptic forcing and long-lived MCSs (Ashley & Ashley, 2008b; Kunkel et al., 2012; Schumacher & Johnson, 2006). While the duration of slow-

rise floods is only moderate in the Northeast and Ohio River valley (Figure 2.8d), long-duration (>250 h) slow-rise floods occur in the northern Great Plains and Mississippi River valley. In the northern Great Plains, slow-rise floods are somewhat infrequent, with moderate rainfall accumulation and area, occurring mostly in the spring and summer (Figure 2.4). This pattern is due to MCSs (Schumacher & Johnson, 2006) and rain-on-snow events, with the latter comprising 66% of long-duration (>250 h) slow-rise floods (Figure 2.9a; Table 2.3). The long-duration and moderately large floods in the lower Mississippi River valley are consistent with a maximum frequency of long-duration (i.e., 5 days) widespread heavy rainfall events in the Gulf of Mexico, which were caused by cool-season synoptic cyclones, tropical cyclones, and summertime convection in nine cases examined by (Schumacher & Johnson, 2009). Flood reports show that long-duration events in the lower Mississippi Valley are primarily due to cool-season heavy rainfall (Figure 2.9b; Table 2.3), showing that cool-season synoptic cyclones explain these long durations. Finally, moderate duration (~100 h) and high rainfall accumulation slow-rise floods also occur in the Pacific Northwest, due to ARs (Davis, 2001; Kunkel et al., 2012; Saharia et al., 2017a) and rain-on-snow events (McCabe et al., 2007).

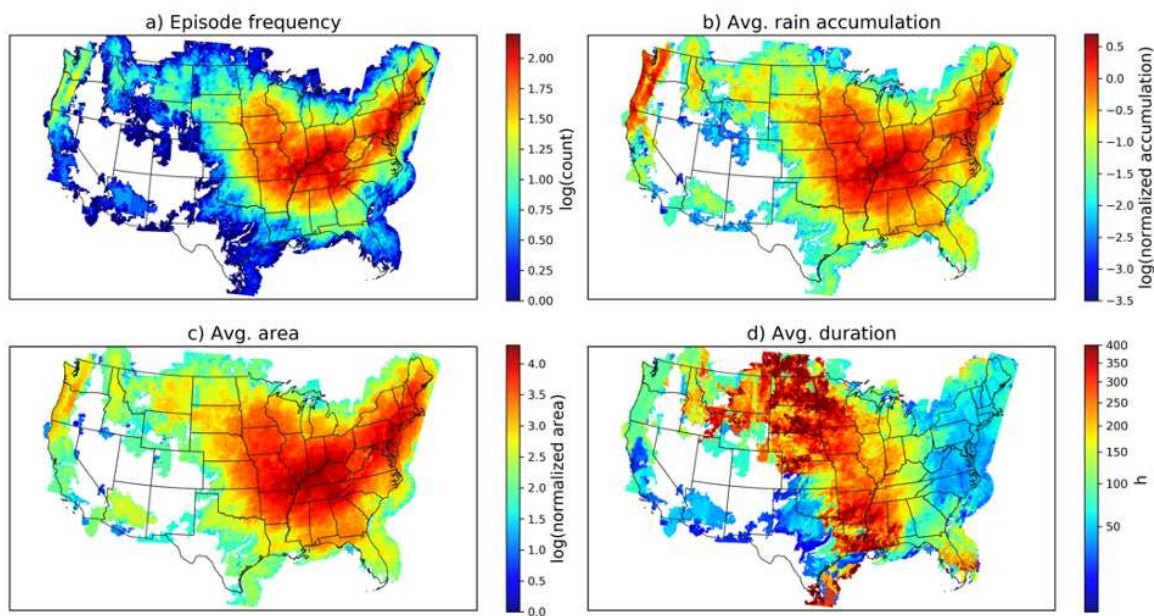


Figure 2.8: As in Figure 2.7 but for slow-rise floods.

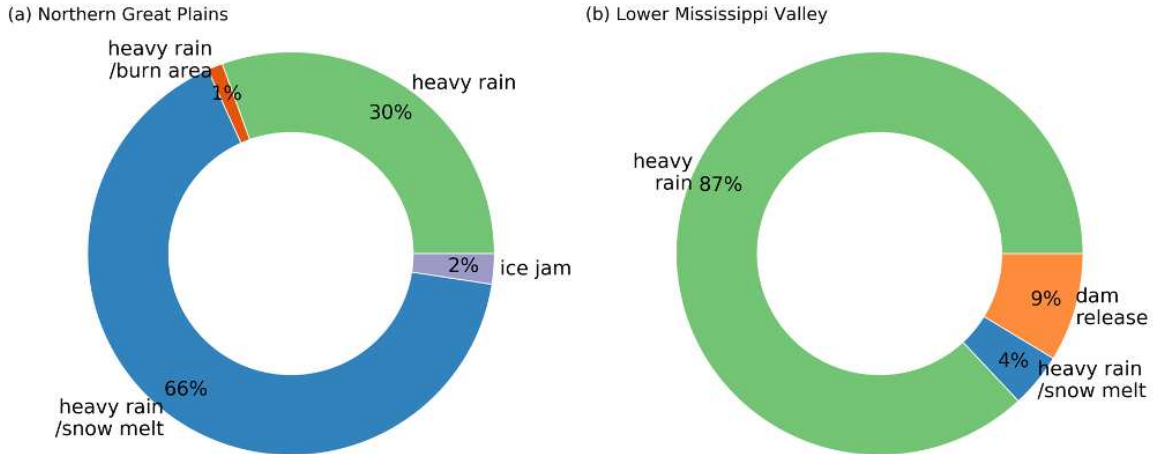


Figure 2.9: Cause of long-duration (> 250 h) slow-rise floods in the (a) northern Great Plains (n=82) and (b) lower Mississippi Valley (n=23) from post-2006 NCEI Storm Events data. The size of different colors in the circle shows the percentage of each flood cause (green= heavy rain, blue=heavy rain on snowmelt, purple=ice jam, orange= dam release, and red=heavy rain over burn area).

Table 2.3: Seasonality of long-duration (>250 h) slow-rise flood causes in the northern Great Plains and lower Mississippi Valley for causes that comprise over 25% of the total. The peak season for each flood cause in each region is bolded.

	Fall	Winter	Spring	Summer	Total
Northern Great Plains					
Heavy-rain	2%	0%	4%	24%	30%
Heavy rain/snowmelt	0%	0%	45%	21%	66%
Lower Mississippi Valley					
Heavy rain	17%	17%	48%	4%	86%

Hybrid floods display a maximum in rainfall characteristics in the central United States, Ohio River valley, and mid-Atlantic (Figure 2.10), which is between the location of maximum slow-rise and flash flood rainfall characteristics. In the central United States, Ohio River valley, and mid-Atlantic, hybrid floods occur most frequently (Figure 2.10a), have the highest average rainfall accumulation (Figure 2.10b), are the largest (Fig. 10c), and have moderate durations (40–100h;

Figure 2.10d). These locations are also where hybrid floods were frequently observed by storm reports (Figure 2.5) and are likely the result of long-lived convection, tropical cyclones (Figure 2.5), and frontal passages (Ashley & Ashley, 2008b; Kunkel et al., 2012; Villarini et al., 2014). The longest duration hybrid floods (>100 h) are observed in the Gulf Coast (Fig. Figure 2.10d), which highlights slow-moving tropical systems (Ashley & Ashley, 2008b; Villarini et al., 2014).

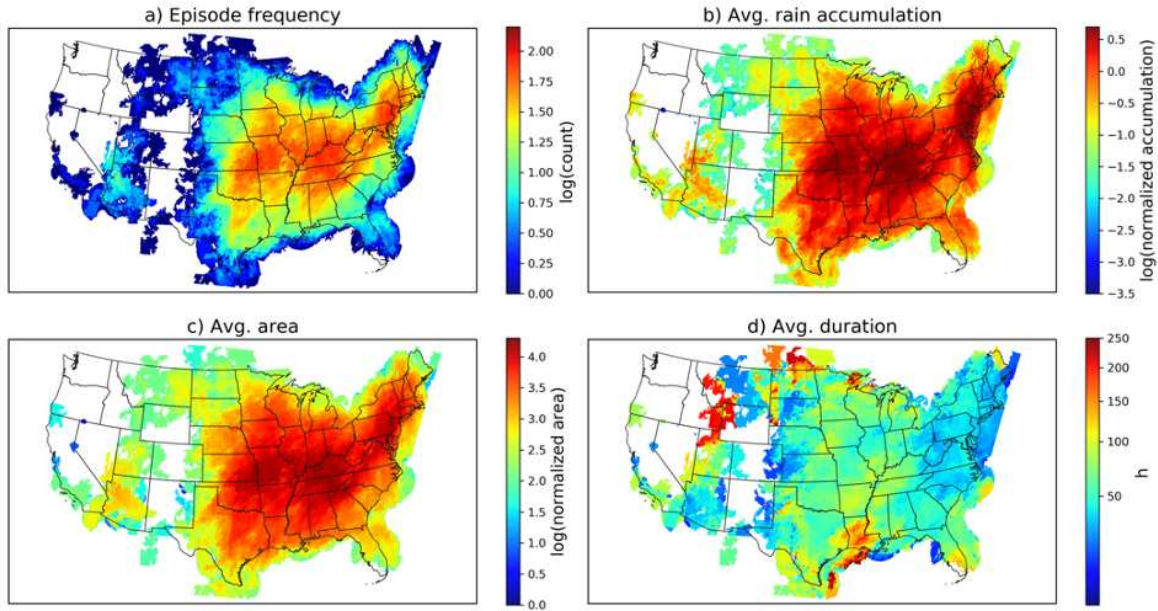


Figure 2.10: As in Figure 2.7 but for hybrid floods.

2.3.3 Comparison of rainfall characteristics in flood-producing storms

While the spatial patterns shown above suggest differences in rainfall characteristics of the different flood-producing storm types, a direct comparison most prominently exhibits these differences. The distribution of episode total rainfall accumulation (normalized by storm area; Figure 2.11a), episode maximum rain rate (Figure 2.11b), total episode duration (Figure 2.11c), and episode flood area (Figure 2.11d) are compared between flash, slow-rise, and hybrid flood-producing storms. The total rainfall accumulation normalized by storm area is used rather than area-averaged rainfall due to the varying storm sizes between the different flood types for a more

accurate comparison. Flash flood-producing storms exhibit high maximum rain rates (mean of 58 and up to 300 mm h⁻¹; Figure 2.11b), the shortest duration (<150 h; Figure 2.11c), and smallest area (Figure 2.11d), which is consistent with the convective nature of flash flood-producing storms (Davis, 2001; Doswell et al., 1996; Maddox et al., 1979). However, rainfall accumulations are only moderate (Figure 2.11a), due to the transient nature of these flood-producing storms, and maximum rain rates that are lower than hybrid flood-producing storms (mean of 71 mm h⁻¹). Given that hybrid flood-producing storms are slightly biased toward being composed of flash floods (section 2b), but with a much larger area (Figure 2.11d) and longer duration (Figure 2.11c) than flash flood-producing storms, this suggests more intense and organized storms. These characteristics of hybrid flood-producing storms result in the highest rainfall accumulation of any flood type (Figure 2.11a), due to high rain rates sustained over a long duration and large area [Eqn. 2.1]. This is despite slow-rise flood-producing storms having a longer duration (Figure 2.11c) and similarly large area (Figure 2.11d). However, slow-rise flood-producing storms have a lower maximum rain rate (mean of 50 mm h⁻¹), which explains the lower rainfall accumulations, consistent with expectations (Davis, 2001).

Differences in flood-producing storm rainfall characteristics are also summarized in Figure 2.12, where flood episode average rain rate is plotted as a function of duration, and the size of the scatter points represents the area of the flood episode. Figure 2.12 visualizes 2.1, which is a simple relationship showing that high rainfall accumulation is governed by high average rain rates sustained over a long-duration (though flood-producing storms usually exhibit a dominance of either rainfall rate or duration; Doswell et al., 1996). Note that average rain rates are calculated over the entire flood duration and area, thus yielding different results (and lower rain rates) than Figure 2.11b. This visual representation of 2.1 (Figure 2.12) thus provides insight into the dominance and importance of flood “ingredients” in the various flood-producing storm types.

From Figure 2.12, it is observed that flash flood-producing storms are intense (>up to 10 mm h⁻¹), small to moderate in size, and short duration (<100 h), while slow-rise flood-producing storms are low-intensity (<6 mm h⁻¹), large, and long-lived (>300 h) events. Hybrid flood-

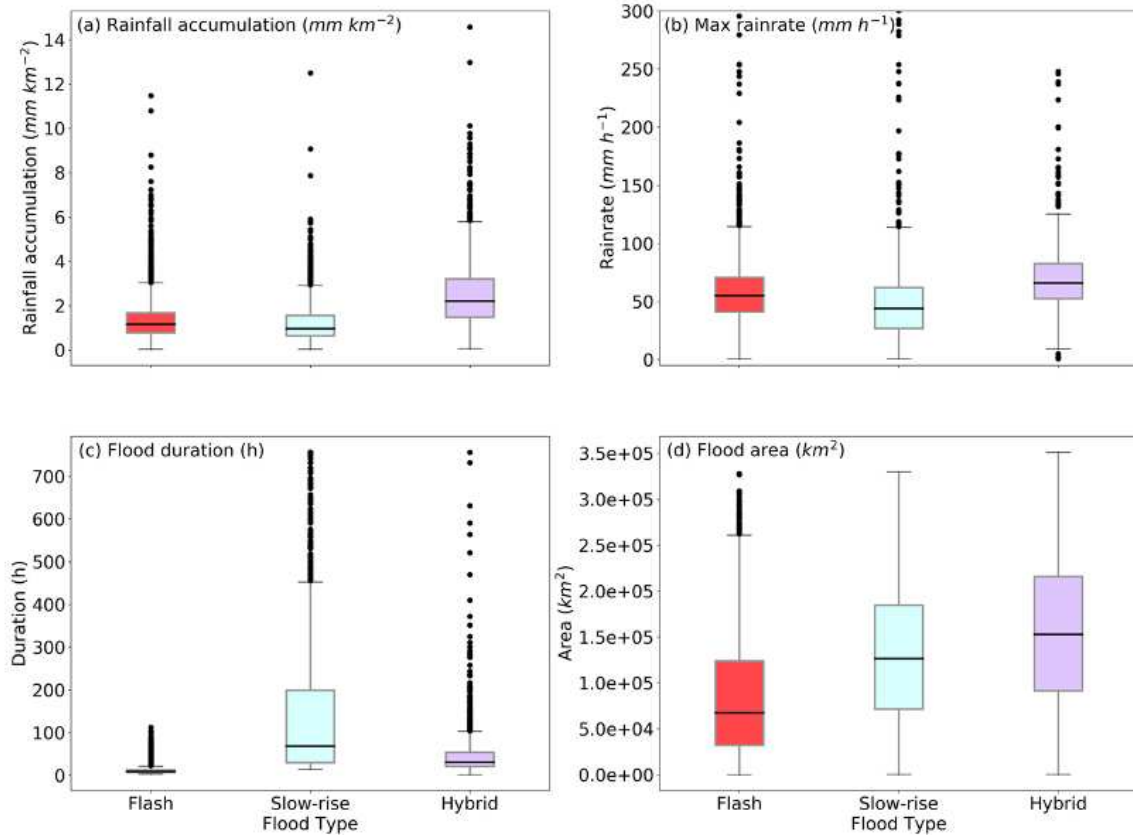


Figure 2.11: Boxplots of (a) rainfall accumulation normalized by flood area (mm km^{-2}), (b) maximum rain rate (mm h^{-1}), (c) flood duration (h), and (d) flood area (km^2) for flash (red box), slow-rise (cyan box), and hybrid flood episodes (purple box). Black dots indicate outliers.

producing storms are large and low intensity ($<6 \text{ mm h}^{-1}$) like slow-rise flood-producing storms, but with durations between flash and slow-rise flood-producing storms (generally $<300 \text{ h}$, with a few outliers). Combining this result with Figure 2.11, hybrid flood-producing storms have the highest rainfall accumulation because they have higher maximum rain rates than slow-rise floods that are sustained longer than flash flood-producing storms. This relationship for the different flood-producing storms types is consistent with Eqn. 2.1, thus providing confidence that this flood climatology is robust and accurately captures flood characteristics unique to each flood type. Such a physically realistic climatology of various flood-producing storm types over the CONUS offers insight into the specific regions at risk for different impacts posed by these floods and their unique characteristics.

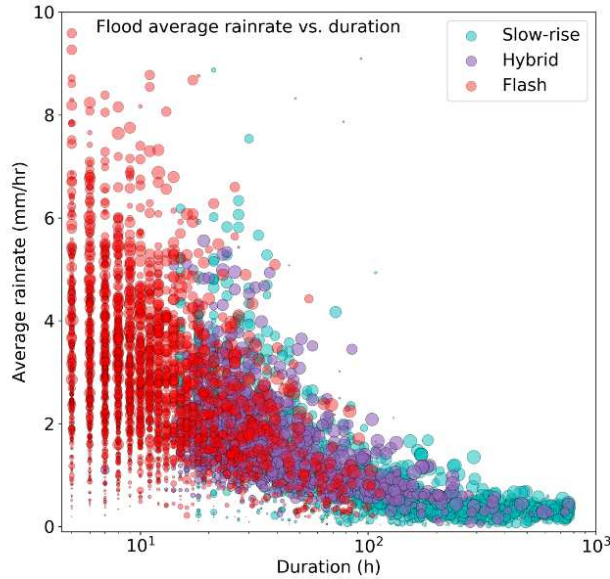


Figure 2.12: Average rain rate (mm h^{-1}) as a function of the log of duration (h) for flash (red dots), slow-rise (blue dots), and hybrid (purple dots) floods, where the size of the dot represents the area of the flood.

2.4 Conclusions

A flood-producing storm climatology over the CONUS from 2002 to 2013 was created to investigate the location, seasonality, and rainfall characteristics of flash, slow-rise, and hybrid flood-producing storms. The NCEI Storm Events Database documented where and when these floods occurred and is merged with stream gauge-indicated floods from the Shen et al. (2017) database to provide a robust indication of a significant hydrologic response to a causative meteorological event. Stage IV data supplemented the storm reports by providing rainfall data for the identified flood-producing storm cases, allowing for examination of flood-producing storm total rainfall accumulation, area, and duration. The methodology employed in this study allowed for the development of a flood-producing storm climatology over the CONUS, which is unique relative to previous studies by linking the specific meteorological rainfall characteristics to verified flood episodes. Additionally, this research fills the need for a flood climatology that examines characteristics of a range of flood-producing storm types and not just flash floods, which have been explored extensively in the literature (Brooks & Stensrud, 2000; Maddox et al., 1979; Saharia et al., 2017a).

The flood-producing storm climatology developed in this study was demonstrated to be robust, as shown by the unique seasonal, spatial, and rainfall characteristics for the different flood-producing storm types that are physically consistent with Doswell et al. (1996) and results from prior studies. Additionally, this study provides a novel perspective on floods by analyzing the detailed rainfall characteristics of numerous flood-producing storms over the CONUS. The results for each flood-producing storm type are summarized as follows:

- Flash flood-producing storms
 - Intense, short-duration, small- to moderate-sized systems with low rainfall accumulation
 - Summertime maximum (due mostly to warm season convection)
 - Occur most often east of the Rocky Mountains
 - Most frequent, highest rainfall accumulation, largest area, and moderate duration in Mississippi and Ohio River valleys
 - Moderate frequency, rainfall accumulation, and area, but longest duration in the Southwest due to the monsoon

- Slow-rise flood-producing storms
 - Low intensity, long-duration, large systems with low rainfall accumulations
 - Spring-early summer maximum
 - Occur most often in the Northeast, Ohio River valley, northern plains, and Pacific Northwest
 - Due mostly to MCSs, synoptic events (including ARs), and rain-on-snowmelt
 - Most frequent, highest rainfall accumulation, and largest area in the Northeast, Ohio River valley, and upper Midwest
 - Moderate duration and frequency, but high rainfall accumulation in the Pacific Northwest due to ARs

- Hybrid flood-producing storms
 - Moderate intensity and duration, large systems, with high rainfall accumulations
 - Late spring–early summer maximum
 - Occur most often in the central United States and the Northeast
 - Due mostly to heavy rain and tropical systems
 - Most frequent, highest rainfall accumulation, largest area, and moderate duration in the central United States, the Northeast, and mid-Atlantic

While more detailed mesoscale and synoptic processes giving rise to the unique characteristics observed in each flood-producing storm type is beyond the scope of the current study, it is reasonable to conclude that these processes differ between flood types, as suggested by Doswell et al. (1996), Davis (2001), and observed in case studies in the literature. Such cases include a flash flood from 6 to 7 May 2000 in eastern Missouri that was produced by a quasi-stationary MCS (Schumacher & Johnson, 2008), multiday AR flooding on the West Coast in December 2010 (F. Ralph & Dettinger, 2012) characteristic of slow-rise flood-producing storms, and hybrid flood-producing storms in Colorado characterized by stratiform rainfall with embedded convection due to persistent upslope flow of moist neutral air (Gochis et al., 2015). Given the consistency of characteristics observed in flood-producing storms from this study with previous work, the mesoscale and synoptic dynamics unique to the aforementioned floods likely explain some of the observed differences among flood types in this climatology. It is important to study the full-spectrum of flood types, as was done in this study, given the range of behaviors exhibited in the different flood-producing storm types. The nature of this flood-producing storm climatology provides the potential to be useful for research and operational applications, especially considering the unique impacts that might result from different flood-producing storm types. An extensive documentation of where, when, how often, and how much rainfall occurred from different flood-producing storm types is valuable information for emergency managers, city planners, and policy makers seeking efforts to protect their communities against flood-related risks.

Furthermore, the characteristics of these flood-producing storms provide a baseline for understanding the nature of these storms in a current climate so that potential future changes associated with a warming climate can be more accurately assessed. One application of this in future work is the utilization of high-resolution, convection-permitting simulations over the CONUS from 2002 to 2013 of the current and future climate (Liu et al., 2017) to examine potential changes to high-impact flood-producing storms from this climatology. This planned future work is similar to the Gutmann et al. (2018) study of hurricanes in a current and future climate, who finds higher precipitation rates in future hurricanes, providing further motivation for studying flood-producing storms in a future climate. These simulations will allow for an understanding of how the physical processes, in addition to the observed characteristics, of flood-producing storms in a future climate might change. Thus, this flood-producing storm climatology is one step toward a better understanding of the complex water, weather, and energy relationships in a current and future climate that can help inform the use of water-resources and risk posed by these disasters over the CONUS.

Chapter 3

The Role of Precipitation in Flood Occurrence and Distribution in Topographically Variable Basins

3.1 Introduction

Floods are one of the deadliest weather-related natural disasters in the continental United States (CONUS; Ashley & Ashley, 2008a), with nearly 41 million people currently exposed to a 1-in-100-year flood (Wing et al., 2018). In spring 2019, locations along the Mississippi River experienced record flood stages and the longest lasting floods since 1927, totaling over three months in duration (Donegan, 2019; NWS, 2019). The record Mississippi River flooding was caused by a unique combination of ingredients during the spring of 2019—rapid snowmelt, saturated soils, and heavy rainfall (NWS, 2019). This concatenation of atmospheric, topographic, and hydrologic factors is necessary for floods to occur, though the relationship between these three systems is complex (Davis, 2001).

To better understand the connection between the various mechanistic drivers of flooding, studies have examined rainfall-streamflow relationships of floods. Stephens et al. (2015) analyzed the link between flood frequency, spatial extent, and duration with river discharge and monthly precipitation in major global rivers. They found that mean monthly precipitation derived from a re-analysis dataset (ERA-Interim) was not well correlated with global flood activity, which Stephens et al. (2015) attributes to the nonlinearity of flood activity and rainfall, as well as regional and seasonal differences. Berghuijs et al. (2016) further investigated the role of different flood-generating mechanisms over the CONUS and the ability of those mechanisms to explain the variability in maximum annual streamflow. Regional and seasonal patterns in streamflow are poorly explained by rainfall alone, and Berghuijs et al. (2016) show that precipitation-excess (i.e., rainfall excess compared to soil moisture storage capacity) is a more important contributor to maximum annual

streamflow. However, Villarini and Slater (2018) demonstrated that rainfall is closely related to streamflow when examining temporal changes in stream gage height associated with changes in storm total precipitation over the CONUS. Storm total precipitation shows regional differences in relation to streamflow, displaying a greater importance on the West Coast and east of the 100th meridian (Villarini & Slater, 2018). Additionally, Slater and Villarini (2016) showed that agreement in precipitation and stream gage height increases in large and low-lying areas, highlighting the more nuanced variability in precipitation and streamflow trends.

These previous studies generally do not find a strong agreement between streamflow and rainfall, which is important for understanding the nonlinearity of rainfall and streamflow processes operating in floods. However, relatively weak associations between these variables is not surprising, because many of these prior studies used coarse precipitation data that is averaged over large spatial or temporal scales (Stephens et al., 2015), and the studies did not consider storm-scale precipitation (aside from Villarini & Slater, 2018, but even they used basin-averaged daily values). Simply examining maximum annual discharge in relation to statistics of monthly or annual precipitation masks the ability of individual storms to cause floods on the scale of hours to days, such as the Big Thompson Canyon and Rapid City flash floods (Maddox et al., 1978), Colorado floods of 2013 (Gochis et al., 2015), or Hurricane Harvey-related flooding in 2017 (NHC, 2018).

The purpose of this study is to fill this gap by examining flood rainfall-streamflow relationships in two different river basins (the Wabash and Willamette basins) in the CONUS using high-resolution precipitation data from a climatology of flood-producing storms and streamflow during these flood events. The inter-basin variability in flood rainfall and discharge is examined to gain a more detailed understanding of flood behavior in two topographically and climatically different river basins. Such an approach paints a more nuanced picture of the variability in the topographic, climatic, atmospheric, and hydrologic processes operating in floods on local scales, which warrants further understanding to protect local communities against flood-related risks.

3.2 Methods

3.2.1 Flood data

Floods in two U.S. river basins—the Wabash and Willamette basins—were identified from a climatology of flood-producing storms over the CONUS from Chapter 2. This database identified floods from 2002–2013 using the National Centers for Environmental Information (NCEI) Storm Events database merged with a database of streamflow-indicated floods (Shen et al., 2017). A storm-centric view of floods with a notable hydrologic response is provided by this database in using only the NCEI flood reports (grouped into separate “episodes” by their associated meteorological system) that were close in space and time with flooded stream gauges identified from Shen et al. (2017). Both flash and slow-rise floods are included in this database: flash floods are defined by the National Weather Service as “a rapid and extreme flow of high water into a normally dry area, or rapid water level rise in a stream or creek above a predetermined flood level, beginning within six hours of the causative event (e.g., intense rainfall, dam failure, ice jam-related),” and slow-rise floods are defined as “the inundation of a normally dry area caused by an increased water level in an established watercourse, or ponding of water, generally occurring more than six hours after the causative event, and posing a threat to life or property” (NWS, 2007). Using this methodology, 3436 (2102) flash (slow-rise) flood-producing storms over the CONUS comprise the flood database (see Chapter 2), and the data is clipped to the boundaries of each respective river basin to study both flash and slow-rise flood-producing storms in each basin.

Rainfall information for each flood-producing storm in the Wabash and Willamette basin is gathered from the Chapter 2 flood database. Hourly, 4-km Stage IV (Lin & Mitchell, 2005) rainfall information for each flood is collected over the whole duration of each flood within $\pm 5^\circ$ latitude and longitude of the flood centroid. While Stage-IV has well-documented issues over the western U.S. (which includes the Willamette basin; Nelson et al., 2016), when compared to the Parameter-elevation Regression on Independent Slopes Model (PRISM) dataset (Daly et al., 2008), results are similar (not shown). To isolate the heavy, flood-contributing rainfall for each flood, only the largest contiguous area where rainfall accumulations exceeded the 75th percentile

are used. Instantaneous streamflow for USGS stream gauges is obtained over the flood duration for all gauges in the flood domain ($\pm 5^\circ$ latitude and longitude from the flood centroid) for each flood. The flood discharge is normalized by contributing area to reduce the effect of catchment area on river discharge (e.g. larger catchment areas tend to produce greater flows). Relationships between average gridded flood rainfall and average discharge for stream gauges in the Wabash and Willamette basins are explored, and Spearman rank correlations for rainfall closest to the stream gauge discharge provide a quantitative metric to better understand this relationship for floods in different basins. While performing a temporal or spatial lag between flood rainfall and streamflow would provide a more comprehensive representation of rainfall and streamflow relationships, doing so would add additional complexity that is beyond the scope of the study.

3.2.2 *Description of river basins*

The Wabash and Willamette river basins are selected because they contain contrasting topography, hydrologic characteristics, and atmospheric regimes. The Wabash River basin has a drainage area 85,237 km² and is located primarily in Indiana (Figure 3.1). Topography in the Wabash River basin is fairly flat, ranging in elevation from approximately 107–360 m, with the highest topography located in the central to northeast portion of the basin and lower terrain to the south. Both flash and slow-rise floods are encountered throughout the year (Figure 3.2a), with most flash floods occurring during the warm season from May–July (likely due to convective storms), and slow-rise floods occurring during the cool-season from December–March.

The Willamette River basin is situated in northwest Oregon, with the Coast Range to the west and the Cascade Mountains to the east (Figure 3.1). It is thus defined by more complex terrain than the Wabash basin, ranging in elevation from 3–3,050 m (Shearman, 1976). The Willamette River has a drainage area of 29,730 km² and is Oregon’s largest river basin (Robins, 2019; Shearman, 1976). Due to its location in the Pacific Northwest, the Willamette River Basin experiences slow-rise floods from November through March (Figure 3.2b) due to atmospheric rivers, which are highly concentrated water vapor plumes associated with extratropical cyclones coming off the

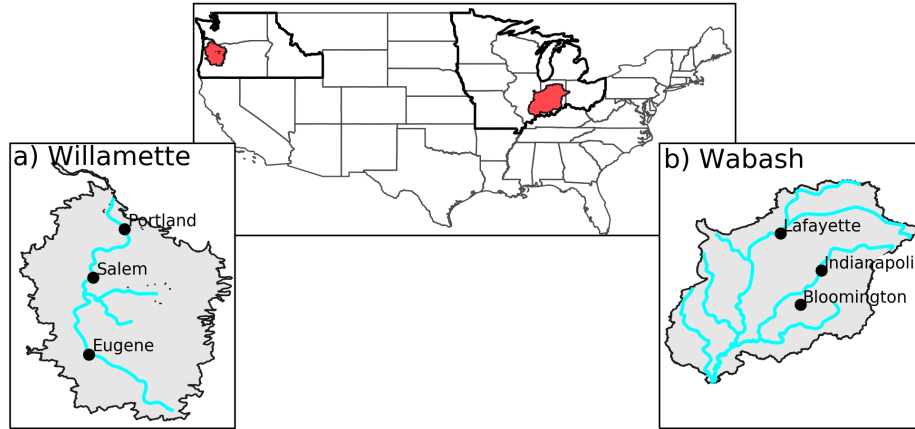


Figure 3.1: The two basins used for analysis in study. The Willamette basin (a) is located in Oregon, next to the Coastal (Cascade) Mountains to the west (east) and is characteristic of the Pacific Northwest (black outline). The Wabash basin (b) is located in Indiana and parts of Illinois and Ohio and is characteristic of a relatively flat river basin in the Midwest (black outline).

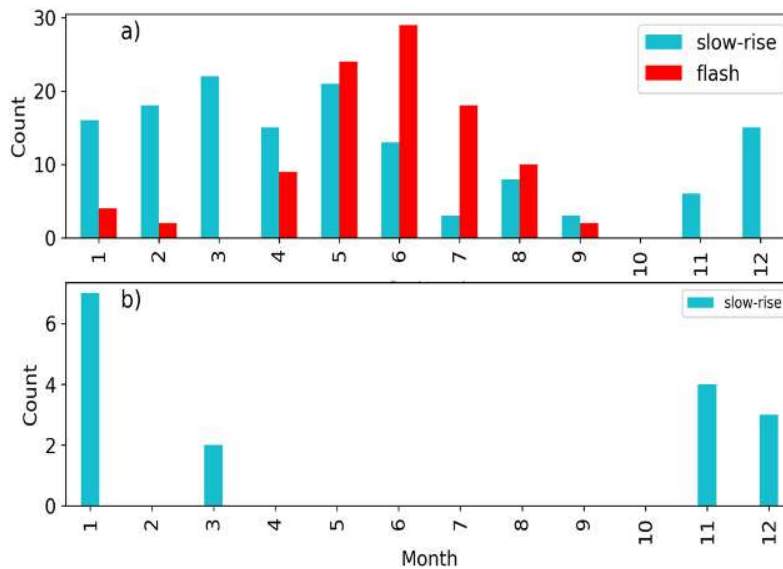


Figure 3.2: a) Seasonality of flash (red) and slow-rise (blue) floods in the Wabash basin by month. b) as in a), but for the Willamette basin. Floods are identified using a flood database from Chapter 2.

Pacific Ocean (Neiman et al., 2008), other extratropical cyclone-related precipitation, and rain-on-snow events (Berghuijs et al., 2016; Stephens et al., 2015; Villarini & Slater, 2018). Only two flash flood episodes occurred in the Willamette basin during 2002–2013 and therefore are excluded from further analysis. The Willamette basin, which contains complex terrain and experiences cool-season slow-rise floods, provides an ideal contrast to the flatter, inland Wabash basin, which experiences both flash and slow-rise floods year-round.

This contrast between the Wabash and Willamette basins yields a useful framework from which to analyze detailed flood rainfall-streamflow relationships. While only two basins are selected for analysis, they are representative of larger climatic regimes and geographical areas. The Wabash basin exemplifies a typical flat Midwest basin that experiences flooding year-round due to extratropical cyclones and convective storms, with larger organized mesoscale convective systems (R. A. Houze Jr, 2004) dominant during the summer months (Ashley & Ashley, 2008b; Kunkel et al., 2012; Schumacher & Johnson, 2006). Meanwhile, the Willamette basin is characteristic of the Pacific Northwest region of the U.S., with complex terrain and flooding primarily confined to the cool-season due to atmospheric rivers and extratropical cyclones (Kunkel et al., 2012; Saharia et al., 2017b). Given the large difference in storm mechanisms driving floods in each basin, analyzing flood rainfall-streamflow relationships in these two basins can provide an inference to flood behavior typical of the Midwest and Pacific Northwest, though further work is necessary to extrapolate results beyond the Wabash and Willamette basins.

3.3 Results

3.3.1 *Flood rainfall and streamflow in the Wabash Basin*

Results show that flash and slow-rise floods occur throughout the Wabash basin, and both types of floods occur most frequently in the furthest downstream regions of the basin (indicated by the color gradient in Figure 3.3a, c). For flash floods, 20–60 floods occurred between 2002–2013 in the northern half of the basin, whereas 80–120 floods occurred in the southern half of the basin during the same time period (Figure 3.3a). Slow-rise floods also exhibit a north-to-south gradient with a maximum of over 150 slow-rise floods occurring in the southeast Wabash basin (Figure 3.3c). The similar spatial variability among flash and slow-rise floods suggests that the interplay between the topography, hydrology, and meteorology creates a preferential hotspot for floods in Wabash basin.

The spatial distributions of average rainfall (indicated by the color gradient in Figure 3.3b, d) and discharge (indicated by the black dots in Figure 3.3b, d) associated with flash and slow-rise floods exhibit more variability than distributions of flood occurrence. The maximum rainfall

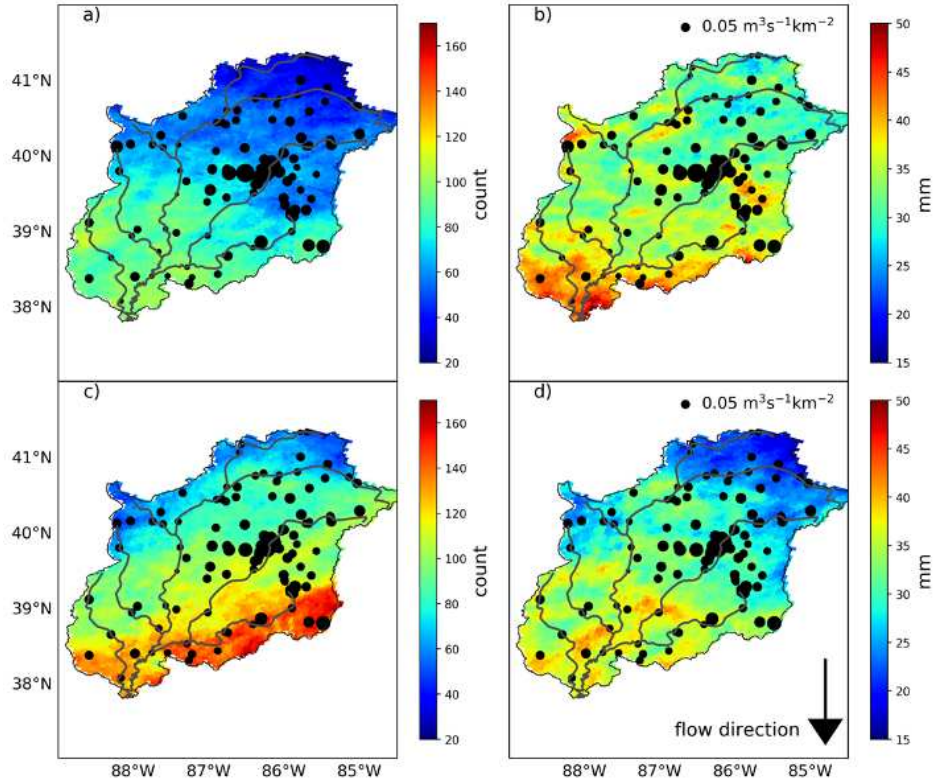


Figure 3.3: a) Number of flash flood episodes in the Wabash basin. b) Average flash flood rainfall in the Wabash basin. c) and d), as in a) and b), respectively, except for slow-rise floods. Black dots show average flood discharge (normalized by catchment area), where larger dots = higher discharge ($\text{m}^3 \text{s}^{-1} \text{km}^{-2}$). The black arrow shows the general north-to-south direction of river flow.

associated with flash floods occurs in the southern part of the Wabash basin, reaching values of 50 mm on average. More localized maxima in average flash flood rainfall occurs throughout the basin, particularly in the central Wabash basin, which indicates the transient and localized nature of flash flood-producing storms. Average flash flood discharge does not directly match the spatial variability of flash flood average rainfall, with maxima (i.e., the larger dots in Figure 3.3b) located in the central region of the basin. The maxima of flash flood discharge coincide with the location of Indianapolis and higher terrain, suggesting that urbanization and topography (however slight) influence flood discharge trends, which has been previously documented (Ashley & Ashley, 2008a; Davis, 2001; Saharia et al., 2017a; B. K. Smith & Smith, 2015). The maximum slow-rise flood discharge (Figure 3.3d) is similarly located in the central and eastern portion of the Wabash, again showing the importance of the basin's topography and land use. Slow-rise flood average

rainfall displays a broader maximum in the southern half of the basin, with lower maximum rainfall amounts of 40 mm. Such a result is consistent with the larger area and less intense nature of slow-rise flood-producing storms (Chapter 2), which tend to be caused by synoptic systems.

To provide a more quantitative understanding of flood rainfall-discharge relationships, correlations between flash and slow-rise flood rainfall and discharge were analyzed. When aggregated across the entire Wabash basin, the correlation between flash (slow-rise) flood rainfall accumulation and river discharge is -0.037 (-0.027; Figure 3.4). The correlation between discharge and flood frequency is also weak in flash (slow-rise) floods, with a value of -0.07 (-0.015). While the flood rainfall/frequency-discharge correlation is weak, correlations between elevation and rainfall as well as elevation and discharge are stronger in floods. The correlation between elevation and rainfall in flash (slow-rise) floods is -0.6 (-0.67) and the correlation between elevation and discharge in flash (slow-rise) floods is 0.36 (0.34). Therefore, while basin-wide correlations between flood rainfall and frequency with discharge are weak, both flood rainfall and discharge exhibit a stronger relationship with elevation. Such a result is possible because flood rainfall has a strong negative correlation with elevation, but flood discharge has a moderate positive correlation with elevation. This relationship suggests that flash and slow-rise flood rainfall maximizes where elevation is lower while flash and slow-rise discharge maximizes where elevation is higher. Such relationships can be visualized in Figure 3.3, where flash and slow-rise flood rainfall typically maximizes in the southern Wabash basin and discharge maximizes upstream in the central Wabash basin.

Whereas rainfall-discharge correlations across the entire basin fail to capture the spatial variability in the Wabash basin, correlations of flood rainfall at individual stream gauges yield higher correlations (Figure 3.5). Both flash (Figure 3.5a) and slow-rise (Figure 3.5b) floods display correlations over 0.75 in much of the central Wabash basin located near Indianapolis and higher terrain (~400 m; darker contours). This suggests a non-negligible role of a slight terrain gradient and urbanization on concentrating rainfall and discharge, similar to the effect of the Balcones Escarpment in central Texas (Caracena & Fritsch, 1983; Nielsen et al., 2016; J. A. Smith et al., 2000).

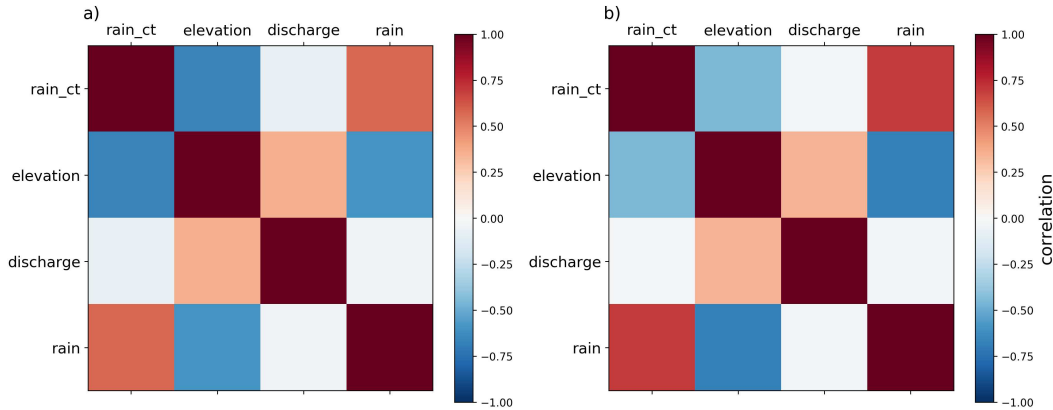


Figure 3.4: Correlation matrix of flood frequency (rain_ct), gauge elevation (elevation), flood average discharge (discharge), and flood average rainfall (rain) averaged across the entire Wabash basin for a) flash floods and b) slow-rise floods.

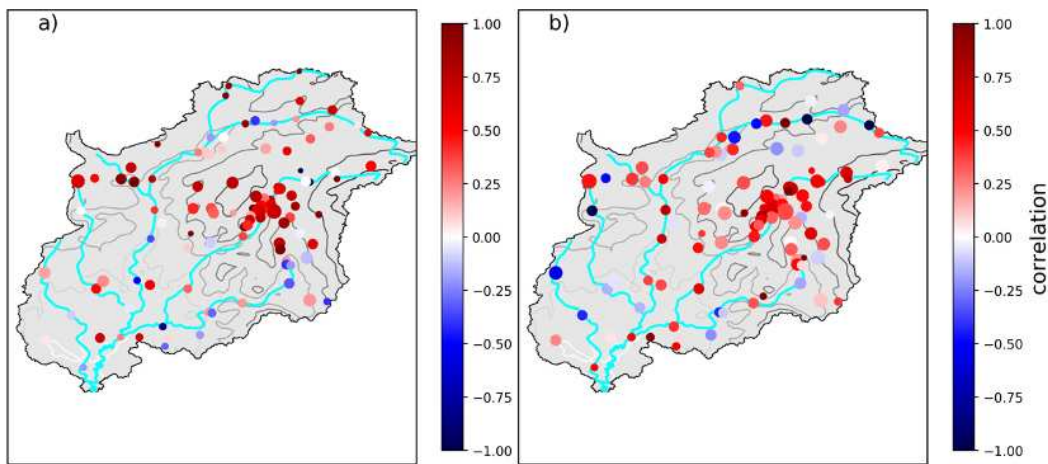


Figure 3.5: Correlation between average discharge and average rainfall at each stream gauge for a) flash floods, and b) slow-rise floods. Blue lines depict major rivers, while grey contours depict topography (darker contours=higher topography).

3.3.2 Flood rainfall and streamflow in the Willamette Basin

In the Willamette basin, slow-rise floods occur most often in the western and northeastern regions of the basin, areas that both border mountain ranges (see Section 3.2), with a maximum of 30 slow-rise floods from 2002–2013 (indicated by the color gradient in Figure 3.6a). The fewest number of slow-rise floods occur in the central part of the basin, bordering the Willamette river (north-south river/ black line in the basin). Similarly, the maximum average slow-rise flood rainfall occurs in the western and northeastern regions of the basin, reaching average values of 150–225

mm (Figure 3.6b). The spatial trends in slow-rise flood discharge are more complex than flood occurrence or average rainfall, but a maximum is observed in the central western Willamette basin, coinciding with the maximum in slow-rise flood occurrence and rainfall. Thus, while topography showed some importance in the Wabash basin, the higher topography in the Willamette basin displays a more prominent influence on the spatial variability of slow-rise flood rainfall and occurrence. Such a result is unsurprising, as the high terrain in the Pacific Northwest acts to focus and enhance rainfall in the stable, moist airmass characteristic of extratropical cyclones and associated atmospheric rivers coming off the Pacific Ocean (Neiman et al., 2008). This appears to exhibit some influence on slow-rise flood discharge as well, at least in the central western Willamette basin, though elsewhere, discharge is spatially variable.

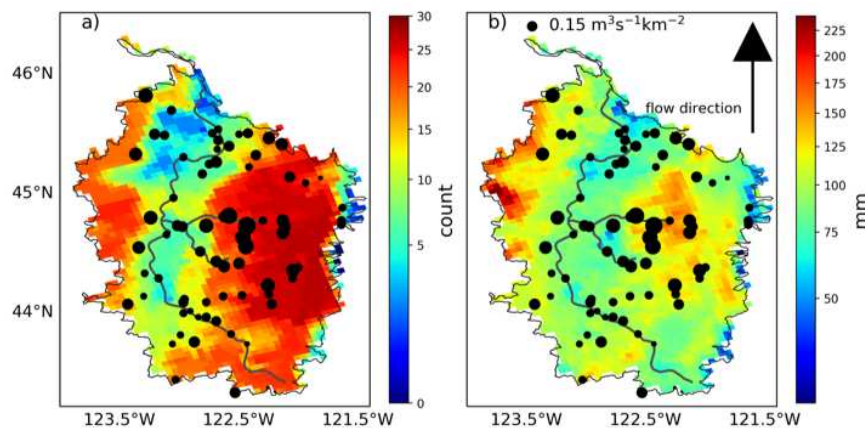


Figure 3.6: a) Number of slow-rise flood episodes in the Willamette basin. b) Average slow-rise flood rainfall in the Willamette basin. Black dots show average flood discharge (normalized by catchment area), where larger dots = higher discharge ($\text{m}^3 \text{s}^{-1} \text{km}^{-2}$). The black arrow shows the general south-to-north direction of river flow.

The variability in slow-rise flood discharge from Figure 3.6 creates a less clear spatial pattern in slow-rise flood discharge and rainfall correlations. Basin-wide, this correlation is 0.43 (0.35) between flood rainfall (frequency) and discharge (Figure 3.7). Slow-rise flood rainfall exhibits a weak correlation with elevation of 0.12, with an even weaker correlation between flood discharge and elevation of -0.096. Weak correlations in flood rainfall and discharge with elevation are likely

due to maxima in flood rainfall and discharge in areas near complex terrain in the west-central portion of the Willamette basin as well as the flatter central Willamette basin (Figure 3.6b).

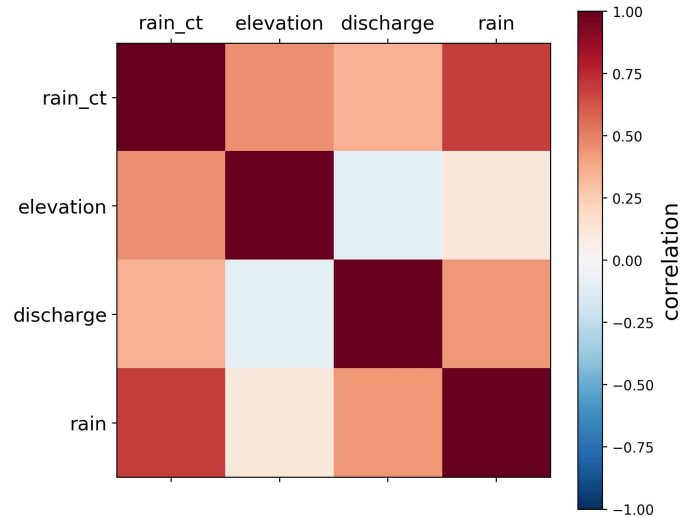


Figure 3.7: As in Figure 3.4, but for the Willamette basin.

Similar to the Wabash basin, the basin-average Willamette correlation misses much of the spatial variability in the rainfall-discharge correlation shown in Figure 3.6. The Willamette slow-rise flood rainfall and discharge correlation map paints a complicated picture, in that stream gauges with strong negative correlations are located just downstream of stream gauges with strong positive correlations in many instances (Figure 3.8). Along the Willamette River itself (north-south river in the middle of the basin), high positive correlations exist (up to nearly 1.00), while on many of the tributaries, strong negative correlations exist (particularly in the northern and southern Willamette), down to nearly -1.00. Notice that many of the high elevation stream gauges (i.e., western-most gauges in the basin) also have high positive correlations above 0.75.

The influence of dams on flood rainfall-streamflow correlations are shown in Figure 3.8, with dams having heights greater than 30 m plotted in triangles, and larger dams indicated by larger triangles. Most of the dams are located along tributaries (Figure 3.8; Shearman, 1976), which could explain how strong positive correlations in rainfall and discharge are located right next to strong negative correlations. While dams exist in the Wabash basin (not shown), the type of dam manage-

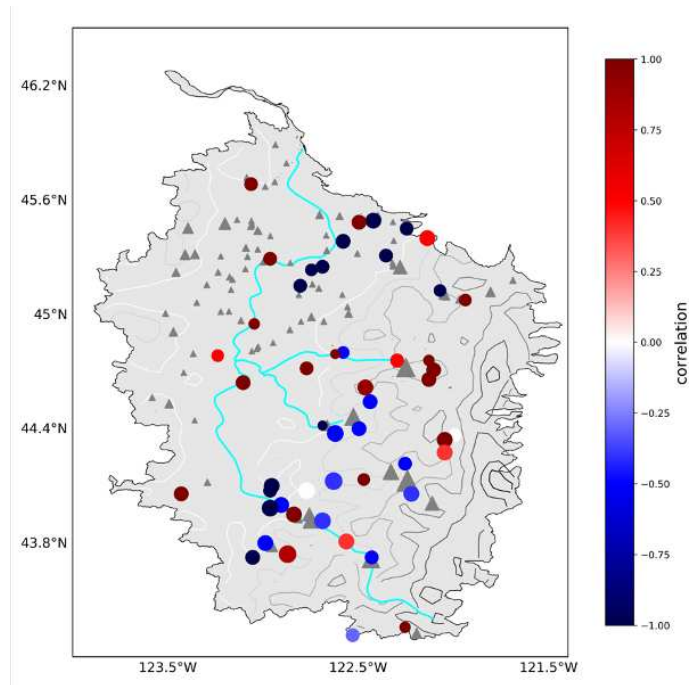


Figure 3.8: Correlation between average discharge and average rainfall at each stream gauge for slow-rise floods. Blue lines depict major rivers, grey contours depict topography (darker contours=higher topography), and grey triangles show dams >30 m height, where the size of the triangles indicate the relative dam height.

ment is different in the Willamette basin, since the majority of precipitation (and flooding) occurs in the winter in the Willamette (Figure 3.2; Neiman et al., 2008; Saharia et al., 2017b) and necessitates a greater storage of water in order to provide water throughout the year (of Engineers, n.d.; Shearman, 1976). Furthermore, the creation of dams in the Willamette basin have substantially modified streamflow, such that locations that experienced a 1-in-10-year peak streamflow pre-dam construction now are more similar to a 1-in-100-year event (Benner & Sedell, 1997). These insights suggest that in addition to the local variability in topography, hydrology, and precipitation that influence flood rainfall-streamflow relationships, water management is an important factor too, which has not received as much attention in the literature.

3.4 Discussion

While the present study only considers two different river basins in the U.S., these results have broader implications to flood rainfall-streamflow relationships in general. First, examining

basin-wide flood rainfall-streamflow correlations leads to a misleading understanding that rainfall-streamflow correlations are weak, whereas correlations are actually spatially variable in both the Wabash and Willamette basin, with some locations in each basin displaying stronger correlations than previously reported in the literature (e.g. Stephens et al., 2015). These strong positive flood rainfall-streamflow correlations do not imply that flood maximum discharge and flood maximum rainfall are directly collocated (as seen in the Wabash basin; Figure 3.3), as previous studies have noted (Berghuijs et al., 2016), but rather that high flood rainfall is strongly correlated with high flood discharge in particular locations. That is, maximum flood rainfall does not necessarily directly translate to maximum flood discharge, but on a localized scale, high flood rainfall is strongly tied to peaks in flood discharge.

This result highlights the importance of using high-resolution rainfall data from individual storms, given the ability of these storms to produce markedly different streamflow responses depending on the terrain, hydrologic, and land-use characteristics in different basins. Villarini and Slater (2018) found that this storm-total precipitation drove temporal changes in annual maximum gauge height in the eastern half of the U.S. and along the West Coast—the locations of the Wabash and Willamette basins, respectively. Therefore, relating coarse precipitation data averaged over timescales greater than several days in flood events (e.g. Stephens et al., 2015), masks the ability of individual storms on short timescales to produce precipitation that exhibits a stronger relationship to regional streamflow patterns in floods. Although other factors influence flood rainfall-streamflow relationships—soil moisture, snow cover, river network configuration, and land-surface—the present study emphasizes that high-resolution flood-producing storm precipitation data is necessary to gain a more nuanced understanding of this relationship.

Additionally, the Wabash and Willamette basins are characteristic of larger geographic and climate regimes, so flood rainfall-streamflow relationships might be similar in other basins, though further research is needed to quantify this. The Wabash basin is characteristic of an inland, fairly flat basin that receives flooding year-round due a variety of systems including extratropical cyclones, fronts, and summertime mesoscale convective systems (Ashley & Ashley, 2008b; Kunkel et

al., 2012; Schumacher & Johnson, 2006). Preferred locations of strong positive rainfall-streamflow correlations exist near a slight terrain gradient and urban center, which could act to concentrate rainfall and discharge, similar to the flooding hotspot in the Balcones Escarpment in central Texas (Caracena & Fritsch, 1983; Nielsen et al., 2016; J. A. Smith et al., 2000). This enhances flood risk in this area and is important to consider when determining where to develop land and require flood insurance.

The Willamette basin, on the other hand, is characteristic of mountainous Pacific Northwest basins that experience cool-season floods due to stable atmospheric conditions associated with extratropical cyclones and atmospheric rivers impinging upon the complex terrain to produce orographic rainfall (Kunkel et al., 2012; Neiman et al., 2008; Saharia et al., 2017b). The orographic rainfall signature is clearly seen by the maximum rainfall occurrence and accumulated rainfall from flood-producing storms in the west and northeast regions of the basin that border the Cascade and Coastal Mountain Ranges, respectively. While these locations also exhibit strong positive rainfall-streamflow correlations, elsewhere this relationship is less clear, likely due to the presence of rain-on-snow flood events (Berghuijs et al., 2016; Stephens et al., 2015; Villarini & Slater, 2018), which also can be generated by extratropical cyclones and atmospheric rivers (Neiman et al., 2008). Though a specific identification of rain-on-snow floods in the Willamette basin does not occur in the present study, this could be a possible explanation for the lack of clear spatial patterns in flood rainfall-streamflow correlations, since these floods are different in character than purely rainfall-driven floods.

Additionally, dams likely muddle the flood rainfall-streamflow relationship in the Willamette basin, as they occupy 27% of the upper portion of the basin (Benner & Sedell, 1997). The influence of dams on modifying flood behavior is important to take into account in different regions of the world given the diversity of dam management that depends on the local climate. Such man-made alterations have been mentioned before by Mallakpour and Villarini (2015) in explaining the discrepancy between the increasing (decreasing) frequency of rainfall (flood events) in Nebraska and Kansas. This suggestion from Mallakpour and Villarini (2015), along with the flood rainfall-

streamflow relationships in the Willamette basin, point to the role of water management in addition to topography and flood-producing storm mechanisms on sub-basin flood risk variability.

3.5 Conclusions

This study examines the sub-basin scale relationship between rainfall and streamflow during flood-producing storm events in the Wabash and Willamette River basins—two topographically and climatically different river basins. Such a high-resolution spatial analysis between flood-producing storm rainfall data and instantaneous streamflow data within individual floods on a sub-basin scale has not been previously examined. Results highlight the utility in conducting a high-resolution spatial analysis given the spatial variation in flood rainfall-streamflow relationships both in and between river basins. In the Wabash basin, a majority of flood events occur in the southern portion of the basin, though maxima in flood rainfall differs between flash and slow-rise floods. Rainfall and discharge correlations exceed 0.75 in the central Wabash basin for flash and slow-rise floods, which coincides with a heavily urbanized area as well as higher topography. High positive rainfall-discharge correlations are also observed in the Willamette basin along the Willamette River and high terrain, but there is greater spatial variability in these correlations. In addition to having more complex terrain and a different climate compared to the Wabash basin, it is hypothesized that differences in flood rainfall and discharge correlations in the Willamette basin are partially due the influence of rain-on-snow floods as well as different water management strategies. This study illustrates that not only are high-resolution storm-scale rainfall and discharge data important for understanding flood behavior, but water management strategies influence these relationships, which is not often considered in similar research. These results are therefore useful for water managers and the risk management community that need detailed, local information about flood discharge and rainfall in order to effectively utilize water resources and protect communities against flood-related hazards.

Chapter 4

Changes in Future Flash Flood-Producing Storms in the U.S.

4.1 Introduction

Floods in the continental United States (CONUS) cause tremendous damage, accounting for over \$123.5 billion in adjusted losses from 1980–2018 (A. B. Smith, 2019). High intensity, short duration flash floods are particularly problematic, as such events are caused by interactions between the atmosphere, land-surface, and hydrology, consequently making forecasting these events challenging (J. M. Fritsch & Carbone, 2004; Herman & Schumacher, 2018a; Sukovich et al., 2014). Due to their transient and complex nature, flash floods can cause enormous destruction. In May 2010, several quasi-stationary mesoscale convection systems (MCSs) led to flash floods in the south-central CONUS, resulting in over \$2 billion of damage (Lackmann, 2013; Moore et al., 2012; NWS, 2011). In south-central and eastern Texas, a lower-level prefrontal trough and warm-air advection resulted in over 305 mm of rainfall on 31 October 2013, which caused \$100 million dollars of damage and four fatalities in the Austin, Texas area (Nielsen et al., 2016).

Contributing to the difficulty of forecasting extreme rainfall and flash floods are the myriad of ingredients necessary to result in these high-impact events. Maddox et al. (1980, 1979) helped to elucidate this issue by categorizing flash floods into four categories of similar synoptic conditions over the CONUS—synoptic events, frontal events, mesohigh events, and Western events (Maddox et al., 1979)—and this led to improved predictability of weather scenarios that produced extreme rainfall. Western events were further decomposed into four distinct synoptic categories, due to their difference from central and eastern CONUS flash flood conditions. Type I Western events were those with a 500 mb shortwave trough moving northward up the western side of a long-wave ridge, while Type II Western events had a shortwave 500 mb trough moving southward down the

eastern side of a long-wave ridge. Type III events had conditions characteristic of atmospheric rivers (ARs), where strong synoptic systems with stable airmasses resulted in widespread floods, and Type IV events were associated with the Southwest monsoon (Maddox et al., 1980). The pattern recognition of these common synoptic environments associated with flash floods is often used to forecast such events (Funk, 1991). In addition to common synoptic patterns, common atmospheric “ingredients” lead to flash floods and are also used from a forecasting perspective, as discussed by Doswell et al. (1996). These ingredients include sufficient upward motion, moisture, and precipitation efficiency to sustain high rain rates over a period of time (Doswell et al., 1996). Land surface conditions also contribute to flash flooding, with terrain gradients, land-use type, and antecedent soil moisture conditions modulating flash flood occurrence (Berghuijs et al., 2016; Davis, 2001; Kumar et al., 2014; Saharia et al., 2017a; A. Schroeder et al., 2016b).

Given the destructive nature of floods in the current climate, it is necessary to understand how they may change in a future warmer climate. Future flood risk has been examined globally and in the CONUS using flood inundation models and flood exposure estimates under various population growth scenarios (Hirabayashi et al., 2013; Wing et al., 2018). While these studies highlight an increased future flood risk, future flood estimates are uncertain due to 1) the underestimation of rainfall in global climate models (GCMs) driving river routing models (Hirabayashi et al., 2013) due to the lack of explicit representation of storm dynamics in GCMs, and 2) the lack of a climate change effect incorporated into future flood hazard maps when a regionalized flood frequency analysis is performed (Wing et al., 2018). Furthermore, different global flood hazard estimates show large variability in flood hazard, exposed population, and economic loss estimates (Trigg et al., 2016).

Due to these limitations, recent work utilizes high-resolution, convection-permitting climate models that more accurately simulate the timing, structure, and intensity of precipitation on regional scales (Kendon et al., 2017, 2012; Prein et al., 2017b). Studies using convection-permitting models show that future convective storms (K. L. Rasmussen et al., 2017), mesoscale convective systems (Prein et al., 2017b, 2017c), and hurricanes (Gutmann et al., 2018) will intensify in the

future due to a warmer climate that has increased water-vapor holding capacity. These studies, along with others that show an increased intensity of precipitation extremes (Ban et al., 2015; Dai et al., 2017; Kendon et al., 2014; Prein et al., 2017a), suggest that flood risk will increase in a future climate. However, just because rainfall intensity increases in the future does not necessarily translate to more intense future floods, since floods are due to an interaction between the atmosphere, land-surface, and hydrology (Berghuijs et al., 2016; Davis, 2001). Therefore, the storms that explicitly produce flash floods over the CONUS have not previously been examined in a future, warmer climate.

The goal of this research is to understand future changes to rainfall and runoff associated with historical flash flood-producing storms using high-resolution convection-permitting climate models over the CONUS. While previous studies have used convection-permitting models to investigate future changes to individual flood-producing storms (Lackmann, 2013; Mahoney et al., 2018), the present research builds upon this prior work by examining future changes to nearly 600 flash flood-producing storms CONUS-wide. The focus of this study is from a storm-scale perspective, rather than changes to rainfall extremes, providing a novel view of how the characteristics in storms that produce high impact floods might change. Such an approach to understanding how rainfall characteristics and runoff may change in future flash flood-producing storms over the CONUS is necessary for quantifying future flood risk, which can be used to update crumbling water infrastructure and create more resilient communities in the face of climate change (Vano et al., 2019).

4.2 Data and Methods

4.2.1 *Convection-Permitting Simulations*

To examine how flash flood-producing storms might change in a future climate, high-resolution convection-permitting simulations of the current and future climate run by scientists at the National Center for Atmospheric Research (NCAR) are used. Liu et al. (2017) describes these simulations in detail, but we briefly summarize the major details. The simulations were run using the Weather Research and Forecasting (WRF) model V3.4.1 over a 1360 x 1016 grid point domain covering

the CONUS and portions of Canada and Mexico with a 4-km horizontal grid spacing (Figure 4.1). The model was configured with 51 vertical levels up to 50 hPa, with the highest resolution in the boundary layer. The parameterization schemes utilized in the model include the Thompson aerosol-aware microphysics (Thompson & Eidhammer, 2014), the Yonsei University (YSU) planetary boundary scheme (Hong et al., 2006), the rapid radiative transfer model (RRTMG) (Iacono et al., 2008), and the Noah-MP land-surface model (Niu et al., 2011), that was improved specifically for these simulations. Spectral nudging above the boundary layer was applied to geopotential height, horizontal winds, and temperature for horizontal scales greater than 2,000 km in order to avoid long-term climate drift (Feser et al., 2011) and to minimize deviations from the forcing data. Scales less than 2,000 km (i.e., local and mesoscale) were allowed to freely evolve, thus allowing for changes in the frequency and structure of sub-synoptic scale weather.

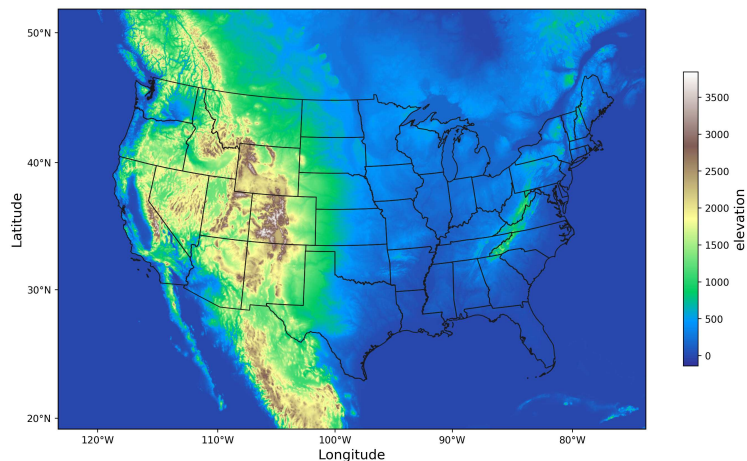


Figure 4.1: Elevation (m) over the domain of the 4-km convection-permitting simulations described by Liu et al. (2017) used in this study. While parts of Canada and Mexico are included in this domain, the present study focuses only on the continental United States.

To simulate the current and future climate, two sets of continuous simulations covering the time period from 2000–2013 were run using the WRF configuration previously described. First, a control (CTRL) simulation that reproduces the current climate over the CONUS was run, forced with ERA-Interim reanalysis data every 6 h. Second, a future climate was simulated over the same 13-year period using a “pseudo-global warming” (PGW) approach. This methodology has been

used in regional climate simulations all over the world (Ban et al., 2015; Dai et al., 2017; Gutmann et al., 2018; Liu et al., 2017; Prein et al., 2017b, 2017c, 2017a; K. L. Rasmussen et al., 2017; R. Rasmussen et al., 2014, 2011; Schär et al., 1996), including studies that examine how floods will change in a future warmer climate in the south-central U.S. (Lackmann, 2013) and Pacific Northwest (Mahoney et al., 2018). In the (Liu et al., 2017) simulations, the PGW approach was applied by adding a climate delta signal to the ERA-Interim data, as given by the following:

$$WRF_{input} = ERA - Interim + \Delta CMIP5_{RCP8.5} \quad (4.1)$$

where $\Delta CMIP5_{RCP8.5}$ is the climate delta signal, which is the 95-year multi-model ensemble-mean monthly change in CMIP5 under the RCP8.5 emission scenario between two 30-year periods:

$$\Delta CMIP5_{RCP8.5} = CMIP5_{2071-2100} - CMIP5_{1976-205} \quad (4.2)$$

The perturbed fields in the PGW simulations include horizontal wind, geopotential, temperature, specific humidity, sea surface temperature, soil temperature, sea level pressure, and sea ice. This results in a future warming over the CONUS of approximately +3–6° C and increase in water vapor mixing ratio of ~20–40%, consistent with Clausius-Clapeyron theory.

The Liu et al. (2017) simulations provide a useful framework for understanding how flood-producing storms might change in a future warmer climate over the CONUS. In the CTRL simulations, there is high fidelity in the depiction of precipitation characteristics, as Beck et al. (2019) found that these simulations outperform other gridded precipitation datasets, with more accurate precipitation totals over the mountainous west, where many flash floods occur (Saharia et al., 2017a). The CTRL simulations also performed best in terms of precipitation variability compared to other uncorrected datasets (Beck et al., 2019). In the PGW simulations, there is confidence that flash flood-producing storms are being reasonably well represented in the future, due to the use of nudging, which ensures that the synoptic environment is being reproduced in the future. Maddox

et al. (1980, 1979) showed that similar synoptic patterns are typically associated with flash floods over the CONUS, so a similar synoptic environment in the CTRL and PGW simulations provides confidence that flash floods in the current climate are present in the future. While there are numerous other factors that contribute to flash flooding in addition to precipitation, including changes in land cover/land use, soil moisture, and other land-surface characteristics, the present study focuses on changes in precipitation and the associated runoff in flash flood-producing storms since these factors are reasonably well simulated.

Furthermore, this PGW approach has been utilized to study specific historical floods in the future, including the south-central U.S. flood of May 2010 (Lackmann, 2013) and the November 2006 flooding from a land-falling atmospheric river event (Mahoney et al., 2018). These case studies demonstrate that the PGW approach is appropriate and well-suited to study how historical flood-producing storms and their ingredients will change in the future. The current study builds upon this prior work to show how nearly 600 flash flood-producing storms will change in a future warmer climate over the entire CONUS.

Caveats of the Liu et al. (2017) simulations are worth noting, given their inability to simulate all aspects of a future climate. Changes in land-use/land cover are not included in these simulations, despite these changes playing a role in future changes in runoff (Frans et al., 2013). Unlike some GCM projections, these simulations are unable to assess the uncertainty in climate change projections from multi-member ensembles due to the computational constraints in running high-resolution simulations (K. L. Rasmussen et al., 2017). Such a limitation was addressed in part by taking the 19-member ensemble mean of CMIP5 simulations, rather than using a single-model run as in R. Rasmussen et al. (2014, 2011). However, the Liu et al. (2017) simulations are still not able to simulate how the large-scale dynamics might change in a future climate, due to the spectral nudging employed. This large-scale dynamical change is more uncertain than the thermodynamic change in a future climate (Liu et al., 2017), thus the focus of the simulations is primarily on understanding how today's weather will change a future, warmer climate. A new set of simulations currently being run by NCAR will address this limitation by allowing the synoptic-scale to

freely evolve, which could lead to future work on how the frequency of flood-producing storms will change in a future climate. However, given the intent of the current set of simulations, this study only focuses on changes to flash flood-producing storm characteristics in a warmer moister climate over the CONUS.

4.2.2 *Flash flood cases*

The historical flash flood cases studied in a current and future climate are taken from the Chapter 2 flood-producing storm database over the CONUS from 2002–2013. This database identifies floods when a flood report from the National Center for Environmental Information (NCEI) is close spatially and temporally to a streamflow-indicated flood from the Shen et al. (2017) database. By utilizing the NCEI database, which groups flood events by causative meteorological feature, with the Shen et al. (2017) database, Chapter 2 captures meteorological systems associated with a hydrologic response. Furthermore, this database captures the rainfall characteristics of the flood events by utilizing the 4-km hourly Stage-IV precipitation dataset (Lin & Mitchell, 2005) to match observed rainfall over the entire duration of the flood event (plus a buffer of several hours). The centroid of the flood reports (computed by merging flood reports with county shapefiles and taking the geographic centroid for all report locations) for a particular event, $\pm 5^\circ$ latitude/longitude, was the spatial domain over which Stage-IV rainfall was analyzed. To isolate the likely flood-contributing rainfall, only the largest contiguous object with flood total rainfall accumulations exceeding the 75th percentile within this large ($\pm 5^\circ$) spatial domain was utilized.

While Chapter 2 identified 3436 flash flood-producing storms (including hybrid flood-producing storms with both flash and slow-rise flood characteristics) from 2002–2013 over the CONUS, only the top 25% most intense (by area-average rainfall) storms are used in this study. These flash floods exhibit a broad warm-season maximum from May to September (Figure 4.2), consistent with previous studies (Maddox et al., 1979; Schumacher & Johnson, 2006), and they occur throughout the year due to the variety of systems leading to flash floods across the country (Chapter 2). The dates and locations of these 859 flash flood-producing storms from the Chap-

ter 2 database are utilized to collect hourly CTRL and PGW precipitation data, again only using the largest contiguous object with flood total accumulations exceeding the 75th percentile. This 75th percentile was computed separately for CTRL and PGW simulations to take into account that the amount (mm) of rain corresponding to the 75th percentile likely changes in the future. The calculation of the 75th percentile occurs after accumulating precipitation over the entire flood duration, so it is not explicitly all wet-hours or all-hours (including dry), due to some flood-producing storms raining continuously, and others experiencing brief pauses in rain (not shown). Ban et al. (2015) and Schär et al. (2016) pointed out that using only all wet-hours can inflate future changes in extreme precipitation due to decreased frequency of future wet-hours, so the use of all-hours is preferred. However, given the goal to understand how flood-producing storms change over their entire lifetime in a future climate, it does not meet the needs of the present study to explicitly use all-hours; otherwise, the focus is no longer on the flood-producing storm. This is an important caveat of the study.

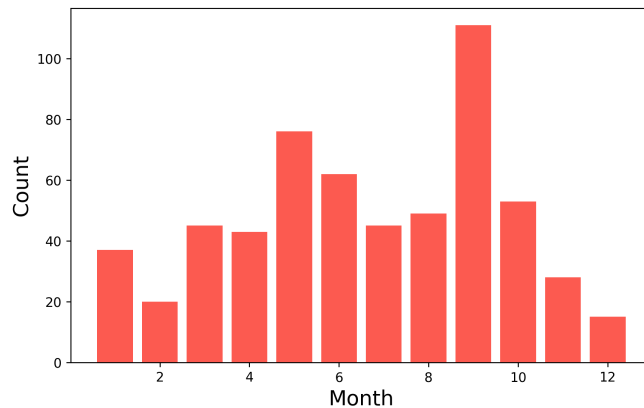


Figure 4.2: Seasonality of the most intense flash flood-producing storms in the continental United States from 2002–2013.

Other caveats in the framework of the present study are that by calculating the contiguous rainfall object separately in the CTRL and PGW simulations, a shift of this heavy-rainfall region within the larger $\pm 5^\circ$ domain is allowed in the PGW simulations. However, the duration is constrained to

be the same as the observed flood in the CTRL and PGW simulations, which is a possible limitation of the study. Given the use of nudging and the minor differences between Stage-IV, CTRL, and PGW flood durations (Figure 4.3, Table 4.1), which is computed by summing all hours during which precipitation fell, accounting for different flood durations does not seem necessary. However, this would be an avenue for future work if changes in frequency of flood-producing storms were explored.

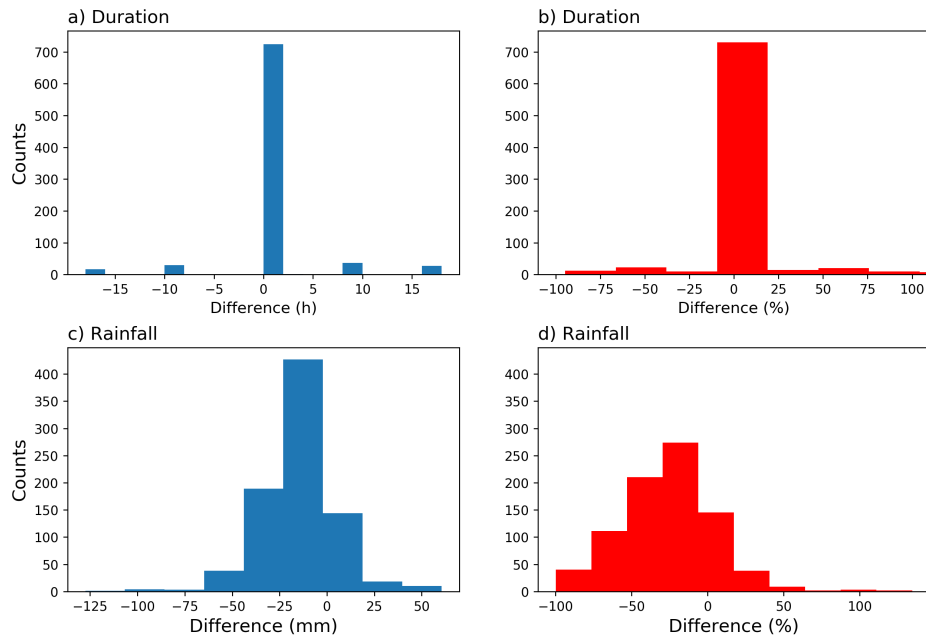


Figure 4.3: Histogram of differences between simulated (CTRL) and observed (Stage-IV) rainfall a) duration (h), b) duration (%), c) area-averaged rainfall (mm), and d) area-averaged rainfall (%) in the top 25% most intense flash flood-producing storm over the U.S. The left column (a and c; blue coloring) shows the absolute difference, while the right column (b and d; red coloring) shows the percent difference. A positive difference indicates that CTRL data overestimates flash flood duration or rainfall.

4.2.3 Comparison of observed and simulated flood rainfall

To ensure that the CTRL and PGW simulations compared well with the observations, CTRL and PGW flash flood rainfall was compared to that observed by Stage-IV. Both the simulations and Stage-IV data have a 4-km horizontal resolution and hourly temporal resolution, so a direct comparison can be made. Fig. 3a and b shows that flash flood duration is similar between CTRL

Table 4.1: Mean values of flash flood area-averaged rainfall, maximum hourly rain rate, duration, area, and runoff in a current (CTRL) and future (PGW) climate, the difference (PGW-CTRL), percent change (% change), and percent change per degree of warming (% K⁻¹) in a future climate. Values in the parentheses indicate the 95% confidence interval (CI) of the mean values for % change and % K⁻¹ after bootstrapping.

	CTRL	PGW	PGW-CTRL	% change (95% CI)	% K ⁻¹ (95% CI)
Area-avg rain (mm)	54.7	66.3	11.6	20.9 (18.7–23.1)	8.2 (5.1–11.6)
Max rain rate (mm h ⁻¹)	86.8	105.6	18.9	27.1 (24.0–30.2)	10.5 (7.6–14.0)
Area (km ²)	1.18*10 ⁵	1.75*10 ⁵	-6122	-0.94 (-3.5–1.9)	2.6 (-0.77–7.1)
Runoff (mm)	4.5	6.4	1.5	48.9 (34.8–66.0)	15.3 (8.2–23.0)

and Stage-IV data, except for a few cases that have a ± 10 –15 h difference. Accumulated rainfall shows a larger difference between CTRL and Stage-IV (Figure 4.3c, d), as might be expected, with a general underestimation (negative values) of area-averaged accumulated rainfall in CTRL compared to Stage-IV. To more directly quantify these differences in CTRL and Stage-IV, duration (D) was multiplied by area-averaged rainfall (R) for each flash flood-producing storm in the CTRL and Stage-IV data and compared. For each storm, the squared difference between the CTRL and Stage-IV $R \times D$ was computed. A mean-squared error (MSE) was then computed for all flash flood-producing storms and was a threshold for excluding particular flood cases. Any storm where the squared $R \times D$ difference exceeded the MSE for the entire sample was excluded from analysis, as well as if the area-averaged rainfall difference exceeded 50%. Such a statistical approach was employed in order to objectively omit poorly represented floods in either the simulations or observations, resulting in 584 flash flood-producing storms.

Visual comparisons between Stage-IV, CTRL, and PGW precipitation for select floods were also conducted in order to confirm these objective criteria as reasonable. As an example of a poor comparison between observations and simulations, Figure 4.4 shows the accumulated rainfall for a flash flood in the south-central U.S. that occurred from 07 UTC 01 May–21 UTC 02 May 2011. The area-averaged rainfall difference between Stage-IV and CTRL is -66%, with a large area of accumulated rainfall exceeding 180 mm in the northeast corner of the flood domain in Stage-IV but not in the CTRL (Figure 4.4a, c). This area of heavy rainfall in Stage-IV (Figure 4.4a) aligns with the River Forecast Center (RFC) boundaries and is actually a spurious artifact in the

observations. Such an error in Stage-IV precipitation, with discontinuities across RFC boundaries is well-known, as has been documented by Nelson et al. (2016). This flood was thus excluded based on the objective criteria discussed above, not for issues with the CTRL precipitation, but with the Stage-IV precipitation. The CTRL and PGW accumulated rainfall for this flood compare remarkably well to each other in terms of structure, location, and rainfall amount, and reproduce the quasi-linear band of precipitation observed in middle of the domain by Stage-IV when the artifact is removed (Figure 4.4b).

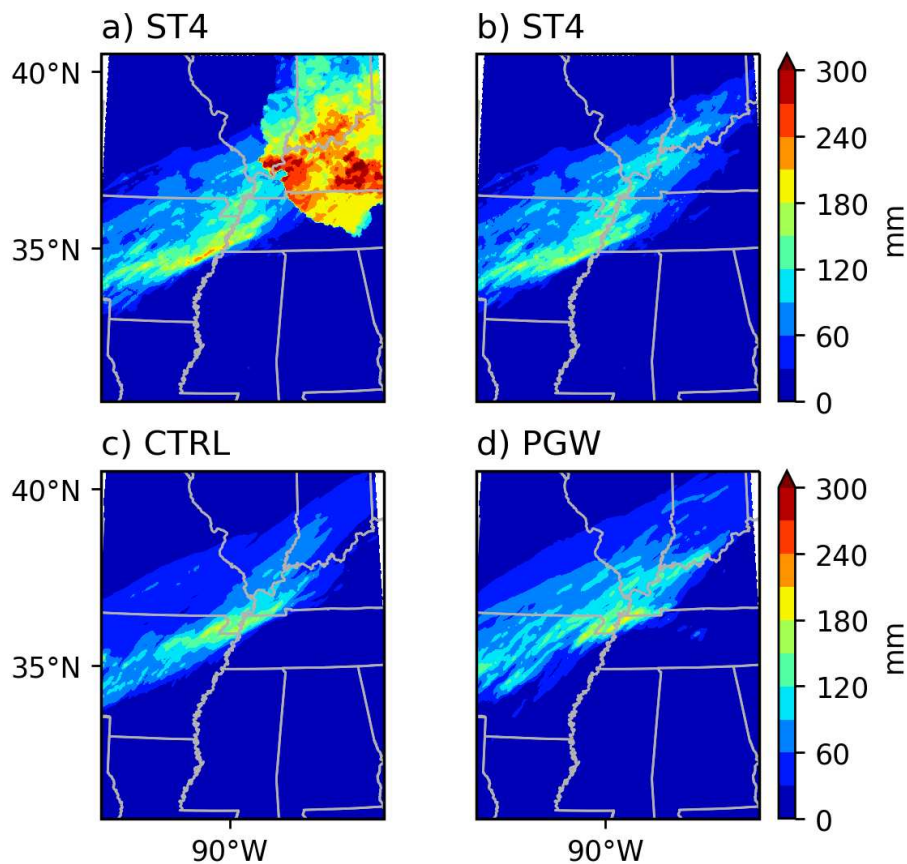


Figure 4.4: Total accumulated rainfall (mm) for a flash flood-producing storm in the south-central U.S. that occurred from 07 UTC 01 May–21 UTC 02 May 2011, in a) the full Stage-IV data, b) Stage-IV without the erroneous rainfall data, c) CTRL, and d) PGW simulations. In a), the erroneous rainfall data in the northeast part of the domain aligns with a river forecast boundary line (not shown).

In order to further ensure that the accumulated rainfall structure is similar between Stage-IV observations and simulations, a metric was computed for each flash flood that quantifies the

structural similarity in rainfall. This metric is a structural similarity index (SSIM), and is given by the following equation from Wang et al. (2004):

$$SSIM(x, y) = \frac{(2\mu_x\mu_y + c_1)(2\sigma_{xy} + c_2)}{(\mu_x^2 + \mu_y^2 + c_1)(\sigma_x^2 + \sigma_y^2 + c_2)} \quad (4.3)$$

where x, y is the pixel location, μ is the mean pixel intensity, σ is the variance of intensity, and c_1 and c_2 are constants to avoid instability when the other terms in the denominator are close to zero. While the SSIM is used in the image processing community to compare the luminance, contrast, and structural differences between two images, it is utilized in this study to compare differences in flash flood rainfall accumulation. In this study, the SSIM computes the structural and intensity differences in each flash flood's accumulated rainfall between Stage-IV observations and CTRL simulations, as well as CTRL and PGW simulations. Thus, the SSIM is a quantitative method to ensure that similar flood-producing rainfall is reproduced in the CTRL and PGW simulations.

When computed for all 584 flash floods, the mean SSIM between Stage-IV and CTRL flash flood accumulated rainfall is 0.88 (Figure 4.5). A value closer to 1 indicates exact structural similarity, so a value of 0.88 indicates high structural similarity between Stage-IV and CTRL rainfall, with the bulk of the distribution between 0.8 and 0.95. Exact agreement (SSIM=1) between Stage-IV observations and CTRL simulations is not anticipated, due to aforementioned issues with Stage-IV observations, as well as slight differences in CTRL representations of rainfall. However, these high SSIM values between Stage-IV and CTRL flash flood accumulated rainfall indicate that the simulations are reproducing observed flash flood rainfall in both amount and structure quite well.

CTRL and PGW SSIM flash flood accumulated rainfall also exhibits high values, with a mean of 0.89 and most floods showing a SSIM from 0.8–0.95. Even for the flash flood with the lowest SSIM of 0.66 between CTRL and PGW, the flash flood accumulated rainfall shows that the structure and location of rainfall is still remarkably similar for a case in southern Texas (Figure 4.6). Rainfall accumulations are slightly higher in the PGW flash flood as one might expect due to the

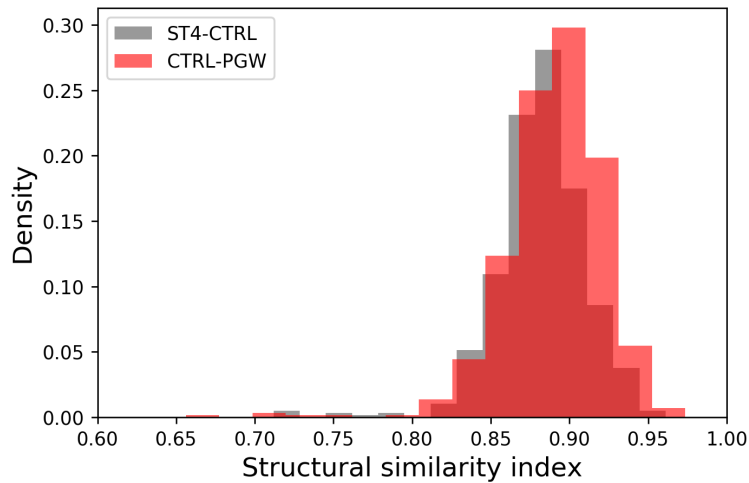


Figure 4.5: Probability density function of the structural similarity index (Wang et al., 2004) between Stage-IV and CTRL (grey) and CTRL and PGW (red) flash flood accumulated rainfall in 584 flash flood-producing storms over the continental U.S. A value closer to 1 indicates greater similarity.

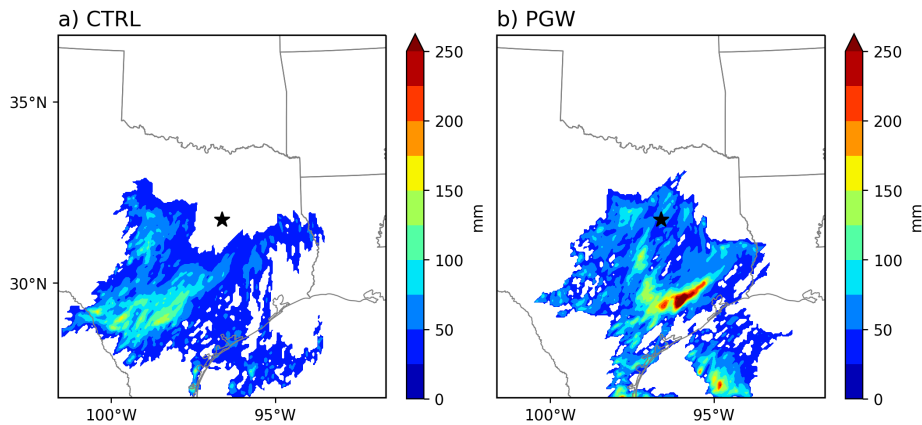


Figure 4.6: Flash flood accumulated rainfall in a) CTRL simulations and b) PGW simulations for a flood that occurred in eastern Texas, with the flood centroid shown by the black star. This flash flood had the lowest structural similarity index of all flash floods between the CTRL and PGW simulations of 0.66.

warmer and moister conditions in the PGW simulations. Thus, a perfect agreement (SSIM=1) between CTRL and PGW simulations is not expected, due to the different thermodynamic environment in the PGW simulations, but the high SSIM values indicate that the structure and spatial pattern of the accumulated rainfall is similar over the same location and duration in the PGW flash floods as the CTRL. Therefore, these results provide additional confidence that a similar flash

flood-producing storm is occurring in the future, just in a warmer and moister environment, which may or may not result in a flood, but still a heavy rainfall event.

4.2.4 *CTRL and PGW synoptic conditions in the Arkansas flash flood of 2008*

To demonstrate the ability of the PGW simulations to reproduce an observed flash flood aside from the SSIM, a case study is explored. Specifically, the Arkansas flash flood of 2008 that occurred from 02–16 UTC 18 March is examined, which was part of the larger Midwest floods in early spring 2008. These floods were due to a closed upper-level low that slowly progressed eastward across the central CONUS that helped to transport moist air from the south in the Gulf of Mexico. A stalled frontal boundary across northern Arkansas and southern Illinois resulted in repeated bouts of heavy rainfall and thunderstorms as several low-pressure systems moved along this boundary (NWS St. Louis, MO, 2019). In Arkansas, this resulted in one death and \$450 K in damage, mainly to roads and bridges (NOAA, 2019).

CTRL simulations show a southwest-to-northeast oriented band of rainfall accumulation associated with this flood, with a maximum rainfall accumulation of 167 mm (Figure 4.7). The PGW simulations reproduce this band of heavy rainfall, with a similar location and structure (SSIM=0.90), except with higher local rainfall amounts over 250 mm in eastern Oklahoma and northwest Arkansas. A similar location and structure of the flash flood rainfall is likely due to similar synoptic conditions in the PGW simulations as the CTRL simulations, as a result of the spectral nudging (see Section 4.2.1). This is clearly shown in the 500 hPa height and winds prior to the flood start at 00 UTC 03 March 2008 (Figure 4.8). Both the CTRL and PGW 500 mb maps at this time show an upper level trough with a closed low south of Arizona and New Mexico, and downstream ridging over the eastern CONUS, which directed southwesterly flow into Arkansas (Figure 4.8a, b). Mean sea-level pressure and winds are also similar in the CTRL and PGW simulations at 00 UTC 03 March 2008 (Figure 4.8c, d), with a surface low pressure over southern Texas and a broad high pressure over the eastern CONUS allowing for southerly winds to transport moist air from the Gulf of Mexico into Arkansas. The only major difference in the synoptic environ-

ment between the CTRL and PGW simulations for the Arkansas flash flood of 2008 is enhanced moisture in the PGW simulations, with precipitable water values reaching up to 60 mm, compared to a maximum of 50 mm in the CTRL simulations, which is consistent with expected future increases in moisture in this region (K. L. Rasmussen et al., 2017). The similarity in the CTRL and PGW synoptic environment for the Arkansas flash flood of 2008, except for more moisture in the PGW simulations, is representative of the main changes (or lack thereof) for the 584 flash floods being analyzed in this study. Given that flash floods are well known to occur under similar synoptic conditions and with similar ingredients (Doswell et al., 1996; Maddox et al., 1980, 1979), the PGW approach provides an opportunity to examine the same historical flash flood-producing storms, including similar synoptic environments, in the future, except with warmer and moister conditions.

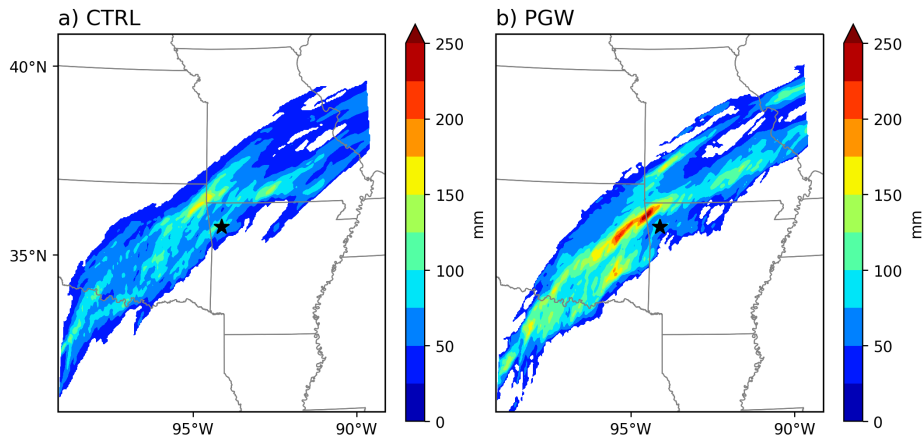


Figure 4.7: Flash flood accumulated rainfall from 02–16 UTC 03 March 2008 in a) CTRL simulations and b) PGW simulations for the Arkansas floods of 2008.

4.2.5 *Flash flood storm calculations*

The calculation of flash flood-producing storm rainfall characteristics (frequency, area, duration, rain accumulation, rain rates) are all computed separately for CTRL and PGW simulations within the heavy rainfall object (i.e., the largest contiguous area of accumulated rainfall exceeding the 75th percentile). The frequency of flash flood-producing storms over the CONUS is calculated

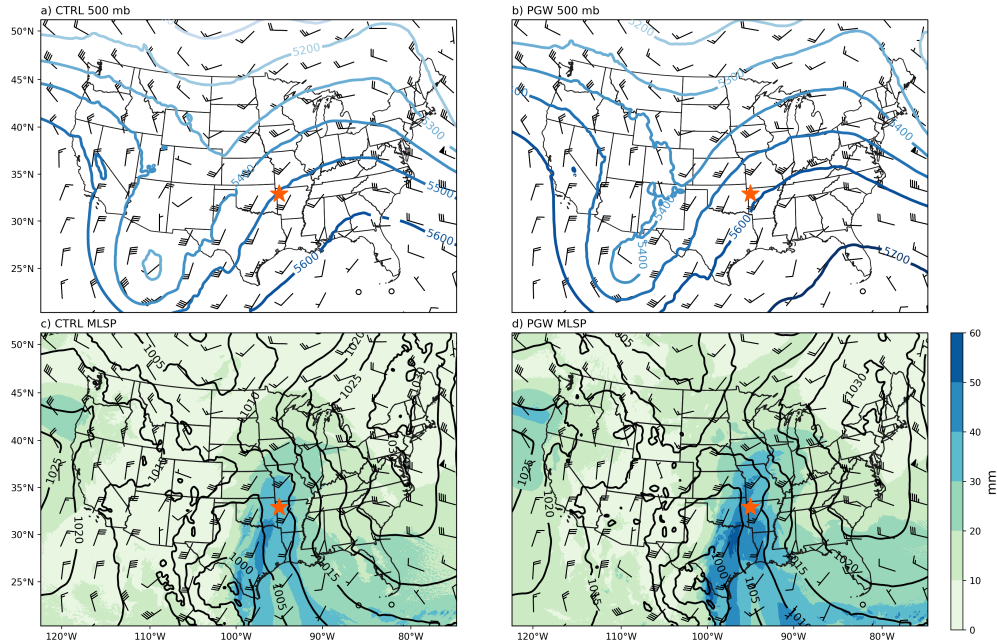


Figure 4.8: 500 hPa geopotential height (blue contours; m) and winds (barbs; each half barb=5 kts, full barb=10 kts, and flags=50 kts) for a) CTRL simulations and b) PGW simulations, as well as mean sea-level pressure (black contours), 10 meter winds (barbs), and precipitable water (mm; shading) in c) CTRL simulations and d) PGW simulations at 00 UTC 03 March 2008. The orange star indicates the flood centroid of the Arkansas floods of 2008.

by summing the occurrence of rainfall for all floods at a particular grid point. If flash flood rainfall only occurs at one grid point, then that grid point will have a frequency of one, but if three flash floods have rainfall at a grid point, then the frequency is three, and so on. Flash flood area is computed by summing the number of raining pixels within the largest contiguous area of accumulated rainfall exceeding the 75th percentile and multiplying by the grid-spacing (4 x 4 km). Duration is calculated by summing the number of hours over which rainfall occurred within a flood report. Rain accumulation is the sum of rainfall over the entire duration of a flood and is either expressed as area-averaged rainfall or the rainfall per storm, with the latter being the total rainfall accumulation from all storms at a grid point divided by the flood-producing storm frequency at that same grid point. The maximum rain rate is the maximum rainfall per hour (mm h^{-1}) that occurred at any point in time during the flood-producing storm. When calculating the percent change per Kelvin ($\% \text{K}^{-1}$) of these quantities, percent differences between the CTRL and PGW quantities were taken, and divided by the degree of future warming per storm, rather than using the average

change in the warming to get a more accurate representation of changes within individual floods. Note that values in Table 4.1 and Figure 4.12–Figure 4.15 are only calculated for a subset of the entire sample where the difference between Stage-IV observed and CTRL simulated area-average rainfall is less than 25%. This results in 354 out of the 584 flash flood-producing storms and is utilized to provide more confidence in the statistics computed.

In addition to calculating flash flood-producing storm rainfall quantities, the runoff associated with each storm was calculated, due to the role of runoff in generating floods (Davis, 2001). Here, hourly surface plus subsurface runoff output from the Noah MP land surface model at each grid point is utilized, as in R. Rasmussen et al. (2014), over the whole duration of the flood-producing storm. The subsurface runoff was corrected to be the residual of all water balance terms (precipitation, evapotranspiration, surface runoff, snow water equivalent, soil moisture, and canopy water), due to Noah MP not computing it correctly (Personal communication, Kyoko Ikeda). Unlike the flash flood-producing storm rainfall, runoff over the entire domain ($\pm 5^\circ$) was analyzed, due to flash flood rainfall leading to complex downstream responses in runoff that depend on watershed configuration, land-use, and topography (Davis, 2001).

While using a temporal and/or spatial lag to analyze runoff is preferred in some hydrologic studies, the focus of this study is on the flash flood-producing storm, so the immediate hydrologic response to the intense rainfall produced by these storms is of interest. Therefore, the focus is on the immediate storm-generated runoff. Given the short temporal nature of flash flood-producing storms, the addition of other water balance terms in addition to runoff is not included in this study since computing the water balance requires longer time-frames (months to years; Padrón et al., 2017) and the full scope of wet and dry periods, which does not apply to flash flood-producing storms. The runoff examined in this study is thus utilized as a proxy for understanding the hydrologic response to intense flash flood-producing storm rainfall.

4.3 Results

Flash flood-producing storms in the future show a similar location and frequency over the CONUS as flash flood-producing storms in the current climate (Figure 4.9). Not only does this ensure that the PGW simulations are capturing a similar occurrence of flash flood-producing storms as the CTRL simulations, but the spatial distribution also compares well to that observed by Stage-IV in the flood-producing storm climatology from Chapter 2. The similar spatial distribution of flash flood-producing storms in the PGW simulations is expected based on the use of spectral nudging and the PGW method (see Section 4.2a–d), that reproduces historical events in a future climate. A noticeable change in the location of flash flood-producing storms is not expected based on this methodology, which does not incorporate large-scale synoptic changes in a future, warmer climate. While this is a limitation of the present study, results in Figure 4.9 demonstrate that a similar location and distribution of flash flood-producing storms occur in the CTRL and PGW simulations, which might or might not change significantly in a future climate if changes in synoptic patterns were represented in this study.

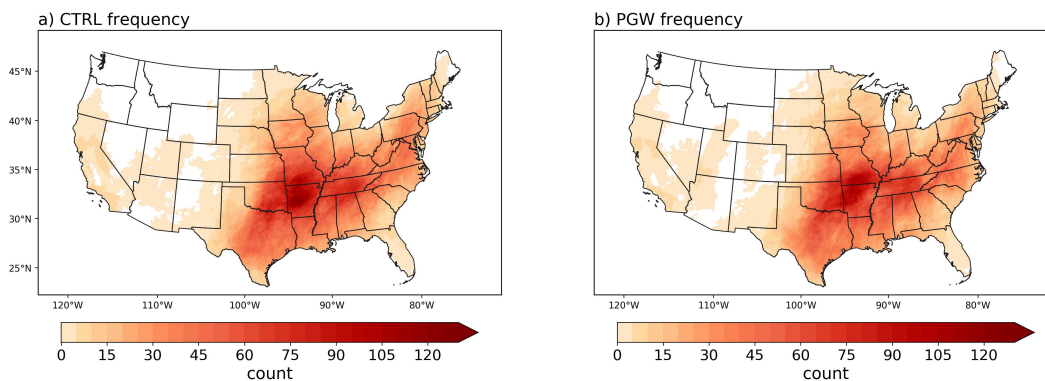


Figure 4.9: Occurrence of flash flood-producing storms in the a) CTRL simulations and b) PGW simulations, where darker colors indicate a higher occurrence of flash flood rainfall. Areas without shading do not indicate a lack of flash flood-producing storms in that region, but rather that the top 25% of flash flood-producing storms do not occur in that region. Note that the distribution of storms is similar in the CTRL and PGW simulations.

Accumulated rainfall in flash flood-producing storms increases over most of the CONUS in the future, with an average increase of 20.9% and the 95% confidence interval (CI) after bootstrapping

ranging from 18.7–23.1% (Table 4.1). Increases are notable in the lower Mississippi Valley and Mid-Atlantic, where rainfall increases over 50 mm per storm (Figure 4.10). Both regions are impacted by floods from land-falling tropical cyclones (Ashley & Ashley, 2008b; Saharia et al., 2017a; Schumacher & Johnson, 2006; B. K. Smith & Smith, 2015), so future increases in tropical cyclone rain rates (Gutmann et al., 2018) could explain some of the signal of increased rainfall. Additionally, the lower Mississippi basin and surrounding Midwest region receive frequent flash floods due to MCSs (Ashley & Ashley, 2008b; Kunkel et al., 2012; Schumacher & Johnson, 2006). Prein et al. (2017c) showed that MCS frequency and precipitation rates increase over the CONUS in a future climate, thus providing another source of increased future flash flood rainfall in this region. More localized increases in future flash flood-producing rainfall occur in the Southwest and suggest a stronger Southwest monsoon, since this is the primary flash flood-producing storm mechanism in this region (Ashley & Ashley, 2008b; Saharia et al., 2017b).

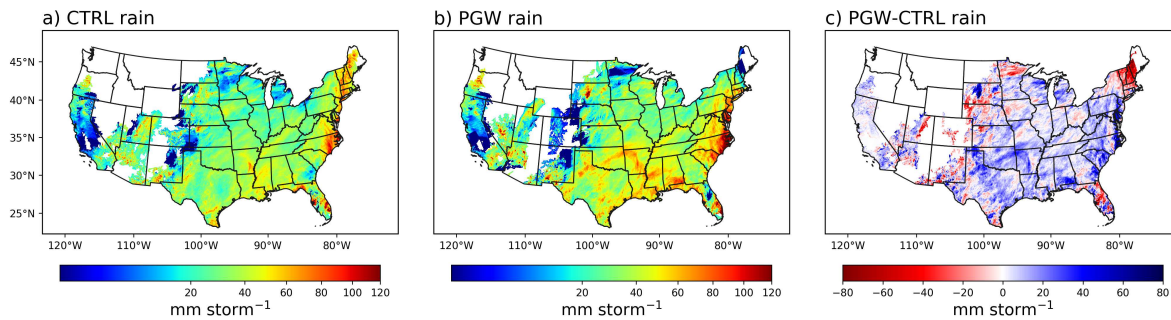


Figure 4.10: Amount of rainfall per flash flood-producing storm (mm storm^{-1}) for 584 storms in a) CTRL simulations, b) PGW simulations, and c) the PGW-CTRL difference where blue (red) represents an increase (decreases) in future rainfall per storm.

Given that flash floods are primarily driven by convective systems (Davis, 2001; Maddox et al., 1979), increased rainfall in future flash flood-producing storms could be linked to the increased frequency of strong convection in a future, warmer climate due to increased moisture, convective available potential energy (CAPE), and convective inhibition (CIN) over the CONUS (Chen et al., 2020; K. L. Rasmussen et al., 2017). This was examined in two flash flood-producing storms—one that had a 49% decrease in future rainfall, and another that had a 99% increase in future rainfall (not

shown). In both storms, CAPE and CIN increased in the future, but CAPE (CIN) increased more (less) in the flash flood that had increased future rainfall, whereas CIN increased more in the flash flood that had decreased future rainfall. Due to the nearly CONUS-wide increases in future rainfall (Figure 4.10), this suggests that future increases in CAPE exceed increases in CIN, supporting stronger flash flood-producing storms in a future climate. Decreased rainfall in future flash flood-producing storms in Figure 4.10 could be due to future increases in CIN suppressing some of the weaker storms, or it could be due to a slight shift in location of the flash flood-producing rainfall (see Section 4.2.2).

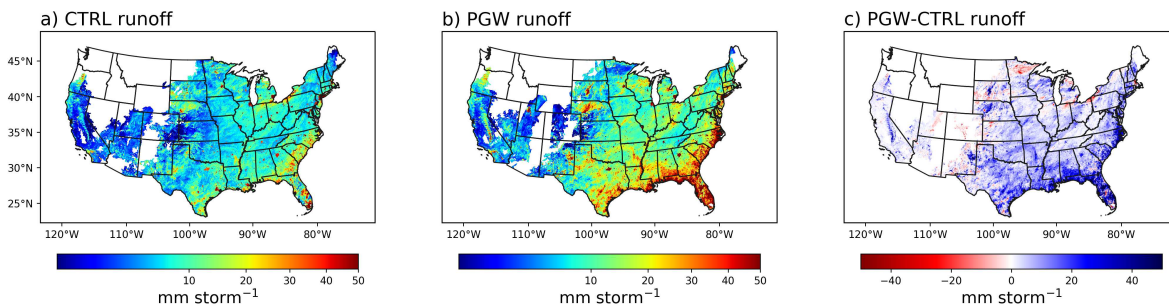


Figure 4.11: As in Figure 4.10 , but for flash flood runoff (mm storm^{-1}).

Despite localized areas of decreased future flash flood rainfall, flash flood runoff increases nearly everywhere over the CONUS (Figure 4.11). On average, runoff increases by 48.9% in the future, with the 95% CI between 34.8–66.0% (Table 4.1). Increases in future runoff are particularly noticeable along the coasts and lower Mississippi Valley, with increases over 30 mm per storm. Such large increases in runoff could be due to increased precipitation excess in a future climate, whereby rainfall exceeds soil moisture storage capacity. Additionally, changes in future seasonal evapotranspiration and soil moisture could influence future changes in storm-generated runoff, but a hydrologic model is needed in order to accurately quantify these changes. Thus, it can only be said with some confidence that increased precipitation excess due to more accumulated flash flood rainfall might contribute to increased future storm-generated runoff.

In addition to contributions from increased future rainfall, future increased runoff could be due to more precipitation falling as rain rather than snow in a warmer climate (R. Rasmussen et al., 2014), which would impact northern and mountainous regions of the CONUS where snowpack is substantial (Berghuijs et al., 2016). Musselman et al. (2018) specifically examined future changes to rain-on-snow flood risk over western North America and found that this risk increases 20–200% mainly due to increases in rainfall rather than snowmelt, particularly over the Sierra Nevada, Canadian Rocky, and Colorado Rocky Mountains. Such results are consistent with increased runoff over the Sierra Nevada Mountains (Figure 4.11) but does not explain changes in the rest of the mountainous West, due to a limited sample size. It is likely that the rain-on-snow events studied by Musselman et al. (2018) are categorized as slow-rise floods, as found in Chapter 2, whereas the few flash floods in the mountainous West in this study are likely a result of upslope convection (Ashley & Ashley, 2008b) and the Southwest monsoon (Ashley & Ashley, 2008b; Saharia et al., 2017b). Thus, the main explanation for increased runoff in a future climate over the CONUS is likely associated with precipitation excess from future increases in flash flood rainfall, despite slight shifts in rainfall location. It is possible other land-surface and hydrologic components contribute to this change as well, depending on soil-type, soil moisture, and topography. This result provides additional evidence that not only are the simulations able to capture flash floods in a future climate (floods are by definition, due to runoff), but suggests that these flash floods might become more intense in the future due to increases in both rainfall and runoff over most of the CONUS.

Regionally, there are variations in how future increases in rainfall from flash flood-producing storms translates to changes in runoff. The eastern CONUS (east of -87°W , which is roughly east of Illinois) experiences a median future rainfall increase of 17.5% and median future runoff increase of 17.6%, with a narrow 95% CI after bootstrapping, as shown by the narrow notches (Figure 4.12). These median changes in future flash flood rainfall and runoff are fairly similar, but future runoff changes show a greater range from approximately -45% to 60% (i.e., the whiskers in Fig. 12), while future rainfall changes have a narrower range from approximately -15% to 55%. The central CONUS (-103° to -87°W , which is roughly from Texas to Illinois), has a median future rainfall

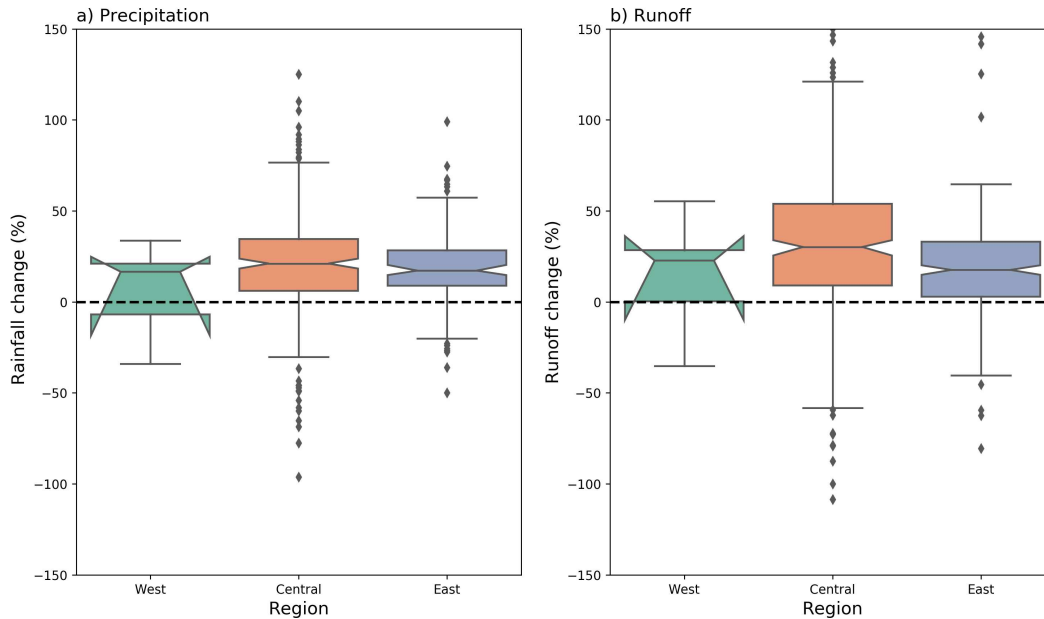


Figure 4.12: The percent future change in a) area-averaged flash flood rainfall and b) runoff, separated by region. West is west of -103°W (or west of Texas), Central is from -103° to -87°W (roughly from Texas to Illinois), and East is east of -87°W (roughly east of Illinois). Boxes show the interquartile range (IQR; first (Q1) through third (Q3) quartile, or 25th–75th percentile), whiskers denote the “minimum” ($Q1 - 1.5 \cdot \text{IQR}$) and “maximum” ($Q3 + 1.5 \cdot \text{IQR}$), and diamonds indicate outliers. Notched lines in the middle of the box indicate the median value, with the size of the notches showing the 95% confidence interval. A positive percent change (i.e., above the dashed horizontal line at zero) indicates a future increase in rainfall or runoff.

increase of 20.5%, with the median future runoff change of 30% exceeding this rainfall change. While these values are robust as shown by the narrow CI, the range of both rainfall and runoff are large in the central CONUS, spanning from -40% to 75% and -60% to 125%, respectively. The western CONUS (west of -103°W , or west of Texas) has the lowest future rainfall increase, with a median of 16.6%. However, as shown by the inverted notch, which is due to having too few samples ($n=10$), this median value is anywhere between -5 to 20%. Runoff changes in the western CONUS similarly display an inverted notch, with a median increase of 22.7% and the 95% CI ranging from 0 to 30%. Despite differing uncertainties and ranges among the different regions, all regions show a positive skew in future flash flood rainfall and runoff changes, suggesting that flash floods in all regions of the CONUS might intensify in a future climate. However, the degree to which they intensify and the mechanisms causing these changes is unexplored and remains an avenue for future work.

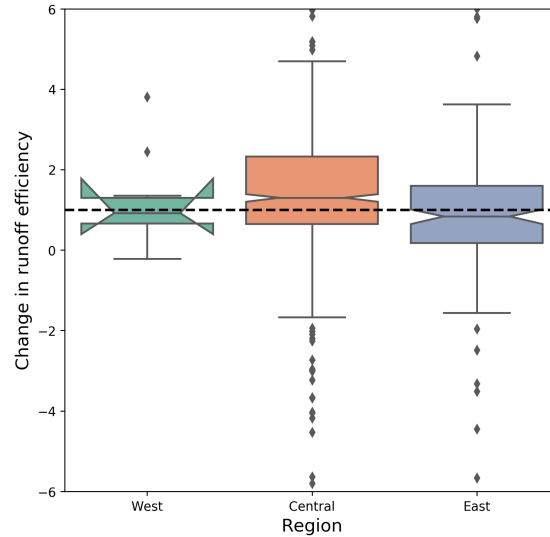


Figure 4.13: As in Figure 4.12, except for the change in runoff efficiency (runoff/precipitation), where values above the dashed line at 1 indicate a future increase in runoff efficiency (increases in runoff exceed increases in precipitation), values between 0 and 1 indicate a future decrease in runoff efficiency (increases in precipitation exceed increases in runoff), and values below 0 indicate a decrease in either future runoff or precipitation .

The future change in the efficiency of runoff generation in each region is shown in Figure 4.13 by dividing the future change in runoff (Figure 4.12b) by the future change in precipitation (Figure 4.12a). Values above 1 indicate an increase in storm-generated runoff efficiency, values between 0 and 1 indicate a decrease in runoff efficiency (i.e., precipitation increases exceed runoff), and values below 0 indicate a future decrease in either runoff or precipitation. The western and eastern CONUS display a median runoff efficiency of 0.92 and 0.82, respectively, indicating runoff is less efficient in a future climate. Runoff efficiency ranges from -0.5 to 1.5 in the western CONUS, while in the eastern CONUS, values range from approximately -2 to 4. The central CONUS, in contrast, shows a median future runoff efficiency of 1.23, indicating that the future increase in runoff exceeds the future increase in precipitation. However, all regions display average runoff values above 1, consistent with Table 4.1 and Figure 4.10–Figure 4.11, where the future increase in runoff exceeds the future increase in precipitation in flash flood-producing storms. Such results are in contrast to previous studies that show decreases in runoff efficiency with temperature (Nowak et al., 2012; Woodhouse & Pederson, 2018), but as suggested by Lehner et al. (2017), temperature

is a secondary influence on runoff efficiency and precipitation is the first, the latter of which likely explains most of the change in flash flood runoff efficiency in a future climate. Other mechanisms responsible for future increases in flash flood storm-generated runoff exceeding precipitation could be due to variations in soil type, topography, and soil moisture, which are beyond the scope of the study to explore but could be examined using a hydrologic model.

More intense future flash floods in the CONUS are also observed through changes in the maximum hourly flash flood rain rates (Figure 4.14). The entire distribution of maximum hourly rain rates shifts to more intense rain rates from the CTRL to PGW simulations, suggesting that rain rates producing flash floods may intensify in the future. The maximum hourly rain rates increase on average by 27.1%, with a 95% CI ranging from 24.0–30.2% (Table 4.1). When maximum rain rates are scaled per degree of warming, they display a positive skew (Figure 4.14b), indicating that the majority of maximum rain rates in flash flood-producing storms increases per degree of warming in a future climate. On average, this increase is 10.5% K⁻¹, with the 95% CI between 7.6–14.0% (Table 4.1). However, the median increase is 7.5% K⁻¹, which is closer to the increase in future rain rates predicted by Clausius-Clapeyron theory and future projections of hourly precipitation extremes (defined as the 95% to 99.99%) over the United Kingdom (Kendon et al., 2014), European Alps (Ban et al., 2015), and CONUS (Prein et al., 2017a). Note that unlike Ban et al. (2015), however, the present study examines the future change in maximum hourly rain rates during the entire duration of flash flood-producing storms, rather than using strictly all-hours (Ban et al., 2015). Therefore, caution must be used when comparing the % K⁻¹ in maximum hourly rain rates in this study against others, especially those who consider changes in extreme percentiles of hourly precipitation (Ban et al., 2015; Kendon et al., 2014; Prein et al., 2017a)..

While the median future change in maximum hourly rain rates in flash flood-producing storms is consistent with Clausius-Clapeyron theory and previous work, the average 10.5% K⁻¹ increase in maximum hourly rain rates exceeds that predicted by Clausius-Clapeyron theory. Such a result could be due to the dynamics operating in more intense cases of convective flash flood-producing storms that provide additional latent heat release to intensify rain rates beyond Clausius-Clapeyron

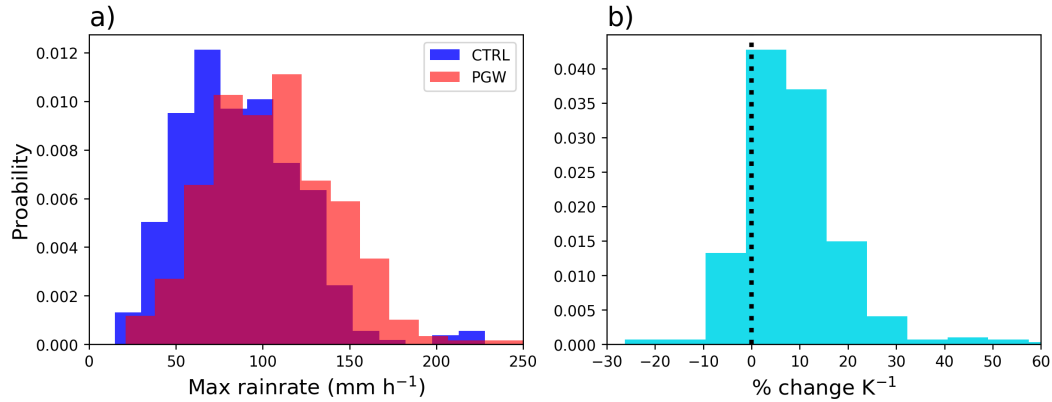


Figure 4.14: Probability distribution function of a) maximum hourly rain rates (mm h^{-1}) in CTRL (blue) and PGW (red) flash flood-producing storms, b) the percent change per Kelvin ($\% \text{ change K}^{-1}$) in maximum hourly rain rates of PGW flash-flood producing storms compared to CTRL. The dotted line is located at 0 to distinguish between the future percent increase and decrease per Kelvin.

theory (Trenberth, 1999; Trenberth et al., 2003). This hypothesis is supported by findings from Tan et al. (2015), who found that historical increases in tropical precipitation were due to changes in the frequency of deep organized convection likely associated with changes in dynamics. A more detailed investigation of how storm dynamics modulate future changes in flash flood-producing storm rainfall in a warmer future climate will follow this study in order to better understand this process.

Other changes in flash flood-producing storm characteristics examined include the area of the precipitating system. The total storm area decreases slightly, by -0.94% on average in a future climate (Table 4.1; Figure 4.15), though when scaled by temperature, there is minimal increase of $2.6\% \text{ K}^{-1}$, on average (Figure 4.15b). This discrepancy between the slight percent decrease in area and increase when scaled by temperature is due to each quantity being calculated for individually for each storm, then the mean being taken. That is, for each storm, the percent difference in area is calculated and the mean is taken (values in Table 4.1), while the percent change per degree of warming is computed as the percent difference in area divided by the domain average temperature change for each storm.

While temperature increases in almost all future flash flood-producing storms (Figure 4.16) a few storms experience a temperature decrease in the future, as well as a decrease in area, leading to

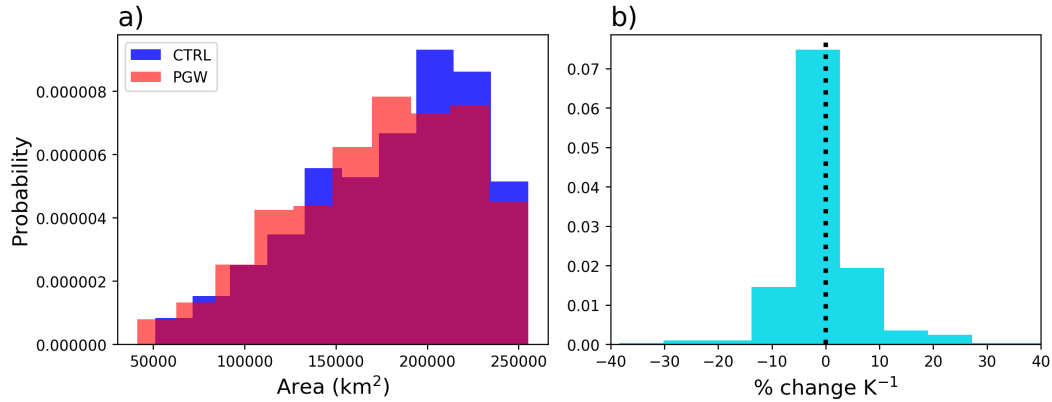


Figure 4.15: As in Figure 4.14, except for the area (km²) of flash flood-producing storms.

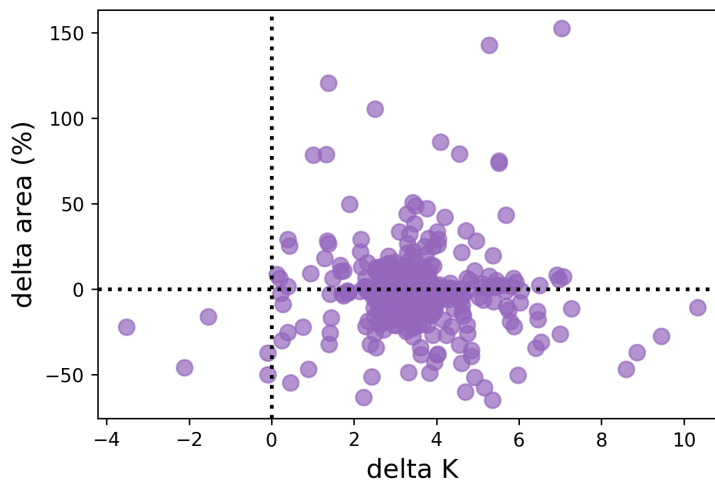


Figure 4.16: The future change in temperature (K) versus the future change in area (%) in flash flood-producing storms, where the vertical (horizontal) line denotes zero to show where future increases in temperature (area) occur.

an increase in the average percent change per degree of warming in area of flash flood-producing storms. However, due to some storms decreasing in area but experiencing a warmer temperature in the future, the 95% CI ranges from negative values ($-0.77\% \text{ K}^{-1}$) to positive ($7.1\% \text{ K}^{-1}$). Changes in area are therefore variable in a future climate, with some storms increasing in area and others decreasing. Thus, the dominant future change in flash flood-producing storms is increased maximum hourly rain rates, total accumulated rainfall, and total runoff over the entire CONUS, suggesting that more intense future flash flood-producing storms are possible.

4.4 Conclusions

High-resolution convection-permitting simulations over the CONUS are used to examine how 584 historical flash flood-producing storms will change in a future, warmer climate. The flash flood-producing storms examined occurred from 2002–2013 over the CONUS and are based on NCEI storm reports, streamflow measurements, and Stage-IV rainfall data, thus providing a holistic view of the meteorological systems and their associated rainfall that produced a notable hydrologic response (Chapter 2). The rainfall in both CTRL and PGW simulations compared well to Stage-IV rainfall observations in these historical flash floods (Figure 4.4–Figure 4.7), and those that did not were excluded from analysis. Based on the accurate depiction of flash flood rainfall in the simulations, and the ability of the PGW method to reproduce similar synoptic conditions associated with flash floods in the future, it was demonstrated that flash flood-producing storms are likely being well simulated in a future, warmer climate.

Future increases in flash flood rainfall and runoff provide additional confidence that this methodology captures flash floods in the future, especially since runoff is necessary to produce flooding. Changes in future flash flood rainfall and runoff display regional differences over the CONUS, due to different flash flood-producing storm types (Chapter 2), topography, and soil characteristics (Davis, 2001; Saharia et al., 2017a). Yet the overall increase in future rainfall and runoff over all regions suggest that flash floods may become more intense in a future climate. This future CONUS-wide increase in storm-generated runoff is 49%, which exceeds the average future 21% increase in flash flood accumulated rainfall, implying that runoff efficiency increases in a future climate. Though some locations exhibit decreased runoff efficiency in a future climate, most notably the western and eastern CONUS in respect to their median values, the average change is a net increase in runoff efficiency. Though increased storm-generated runoff is likely due to more flash flood accumulated rainfall in a future climate, other factors such as seasonal changes in evapotranspiration and soil moisture could play a role as well and is an avenue for future work.

The future increase in flash flood accumulated rainfall is tied to the intensification of maximum hourly rain rates, which increases by 7.5% K⁻¹ (median) and 10.5% K⁻¹ (average). Though the

median $\% \text{ K}^{-1}$ in maximum hourly rain rates is consistent with the theoretical Clausius-Clapeyron increase of $7\% \text{ K}^{-1}$, some individual flash flood-producing storms exceed this rate, which could be due to additional latent heat release within intense convective storms, as suggested by Trenberth (1999) and Trenberth et al. (2003), and is an area of future work. These more intense future maximum rain rates, which increase in all flash flood-producing storms, could also contribute to increased future storm-generated runoff via enhanced precipitation excess whereby intense rain rates exceed soil moisture capacity.

Other changes to flash flood-producing storm characteristics were examined, including storm area, which showed minimal change. Thus, the main changes to future flash flood-producing storms are more intense maximum rain rates, more runoff, and higher rainfall accumulation, with the latter shown in Figure 4.17. This is the composite CTRL and PGW rainfall accumulation of all 584 flash floods. Figure 4.17 shows little change in the area of rainfall in the future, but an increased maximum rainfall accumulation from approximately 50 to 60 mm. This increase in future flash flood rainfall of approximately 21%, along with increases in future maximum hourly rain rates of 27% and runoff of nearly 50% (Table 4.1), suggest that communities across the U.S. might need to prepare for more intense future flash floods. Such information is critical for policy makers, city planners, and water managers to utilize in order to create more resilient cities and update crumbling water infrastructure (Vano et al., 2019) that can withstand the effects of climate change.

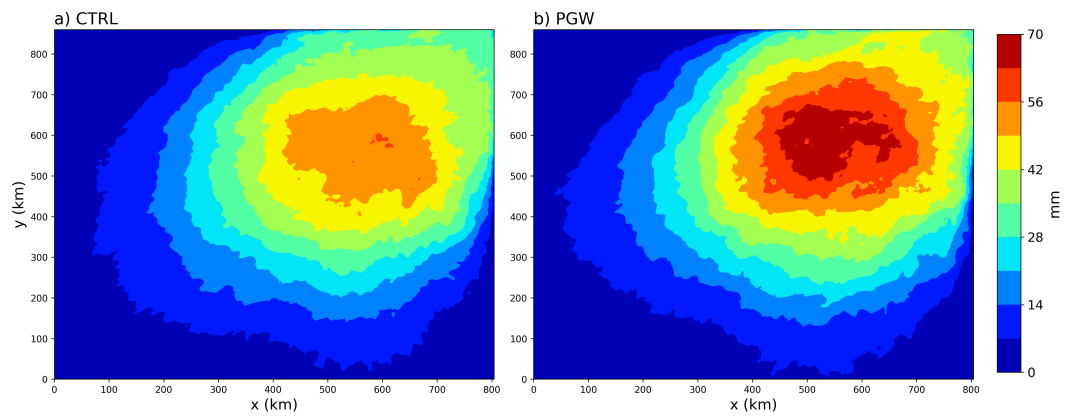


Figure 4.17: Composite area-averaged rainfall accumulations in all 584 flash flood-producing storms averaged in CTRL simulations (left) and PGW simulations (right). The x and y-axes are arbitrary and provide the size of the rainfall (km).

Chapter 5

Future Changes in the Hydrologic Cycle Associated with Flood-Producing Storms in California

5.1 Introduction

The duality of California’s Mediterranean climate from wet winters to dry summers poses a challenge in managing water resources, especially when combined with an ever-growing population (M. D. Dettinger et al., 2011a). While the wet winters in California provide most of the state’s water resources, they can also lead to floods and natural disasters. For example, the Oroville Dam catastrophe in February 2017 was caused by anomalous winter precipitation, near saturated soils, and partial melting of snowpack that contributed to excessive runoff (an entire year’s worth in January and February 2017; White et al., 2019). The anomalous precipitation in winter 2017 in California was due to an especially active season of atmospheric rivers (ARs)—the main precipitation and flood-producing systems along the United States West Coast that cause \$1.1 billion in damage annually in the West (Corringham et al., 2019).

ARs are narrow corridors of enhanced water vapor plumes in the warm sector of extratropical cyclones coming off the Pacific Ocean (Neiman et al., 2008). They are defined in a variety of ways, based upon their scale and intensity. Neiman et al. (2008) defined them as narrow plumes of integrated water vapor (IWV) exceeding 2 cm and over 2000 km long and less than 1000 km wide. They are also defined by integrated water vapor transport (IVT), with one common form of this equation given by Gao et al. (2015):

$$IVT = \sqrt{\left(\frac{1}{g} \int_{1000}^{500} qu dp\right)^2 + \left(\frac{1}{g} \int_{1000}^{500} qv dp\right)^2} \quad (5.1)$$

where g is the gravitational acceleration, q is the specific humidity, and u and v are the zonal and meridional winds, respectively. This variable quantifies the amount of water vapor transport

in the lower troposphere, where a majority of the moisture resides in ARs (Neiman et al., 2008). Typically, IVT values exceeding $250 \text{ kg m}^{-1} \text{ s}^{-1}$ are used to indicate ARs (F. M. Ralph et al., 2010, 2019; Rutz et al., 2014; Young et al., 2017), sometimes in conjunction with a spatial requirement that this IVT threshold covers a contiguous region over 2000 km long (Rutz et al., 2014). While there are a variety of ways in which ARs are defined, using an IVT threshold (whether absolute or relative) is a common method, though using different forms of this definition can yield a range in the detection of these atmospheric systems (Shields et al., 2018).

ARs are associated with heavy rainfall along the West Coast due to the shallow, moist neutral air in extratropical cyclones impinging upon mountainous terrain which results in strong forcing for orographic rainfall, particularly in the cool-season from October through March (Neiman et al., 2008). In California, ARs contribute 20–50% of California’s annual streamflow and precipitation, with only a few storms necessary to produce this contribution (M. D. Dettinger et al., 2011a). One-third to one-half of all precipitation in California falls in 5–10 days, highlighting the importance of ARs in delivering crucial precipitation to the state (M. D. Dettinger et al., 2011a). This also includes snowfall, as ARs contribute 40% of the total snow water equivalent (SWE) in California, particularly in the Sierra Nevada Mountains (Guan et al., 2010; Neiman et al., 2008).

In addition to making important contributions to rainfall and snowpack in California, ARs also contribute to flooding and landslides. F. Ralph et al. (2006) found that AR conditions were present in all seven floods on California’s Russian River from 1997–2006 and contributed to those floods due to associated heavy orographic rainfall. In December 2010, ARs produced over 670 mm of rain in the San Bernardino Mountains outside of Los Angeles and led to floods in California as well as Washington (F. Ralph & Dettinger, 2012). Young et al. (2017) specifically examined the relationship between ARs and floods, flash floods, and debris flows in California based on storm reports and a climatology of land-falling ARs from (Rutz et al., 2014). They found that floods and debris flow were associated with ARs during the cool-season in Northern California and flash floods not associated with ARs during the warm-season in Southern California. Along the West

Coast, the top 11 out of 20 counties with the highest proportion of flood damage due to ARs are located in California (Corringham et al., 2019).

Given the impact ARs have on California's precipitation, floods, and water resources, current research has investigated how ARs might change in a future climate. The frequency of ARs along the West Coast is projected to increase anywhere from 2.5 days per year (M. Dettinger, 2011b), to double the number of AR days per season (Gao et al., 2015), to 35% in the mean number of AR days (Hagos et al., 2016). M. Dettinger (2011b) showed that IWV increased in future ARs and storms were 1.8°C warmer, possibly explaining the increased number of AR days. The findings of Gao et al. (2015) demonstrate that increased AR frequency in the future is mainly due to thermodynamic rather than dynamic effects, supporting the results of M. Dettinger (2011b). Due to the changing thermodynamic effects on ARs in a future climate, future AR extreme precipitation is projected to increase by 100–200% in the fall and winter along the West Coast (Gao et al., 2015), and upwards of 200% in a case study of a flood-producing AR in the Pacific Northwest due to more orographic enhancement in a future climate (Mahoney et al., 2018). These thermodynamic changes in a future climate also affect the future hydrology in California's Sierra Nevada Mountains, with a projected decline in snowpack of 67% and increased frequency of days with runoff above 20 mm nearly tripling (Huang et al., 2018). This decrease in snowpack in a future warmer climate is due to more precipitation falling as rain rather than snow (Das et al., 2011). A future change from snow to rain leads to a projected increase in the magnitude and frequency of floods in the Sierra Nevada Mountains when using downscaled temperature and precipitation from GCMs to drive a Variable Infiltration Capacity (VIC) model (Das et al., 2011). Davenport et al. (2020) found that historical rainfall-driven floods in the western CONUS produce larger streamflow magnitudes than snowmelt-drive floods, suggesting a heightened flood risk as snow changes to rain with future warming, particularly at mid-elevation sites that receive a mix of rain and snowfall-driven floods. Thus, ARs impacting the West Coast in a future warmer climate are predicted to be more frequent and intense, producing more rainfall, less snowpack, and more runoff, suggesting an enhanced future flood risk.

While these previous studies highlight many important changes to ARs and hydrology in the Sierra Nevada Mountains in a future, warmer climate, most of these studies utilized global climate models (GCMs) to simulate future changes. GCMs are helpful for understanding the large-scale changes to future ARs, including their frequency, but due to their coarse resolution, they cannot accurately simulate precipitation processes and storm dynamics over complex terrain. This is a serious limitation for investigating changes to AR precipitation because AR precipitation is orographically enhanced and requires scales on the order of several kilometers to accurately depict the topographic effects on atmospheric flows (R. Rasmussen et al., 2011), which improves simulated precipitation up to 40–60% in nine historical ARs when increasing model resolution from 27 to 3 km (Huang et al., 2020). Though some studies like Das et al. (2011) used downscaled precipitation and temperature data from GCMs, the 12-km spatial resolution is still too coarse to properly depict precipitation and snowfall characteristics over mountainous terrain due to the topography resolution (R. Rasmussen et al., 2011) and use of a convective parameterization to simulate cloud and mesoscale dynamics. Mahoney et al. (2018) is one of the few studies to investigate changes to a land-falling AR event and its associated rainfall using high-resolution simulations of a future climate under a pseudo-global warming (PGW) framework. This is a useful demonstration of a case study, but studying how a broad spectrum of AR events change using high-resolution simulations is necessary to gain confidence in future projected changes.

The present study seeks to address these limitations and build upon the understanding of how ARs will change in a future climate by using high-resolution convection-permitting simulations that more accurately resolve complex terrain and precipitation processes along the West Coast. Specifically, this study investigates changes to cool-season precipitation and flood-producing storms associated with ARs in California in a future, warmer climate. An examination into the precipitation, SWE, and runoff changes in California's cool-season and flood-producing storms is necessary to gain a detailed understanding of how California's water resources may change in a future warmer climate.

5.2 Data and Methods

5.2.1 Convection-permitting simulations

To examine California's cool-season precipitation and floods in a future climate, 4-km convection-permitting simulations run by scientists at the National Center for Atmospheric Research (NCAR) are utilized (Liu et al., 2017). These simulations (hereafter called WRF-CONUS) were run with the Weather Research and Forecasting (WRF) model V3.4.1 over a 1360x1016 grid point domain covering the CONUS and parts of Canada and Mexico. The horizontal resolution is 4-km and there are 51 stretched vertical levels up to 50 hPa. The WRF-CONUS parameterizations include the Thompson aerosol-aware microphysics (Thompson & Eidhammer, 2014), the Yonsei University (YSU) planetary boundary scheme (Hong et al., 2006), the rapid radiative transfer model (RRTMG) (Iacono et al., 2008), and the Noah-MP land-surface model (Niu et al., 2011), which was improved for these simulations (Liu et al., 2017). For the purposes of this study, only simulations over California are considered (Figure 5.1).

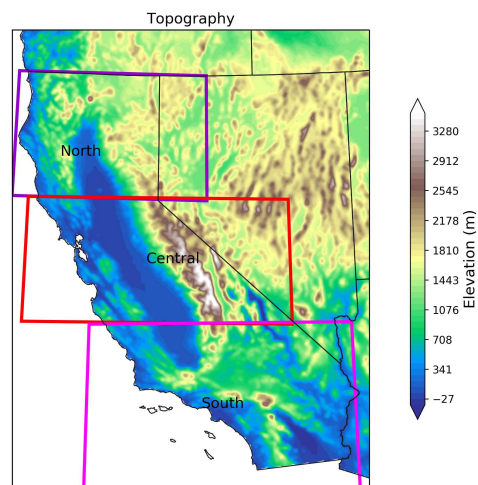


Figure 5.1: The study domain over California and its elevation to highlight the complex terrain. Also shown are boxes around three different regions in California—Northern California (purple), Central California (red), and Southern California (pink).

The WRF-CONUS simulations were forced by 6 hourly ERA-Interim reanalysis data. Two sets of simulations were run over this time-period—a current (CTRL) simulation that reproduced the present climate, and a future climate simulated using a pseudo-global warming (PGW) approach. The PGW approach adds a climate delta signal to the ERA-Interim data, as given by the following equation:

$$WRF_{input} = ERA - Interim + \Delta CMIP5_{RCP8.5} \quad (5.2)$$

where $\Delta CMIP5_{RCP8.5}$ is the 19-model ensemble monthly mean change between the current and future climate under the RCP 8.5 emissions scenario:

$$\Delta CMIP5_{RCP8.5} = CMIP5_{2071-2100} - CMIP5_{1976-2005} \quad (5.3)$$

The PGW simulations perturb the horizontal wind, geopotential, temperature, specific humidity, sea surface temperature, soil temperature, sea level pressure, and sea ice. Large-scale spectral nudging was applied to these simulations above the planetary boundary layer on horizontal scales greater than 2,000 km in order to minimize long-term climate drift (Feser et al., 2011). Nudging also allows for specific synoptic weather events to be reproduced, but sub-synoptic scales can freely evolve, thus allowing for an investigation of how storms will change in a future climate (Liu et al., 2017).

The PGW approach applied to convection-permitting simulations has been utilized in numerous studies investigating how storm processes will change in a future climate. Heavy precipitation in the CONUS (Dai et al., 2017; Mahoney et al., 2018; Prein et al., 2017a), the European Alps (Ban et al., 2015), and the United Kingdom (Kendon et al., 2014) have been studied using this method. Case studies of historical floods have also been examined from this perspective in the South-Central U.S. (Lackmann, 2013) and Pacific Northwest (Mahoney et al., 2018) to better understand how certain flood “ingredients” (Doswell et al., 1996) will change in the future. The WRF-CONUS simulations have recently been used to understand how the convective population (K. L. Rasmussen et al., 2017), mesoscale convective systems (Prein et al., 2017b, 2017c), hurricanes (Gutmann et

al., 2018), rain-on-snow events (Musselman et al., 2018), and flash flood-producing storms (Chapter 4) will change in a future climate. These simulations compare well with observations of the diurnal cycle of convection (K. L. Rasmussen et al., 2017), and outperform other gridded rainfall datasets, particularly over the mountainous West (Beck et al., 2019). This is especially critical for understanding future changes to cool-season rainfall and floods in California, most of which are orographically enhanced. The large-scale nudging used in the simulations also provides confidence that flood-producing storms are being represented in the future climate, since cool-season floods in California are largely driven by synoptic-scale ARs (M. D. Dettinger et al., 2011a; Saharia et al., 2017a), and the nudging reproduces these synoptic conditions in flood-producing storms, as shown in Chapter 4 in the case of the 2008 Arkansas flash flood.

However, there are limitations to the WRF-CONUS simulations. Due to the use of large-scale nudging and taking ensemble mean monthly differences, future changes in large-scale dynamics, including changes in storm-track, are weak and unable to be explored. Within the context of ARs, this weak large-scale dynamical change means that changes in future moisture flux are likely due to future increases in moisture rather than stronger winds, since the PGW simulations focus more on how the future thermodynamic change will affect similar weather patterns in the future (Liu et al., 2017). Yet, because the mesoscale is allowed to freely evolve, detailed changes in precipitation from a variety of weather systems can be assessed on fine horizontal resolutions that omit the need for a convective parameterization. Due to this high-resolution and the computational constraint of running the WRF-CONUS simulations, the climate change uncertainty cannot be addressed from these simulations using multi-member ensembles. Taking the 19-model ensemble monthly mean from CMIP5 simulations was done in order to partially address this limitation, rather than using a single model run as in (R. Rasmussen et al., 2014, 2011) While these limitations are notable, the purpose of the WRF-CONUS simulations to understand how today's weather might change in a warmer and moister future climate is well-suited to understand detailed precipitation changes associated with ARs in California.

5.2.2 *Cool-season climatology*

A majority of California's annual precipitation is concentrated in the cool-season from October through March, due to enhanced baroclinic cyclogenesis in the Pacific Ocean and a prevalence of land-falling ARs during this time-period (M. D. Dettinger et al., 2011a; Neiman et al., 2008). Therefore, most of California's water resources and also floods emanate from cool-season precipitation (M. D. Dettinger et al., 2011a). To understand how California's precipitation will change in a future climate, the cool-season (October through April) hydrologic components are examined in the WRF-CONUS CTRL and PGW simulations, similar to R. Rasmussen et al. (2014). Future changes in precipitation are examined using the hourly CTRL and PGW data, while changes in snow water equivalent (SWE), and total (surface + subsurface) runoff are examined using monthly totals. All quantities are presented in terms of cool-season averages and provide a holistic understanding of how California's water resources are changing in a warmer, future climate, and not just the precipitation delivered.

5.2.3 *Cool-season floods*

A majority of the cool-season precipitation in California is associated with flooding, particularly when delivered by ARs (F. Ralph et al., 2006; Young et al., 2017). In addition, as ARs make landfall on the West Coast, complex interactions with the topography and associated mesoscale processes are important factors in determining the intensity and hydrological impact of each event (Lorente-Plazas et al., 2018; Neiman et al., 2008). Thus, to understand how high-impact precipitation affecting California will change in a future climate, we focus specifically on flood-producing storms. The flood-producing storm climatology created in Chapter 2 is utilized to identify cool-season (October through April) flash and slow-rise flood-producing storms in California from 2002–2013. This climatology merges flood reports from the NCEI Storm Events Database with streamflow-indicated floods from Shen et al. (2017) and their associated rainfall characteristics from the Stage-IV precipitation dataset (Lin & Mitchell, 2005). To isolate the likely flood-contributing rainfall associated with each flood, the largest contiguous object with accumu-

lated rainfall at or above the 75th percentile within a $\pm 5^\circ$ latitude/longitude grid box from the flood centroid was identified. Flash floods in the flood-climatology from Chapter 2 are shorter duration, high intensity events usually associated with convection, while slow-rise floods are longer duration, moderate intensity events associated with larger-scale synoptic events. Young et al. (2017) showed that a majority of flash and slow-rise floods in California during the cool-season are associated with ARs. Thus, the cool-season floods in California identified from Chapter 2 are likely associated with ARs.

69 flood-producing storms are identified in California from 2002–2013. The date and location of floods from the Chapter 2 climatology are used to subset the hourly CTRL and PGW precipitation data, again only using the largest contiguous area with rainfall accumulations meeting or exceeding the 75th percentile within the flood domain ($\pm 5^\circ$). These heavy rainfall objects are computed separately in the CTRL and PGW simulations to take into account that the amount and location of heavy rainfall within each flood domain could change slightly in a future, warmer climate. However, the accumulated rainfall (as well as SWE, temperature, and runoff) are computed using the same dates from Chapter 2 in the CTRL and PGW simulations. While this is a possible limitation of the study, due to the possibility of rainfall within a flood event being longer or shorter in duration in a future climate, the use of spectral nudging ensures similar synoptic situations and durations in the PGW simulations. Given that flood events associated with ARs are synoptically driven, it was expected that the CTRL flood location, rainfall structure, and duration would compare well with observations and to PGW simulations.

To test this expectation, each of the 69 floods in the CTRL simulations are compared to Stage-IV observations and PGW simulations. Between CTRL simulations and Stage-IV, if the area-averaged rainfall difference exceeds 50% within a flood, a manual comparison occurs. This manual comparison is conducted using observed daily archived precipitation data over California from the Advanced Hydrologic Prediction Center (<https://water.weather.gov/precip/>). In the Western CONUS, the daily archived precipitation data is derived from the Parameter-elevation Regressions on Independent Slopes Model (PRISM; Daly et al., 1994) dataset, due to issues in

Stage-IV coverage over the mountainous West. Based on a qualitative comparison of CTRL simulated precipitation with PRISM precipitation, 24 floods are omitted, leaving 27 (18 flash (slow-rise) flood-producing storms for a total of 45 cool-season floods in California.

Among these 45 cool-season floods, the similarity between rainfall amount and structure in CTRL and PGW simulations is quantified using the structural similarity index (SSIM) from Wang et al. (2004)

$$SSIM(x, y) = \frac{(2\mu_x\mu_y + c_1)(2\sigma_{xy} + c_2)}{(\mu_x^2 + \mu_y^2 + c_1)(\sigma_x^2 + \sigma_y^2 + c_2)} \quad (5.4)$$

where x, y is the pixel location, μ is the mean pixel intensity, σ is the variance of intensity, and c_1 and c_2 are constants to avoid instability when the other terms in the denominator are close to zero. SSIM is often used in the image-processing community to compare the difference in two images luminance, contrast, and structural differences. In this study, SSIM is utilized to compute differences in accumulated rainfall amount and structure between each flood in the CTRL and PGW simulations like in Chapter 4, where this metric is computed for 584 flash flood-producing storms over the CONUS and found good agreement between both the observations and CTRL simulation, and the CTRL and PGW simulations. This metric quantifies the similarity of the rainfall structure between CTRL and PGW simulations over the same time period and location for each of the 45 floods in California to ensure that a similar flood occurs in the future.

Computing the SSIM between the CTRL and PGW accumulated rainfall for all 45 floods in California results in a mean value of 0.94, with values ranging from 0.88–0.99 (Figure 5.2). A value of 1 indicates exact similarity, so a mean value of 0.94 suggests that the CTRL and PGW precipitation is remarkably similar in floods-producing storms. Even for the flood with the lowest SSIM of 0.88, the rainfall structure and location is similar (Figure 5.3). Though exact agreement is not expected between CTRL and PGW flood precipitation due to a different thermodynamic environment in PGW simulations, the high SSIM values are likely due to the PGW simulations' ability to reproduce the synoptic environment in the CTRL simulations.

(Maddox et al., 1980, 1979) showed that similar synoptic environments are associated with floods, including ARs, which are, by definition, synoptically-driven. Therefore, while remarkable,

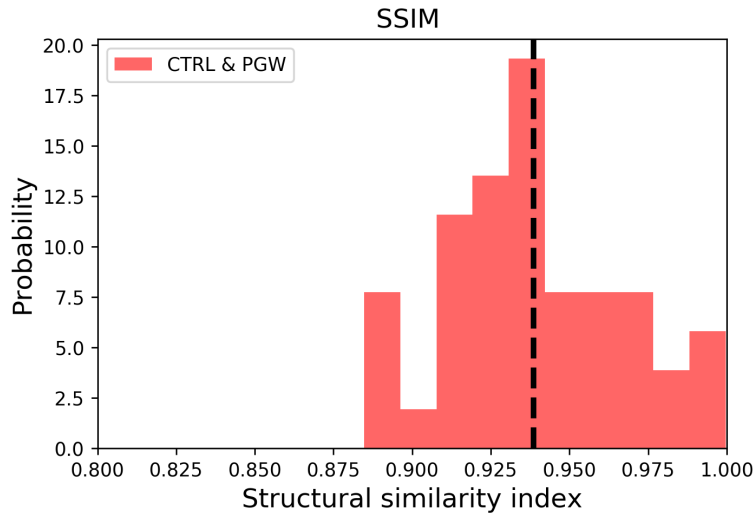


Figure 5.2: Probability density function of the structural similarity index from Wang et al. (2004) used to compute the structural differences in rainfall accumulation among 45 cool-season floods in California in CTRL vs. PGW simulations. The mean value is indicated by the dashed vertical line.

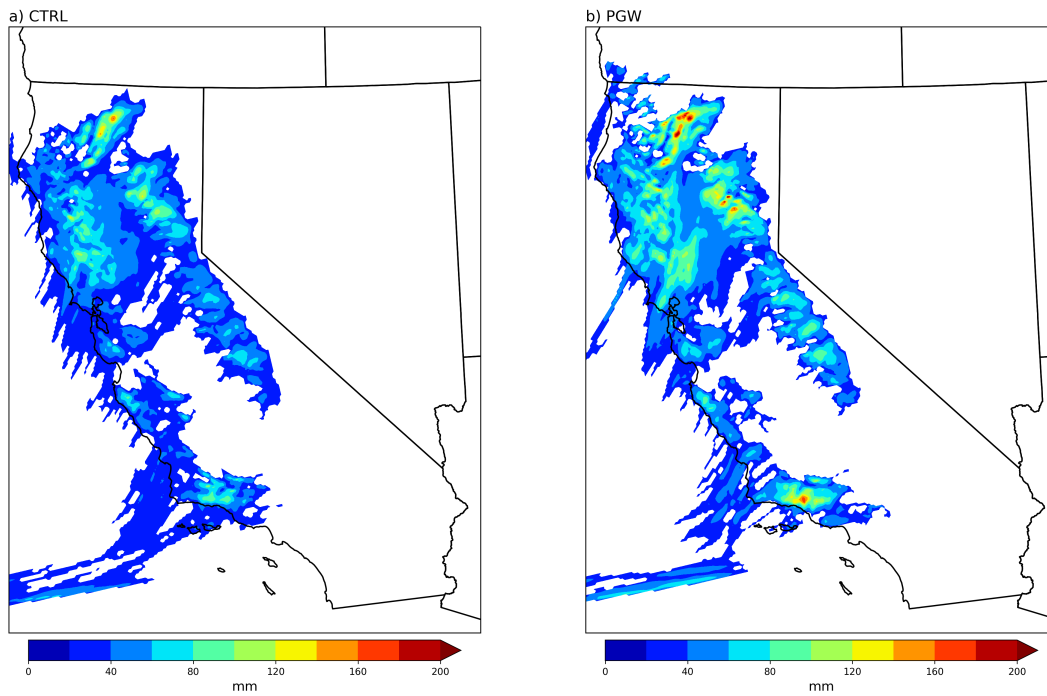


Figure 5.3: The accumulated rainfall in a) CTRL simulations and b) PGW simulations for a slow-rise flood that occurred from 0000–2200 UTC 20 January 2010. This flood had the lowest structural similarity index among all 45 cool-season floods in California of 0.88.

it is not surprising that the PGW simulated rainfall in floods likely associated with ARs in California is similar to the CTRL simulations, based on the simulation design and the types of floods

examined. These results provide confidence that flood-producing storms in the current climate are being reproduced in the PGW simulations in terms of location, timing, and structural similarity of precipitation. However, future changes in soil-moisture, land-use, and streamflow are not assessed in this study, which could modulate the occurrence of floods in a future climate. Therefore, it cannot be said with certainty that storms associated with floods in the current climate also produce floods in the future.

Work by Young et al. (2017) showed that nearly 80% of floods and debris flow were associated with ARs in California. The Rutz et al. (2014) AR database using Modern Era Retrospective Analysis (MERRA; Rienecker et al., 2011) reanalysis data from 1980–2019 was utilized to confirm that the flood-producing storms in this study were associated with AR conditions. If the start date of flood-producing storm was less than or equal to two days from the end date of an AR event from Rutz et al. (2014), then that storm was classified as being associated with an AR. Based on this definition, all 45 flood-producing storms were associated with ARs. Given the association with AR conditions, it is likely that these flood-producing storms result in floods in the future.

In addition to precipitation, changes in SWE and runoff are examined using the CTRL and PGW hourly data among the 45 floods. Integrated water vapor transport (IVT) is also compared in CTRL and PGW flood-producing storms using Eqn. (1), since this quantity is often used to define ARs (Gao et al., 2015; F. M. Ralph et al., 2019; Rutz et al., 2014). IVT has a particularly important link to precipitation, as it is strongly related to precipitation over complex terrain (Junker et al., 2008; Neiman et al., 2013, 2002; F. Ralph et al., 2013). Therefore, an understanding of how IVT changes in future California floods associated with ARs is crucial to explain how rainfall in these flood-producing storms might change.

5.3 Results

5.3.1 *Cool-season climatology*

Average cool-season precipitation over California increases almost everywhere in a future climate (Figure 5.4), especially over the complex terrain of the Coastal Range and Sierra Nevada

Mountains (refer to Figure 5.1 for topography). Precipitation increases from 40–120 mm in most of the state, with increases of up to 180 mm over the Sierra Nevada Mountains. Localized areas of decreased precipitation occur on the leeward side of the Southern Coastal Range, but these decreases are minimal (40 mm decrease) and occur in a climatologically dry area. The statewide increase in future precipitation is 49 mm (11%). Such an increase in future precipitation during California’s cool-season is not unexpected, as water vapor increases in a warmer climate according to the Clausius-Clapeyron equation (Trenberth et al., 2003). The greatest future increase in precipitation over complex terrain is also not surprising, as orography enhances forcing via mechanical lifting for precipitation.

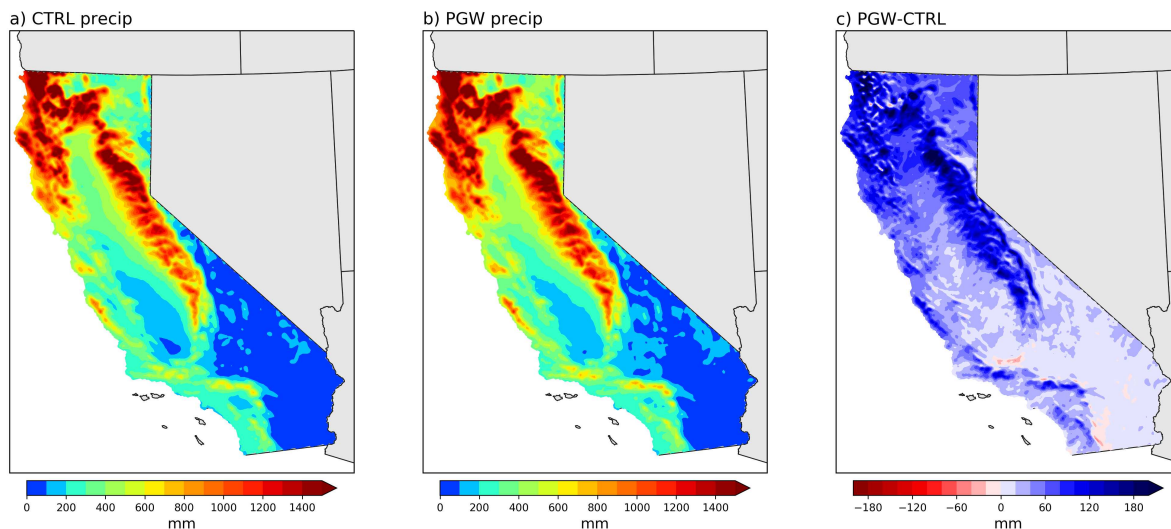


Figure 5.4: Average cool-season (October–April) precipitation over California in a) CTRL simulations, b) PGW simulations, and c) PGW-CTRL difference, where blue indicates increased PGW precipitation and red indicates a decrease.

Future changes in cool-season SWE show the opposite change compared to precipitation, with an average decrease of 57.5 mm (47.5%; Figure 5.5). Decreased SWE is greatest over the Sierra Nevada Mountains, which receive the climatological maximum snowfall in California (Huang et al., 2018). These decreases are up to 360 mm over the mountains, and no locations display an increase in average cool-season SWE. Such a result is particularly concerning, as California relies on most of its water resources from seasonal snowpack accumulations (M. D. Dettinger et al.,

2011a). Changes in snow have already been observed in the Sierra Nevada Mountains, with an increase in the observed mean snow line over the last 15 years (Hatchett et al., 2017). Future decreases in snow have also been shown in the Colorado Rockies and high-elevation locations in the Pacific Northwest, with future warming causing a shift from rain to snow (Mahoney et al., 2018; R. Rasmussen et al., 2014). Furthermore, Huang et al. (2018) showed that for the 2016–2017 season, maximum SWE decreases by 67% under RCP8.5 using a 9-km downscaled simulation of the future climate. Given that these results span a longer time frame than Huang et al. (2018), include all of California, and properly resolve orographic precipitation processes (R. Rasmussen et al., 2014), the 47.5% average decrease in California’s cool-season SWE should be seriously considered.

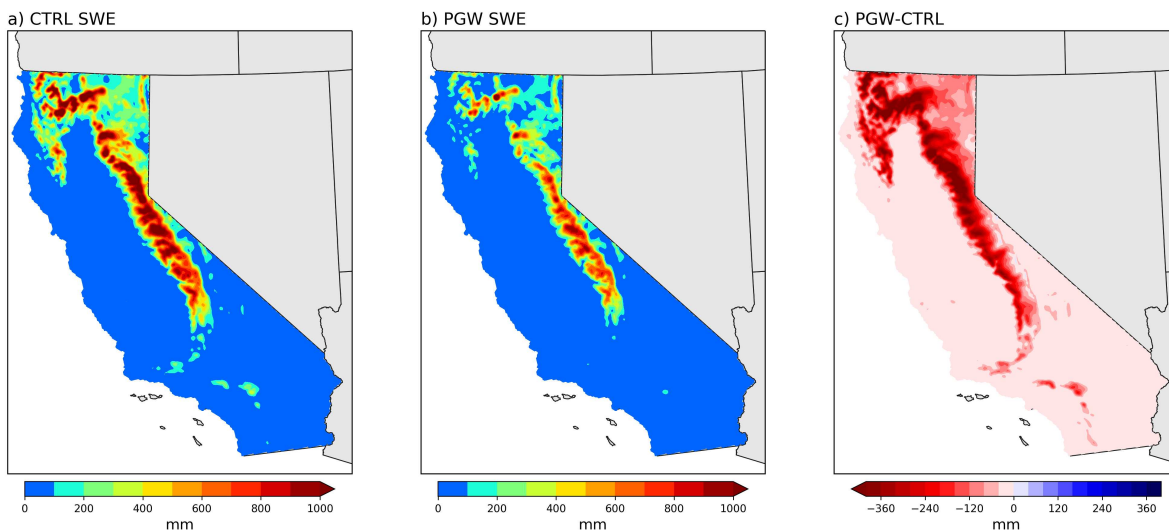


Figure 5.5: As in Figure 5.4., but for snow water equivalent (SWE).

The above changes in future cool-season precipitation and SWE due to warming contribute to changes in future cool-season runoff (Figure 5.6). On average, cool-season runoff increases 51.8 mm (27.1%), with a majority of California experiencing increased runoff, except for some localized areas in southern California that experience slight decreases in runoff less than 50 mm. Increased runoff is greatest over the Sierra Nevada Mountains, due to the greatest increase (decrease) in precipitation (SWE) here, with average increased runoff up to 450 mm. This is consistent with

R. Rasmussen et al. (2014) and Schwartz et al. (2017) who found more precipitation falling as rain rather snow in a future climate, which led to increased winter runoff in the Colorado Rockies (R. Rasmussen et al., 2014), and earlier snowmelt and runoff in the Sierra Nevadas (Schwartz et al., 2017). Huang et al. (2018) also found that runoff increases under RCP8.5 in a future simulation of the 2016–2017 wet year in the Sierra Nevada Mountains, with days of runoff exceeding 20 mm nearly tripling. The future increases in cool-season runoff in California due to increased precipitation and decreased SWE not only suggest a shift in the water balance, but also an enhanced future flood risk, which will be explored further in Section 5.3.2.

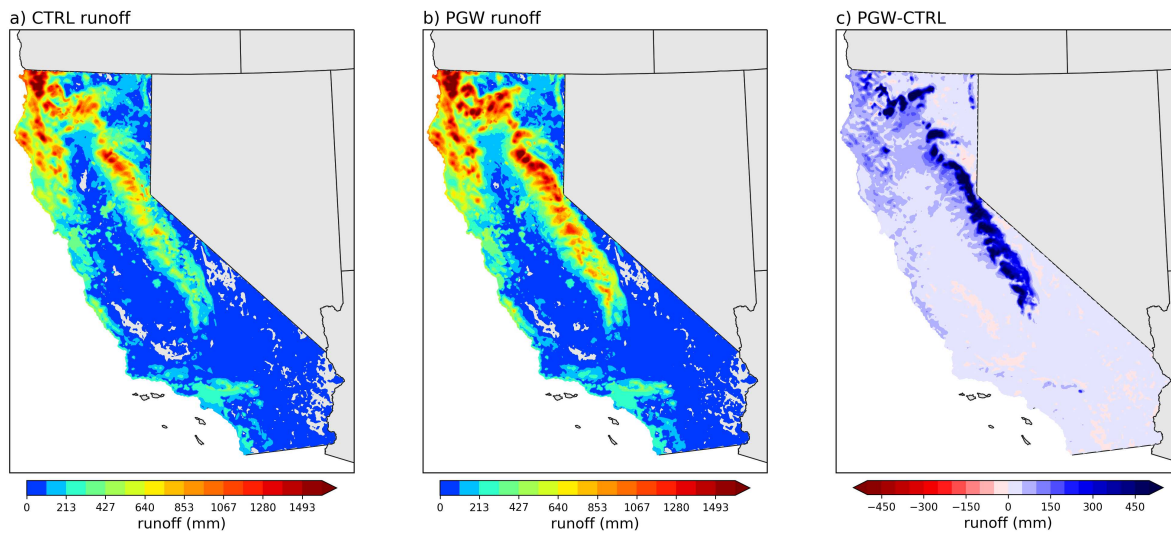


Figure 5.6: but for runoff.

To further understand the nuances of future changes in cool-season precipitation, SWE, and runoff, the dependence on elevation in California is explored (Figure 5.7). Consistent with Figure 5.4–Figure 5.6, future precipitation increases at all elevations, up to 200 mm. SWE decreases at all elevations in the future, as seen in Figure 5.5, with a maximum decrease of nearly 800 mm between 1500–2000 m in elevation, and smaller decreases in SWE above and below this elevation. This large decrease in SWE at mid-elevations is consistent with projected future changes in the 2016–2017 1 April SWE in the Sierra Nevada Mountains, during which SWE between 1500–2500 m almost disappears, and high-elevation (> 2500 m) SWE is halved (Huang et al., 2018). The

maximum decrease in SWE at mid-elevations is likely due to higher freezing levels in a warmer climate that converts snow to rain (Mahoney et al., 2018; R. Rasmussen et al., 2014). Interestingly, R. Rasmussen et al. (2014) found that at the highest elevations in the Colorado Rockies, temperatures were still cold enough to support increased snow in the future, which is not the case in California. This could be due to most of the cool-season precipitation in California being delivered by ARs, which tend to be associated with warmer than normal conditions and thus, high snowlines (M. D. Dettinger et al., 2011a; Neiman et al., 2008). Due to the overall increase in precipitation and decrease in SWE, future runoff increases at and above mid-elevations (1500 m), where snow is likely falling as rain in a future warmer climate. This is consistent with future increased runoff at mid and high-elevations in the Sierra Nevada Mountains for the 2016–2017 season (Huang et al., 2018), and increased runoff in the spring in the Colorado Rockies (R. Rasmussen et al., 2014). Such a result suggests an increased flood risk at mid-elevations as snow changes to rain in a future climate, since rainfall-driven events have higher streamflow magnitudes than snowmelt-driven events (Davenport et al., 2020).

The seasonality of precipitation, SWE, and runoff are explored for the cool-season in California to examine if there were any shifts in the seasonality of these components, and thus, the water balance. Future precipitation and runoff increase through the entire cool-season (October through the end of April), with maximum increases in January–March ranging from 15–20%, and 20–40%, respectively (Figure 5.8). SWE decreases in the future from October through April, with the greatest decreases of over 60% in the early-season (October–December). Not much SWE exists in California in October (the statewide average is 4 mm in CTRL simulations), so the future decrease is only a few mm averaged over the state, despite the large percentage decrease. However, the large future decrease of nearly 70–80% in November and December SWE is likely robust, as California climatologically experiences large gains in SWE during these months (Neiman et al., 2008).

For most of the cool-season in California, there does not appear to be a future shift in the timing of precipitation, SWE, or runoff, but simply increased (decreased) precipitation and runoff

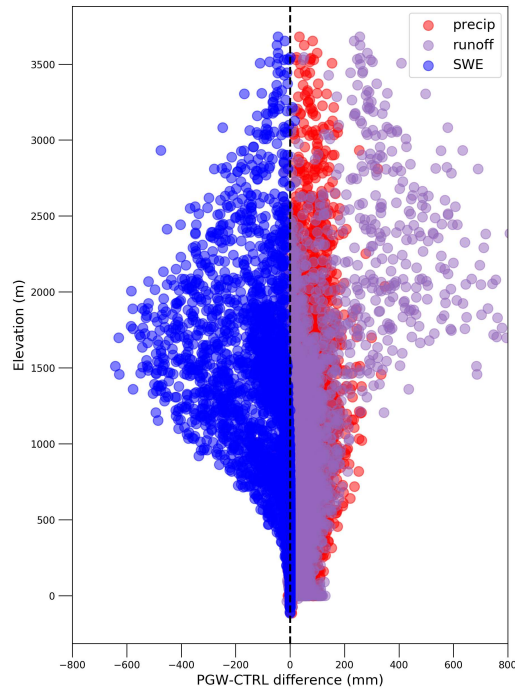


Figure 5.7: PGW–CTRL difference in cool-season precipitation, runoff, and SWE shown in Figure 5.4–Figure 5.6, as a function of altitude over California.

(SWE). The only exception occurs on the fringes of the cool-season, where precipitation and runoff slightly decrease in the future in December and April. The decrease in precipitation and runoff in April could indicate earlier snowmelt, especially since SWE decreases more in April than the previous months. Such a result would be consistent with Huang et al. (2018) who found that early-season gains in Sierra Nevada runoff (January in February) in a future climate came at the expense of decreased late-season runoff (April–June). The present study only explores the cool-season, however, so any changes in the seasonality beyond this timeframe cannot be stated. Yet, these results are consistent with future changes in water balance components in the Colorado Rockies (R. Rasmussen et al., 2014) and Sierra Nevada Mountains during the 2016–2017 season (Huang et al., 2018)—namely the future increases (decreases) in precipitation and runoff during the middle (edges) of the cool-season, and largest decreases in SWE on the edges of the cool-season in Cal-

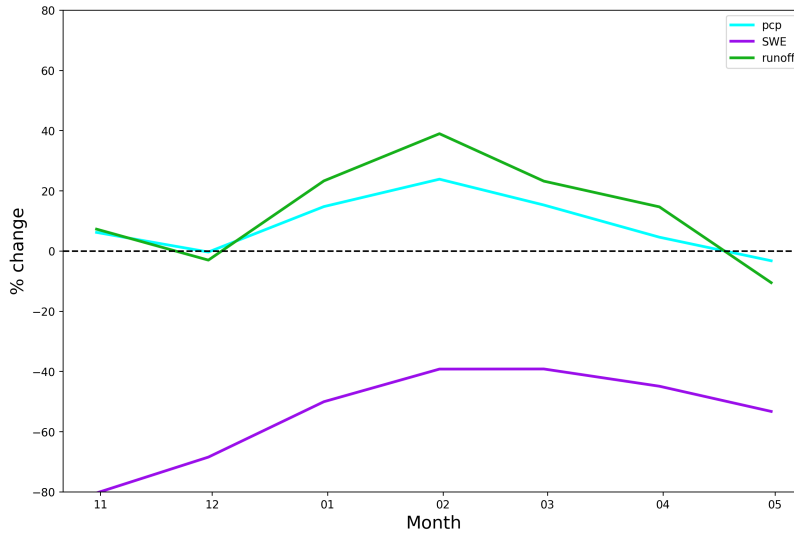


Figure 5.8: Seasonality from October–May of percent future change in precipitation (turquoise), SWE (purple), and runoff (green). The dashed line at zero indicates no change, while values above (below) the line indicate a future percent increase (decrease). Note that the percent change is computed as PGW-CTRL/CTRL *100.

ifornia. This provides confidence in the expected future changes in the water balance and water resources in California in a warmer climate.

5.3.2 Cool-season flood-producing storms

Future cool-season flood-producing storms in California show an increase in precipitation everywhere (Figure 5.9), similar to changes in overall cool-season precipitation (Figure 5.4). However, the future percent increase in flood-producing storm precipitation exceeds the cool-season precipitation, with increases of 25.4% (7.1 mm) in northern California (NorCal), 25.8% (5.3 mm) in central California (CenCal), and 21.7% (3.3 mm) in southern California (SoCal; Table 5.1–Table 5.2). These increases are less than the projected future precipitation increases in ARs simulated by Mahoney et al. (2018) and Gao et al. (2015), who found increased precipitation up to 200%. These differences could be due to Mahoney et al. (2018) only considering one land-falling AR case in the Pacific Northwest, which are different in nature than land-falling ARs in California (Neiman et al., 2008). Additionally, Gao et al. (2015) concentrated on future changes to land-falling ARs on the West Coast and their extreme (> 95th percentile) precipitation using

GCMs, rather than the entire distribution of precipitation using a convection-permitting model, as is considered in this study. Using future ensemble changes in CMIP5 members rather than just the mean change, as is considered in the present study, is another reason why the projected increase in precipitation in the current study is possibly less than that in Gao et al. (2015).

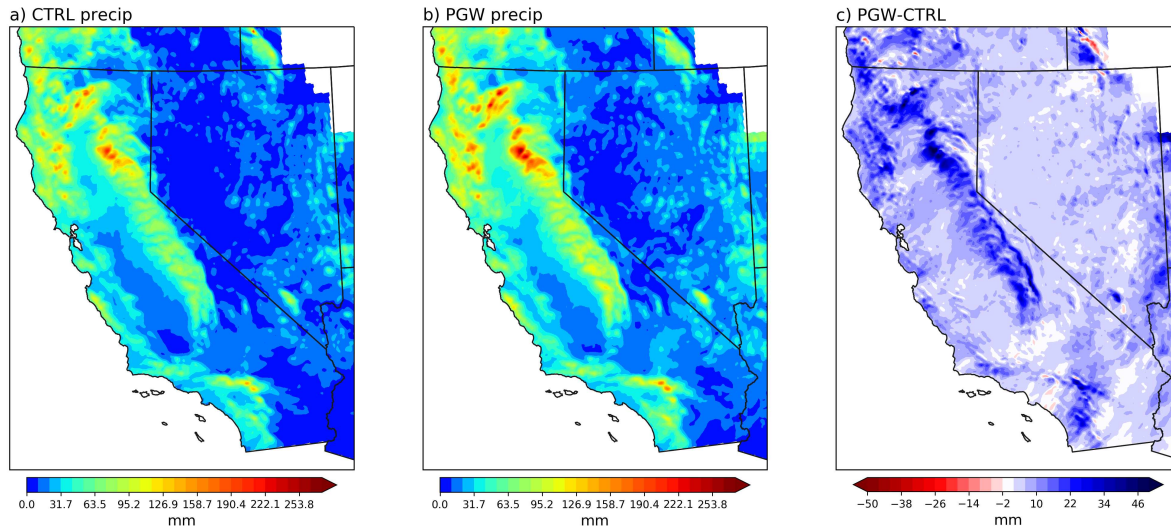


Figure 5.9: As in Figure 5.4 but for average precipitation in 45 cool-season flood-producing storms in California between 2002–2013.

Table 5.1: Future percent change in precipitation, snow water equivalent (SWE), and runoff in 45 flood-producing storms in California from 2002–2013. The future percent change is $PGW-CTRL/CTRL * 100$ in different California regions (North, Central, South).

	North	Central	South
Average precipitation (%)	25.4	25.9	21.7
SWE (%)	-68.3	-32.0	-89.6
Runoff (%)	34.4	28.9	15.3

Future changes in SWE among California flood-producing storms, which has not been examined in much detail before, display an overall decrease (Figure 5.10). This decrease is largest in SoCal of -89.6% (Table 5.1), but SoCal does not receive much SWE in a current climate (Fig-

Table 5.2: As in Table 5.1 but for the raw future change (PGW–CTRL) in temperature, precipitation, SWE, and runoff.

	North	Central	South
Temperature (K)	3.8	3.8	3.6
Average precipitation (mm)	7.1	5.3	3.0
SWE (mm)	-4.0	-1.7	-0.3
Runoff (mm)	4.4	2.2	1.2

ure 5.10b), so the absolute decrease of 0.3 mm in SWE in a future climate is minimal (Table 5.2). However, the future decrease in NorCal SWE of -68.3% (-4.4 mm) is notable, as it receives 50–130 mm of SWE on average from cool-season flood events in the CTRL simulations. Interestingly, CenCal exhibits the least future decrease in SWE in a future climate, with a -32% (-1.7 mm) average decrease. This region contains some of the highest mountains, and the highest SWE in the CTRL simulations, with large areas of SWE exceeding 100 mm (Figure 5.10a). The reason for the lesser decrease in SWE in CenCal is because some areas in the Sierra Nevadas exhibit a future increase in SWE, up to 20–30%. This is along the highest terrain of the Sierra Nevadas (Figure 5.1), and the increase is due to future temperatures in this region staying below freezing (< 273 K; Figure 5.12), thus allowing for frozen precipitation to continue despite a warmer climate. Some mid-elevation (1500–2500 m) locations are also below freezing in the future, but these places show a 0–25 mm decrease in SWE. The reason for the future increases in SWE at the high elevations that are below freezing in the future climate, but not mid-elevations is unclear, but results are consistent with R. Rasmussen et al. (2014), and could be due to mid-elevations sites receiving a mix of rain and snow, depending on the individual flood-producing storm characteristics.

The future increase in precipitation and decrease in SWE in flood-producing storms in California results in increased future runoff over the entire state (Figure 5.11), similar to the cool-season climatology. Runoff increases range from 15.3% (1.2 mm) in SoCal to 34.4% (4.4 mm) in NorCal, with the greatest increases along complex terrain. The increased runoff is consistent with future changes in the Sierra Nevada Mountains (Huang et al., 2018) and the Colorado Rockies

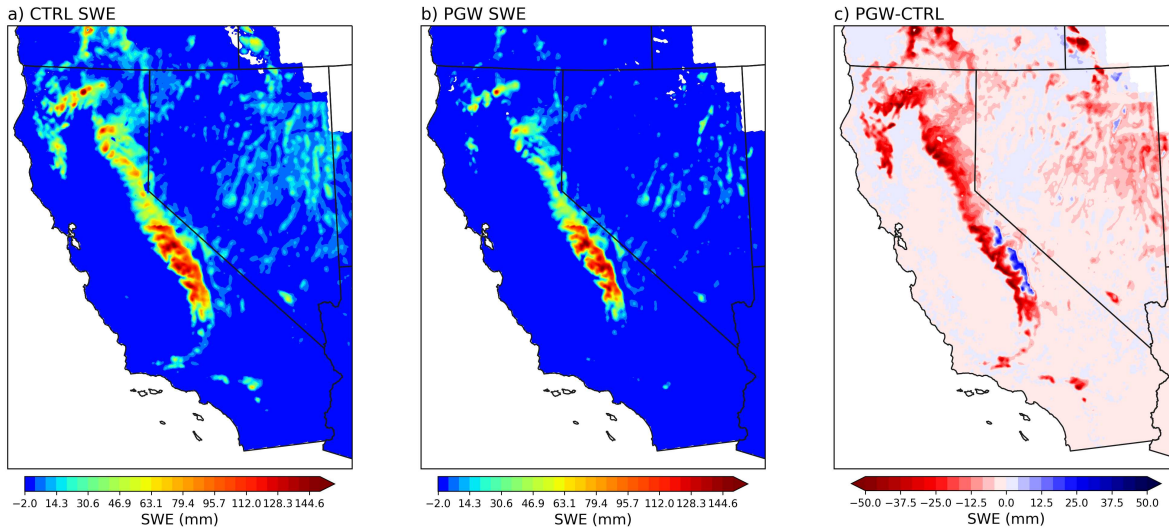


Figure 5.10: As in Figure 5.5, but for average SWE in 45 cool-season flood-producing storms in California between 2002–2013.

(R. Rasmussen et al., 2014), due to the change from rain to snow, and overall increased precipitation. Given that ARs are associated with anomalously warm conditions in the present climate that exacerbate rain-on-snow flood risks (Neiman et al., 2008), and future temperatures in cool-season flood-producing storms increase by approximately 4 K (Table 5.2), future warming likely enhances rain-on-snow flood risk (Musselman et al., 2018) or purely rainfall-driven flood risk (Davenport et al., 2020), and contributes to increased runoff. Thus, cool-season flood-producing storms in California in a future climate appear to be more intense due to increased precipitation and runoff, and decreased SWE, consistent with future projections of floods in the Sierra Nevada Mountains that show increased streamflow magnitudes due to more frequent storms and precipitation falling as rain rather than snow (Das et al., 2011).

To understand why precipitation and runoff increase in future cool-season flood-producing storms in California, future changes to IVT are examined. IVT is not only used to indicate AR occurrence (F. M. Ralph et al., 2010, 2019; Rutz et al., 2014; Young et al., 2017) but is also strongly related to orographic precipitation (Junker et al., 2008; Neiman et al., 2013, 2002; F. Ralph et al., 2013). In the CTRL simulations, average IVT during flood-producing storms in California is $250 \text{ kg m}^{-1} \text{ s}^{-1}$, with a defined IVT plume in the lower half exceeding values of 290 kg m^{-1}

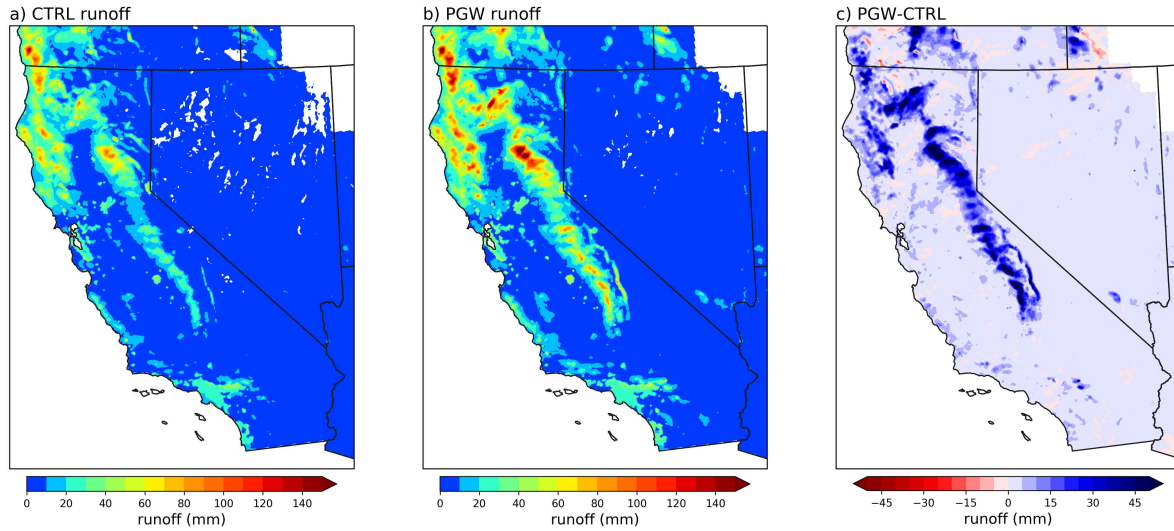


Figure 5.11: As in Figure 5.6, but for average runoff in 45 cool-season flood-producing storms in California between 2002–2013.

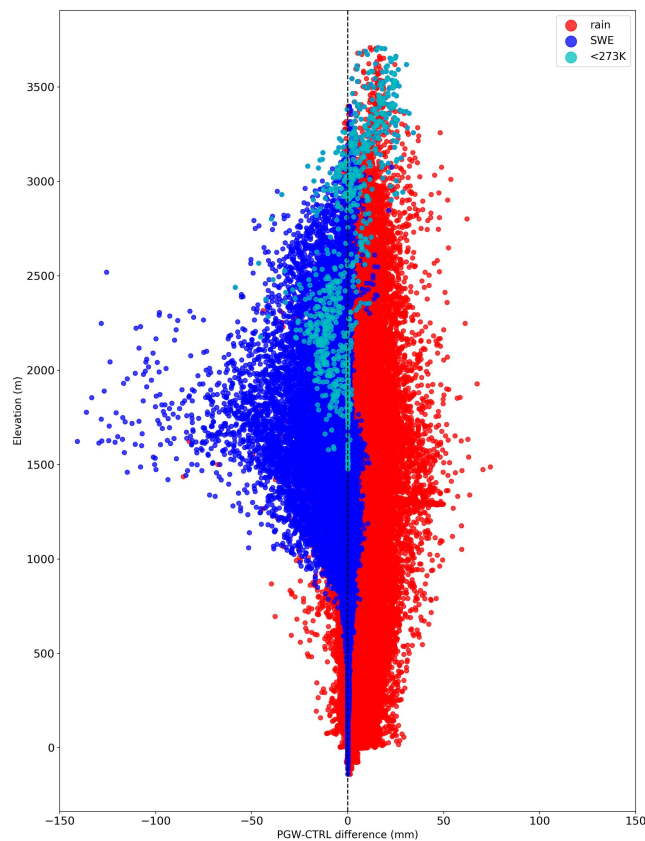


Figure 5.12: PGW-CTRL differences in precipitation (red dots) and SWE (blue dots) 45 flood-producing storms in California as a function of altitude. Turquoise (dark blue) colored-dots indicate SWE changes in storms where the temperature is below (above) freezing (273 K) in the PGW simulations.

s^{-1} (Figure 5.13). Given that the IVT threshold for AR identification is at or equal to $250 \text{ kg m}^{-1} \text{ s}^{-1}$ (F. M. Ralph et al., 2010, 2019; Rutz et al., 2014; Young et al., 2017), this confirms the identification of 45 flood-producing storms being associated with ARs based on the Rutz et al. (2014) database. In the future, the average IVT increases by $100 \text{ kg m}^{-1} \text{ s}^{-1}$ to $350 \text{ kg m}^{-1} \text{ s}^{-1}$ (Figure 5.13). M. Dettinger (2011b) similarly found that future ARs become more intense, with increases in IWV. Gao et al. (2015) discovered that this thermodynamic (water vapor) effect dominates over the dynamical (wind) effect in explaining the 50–600% increase in future AR days along western North America. This thermodynamic effect of increased water vapor, which is simulated using the PGW methodology in this study, likely explains much of why IVT increases in a future climate in association with flood-producing storms. Therefore, stronger future ARs associated with cool-season floods in California is consistent with prior work, with the present study additionally showing that the stronger ARs are associated with increased precipitation and runoff due to enhanced water vapor transport in California flood-producing storms.

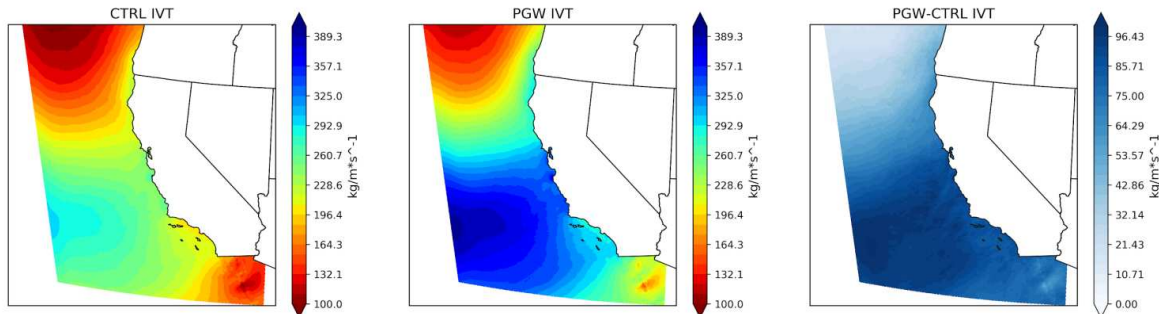


Figure 5.13: As in Figure 5.11, but for integrated water vapor transport (IVT).

5.4 Conclusions

High-resolution convection-permitting simulations are utilized to understand future changes to California’s precipitation, SWE, and runoff in 45 AR flood-producing events as well as the entire cool-season. Given the ability of the PGW simulations to reproduce the precipitation structure and amount in these flood-producing storms over the same duration and location as CTRL simulations,

there is confidence that storms producing floods in the current climate also occur in the future, likely resulting in a flood due to their association with AR conditions. While studies have previously investigated future changes to ARs impacting the West Coast, including a flood caused by an AR (Mahoney et al., 2018), this is the first study to examine changes in a large number of flood-producing storms and the cool-season's hydrologic components using a convection-permitting regional climate model framework. Such information is critical to understand how California's water resources will change in a future climate, and the use of high-resolution simulations are necessary for accurately depicting the complex orographic processes and storm dynamics leading to such changes in a future, warmer climate.

Future changes in California's cool-season flood-producing storms associated with ARs are similar to changes in the cool-season climatology of precipitation, SWE, and runoff. This result suggests that changes in future AR flood-producing storms will significantly affect California's water resources, given that a majority of the state's water resources are due to cool-season precipitation from ARs (M. D. Dettinger et al., 2011a; Neiman et al., 2008). Flood-producing storm precipitation increases 22–26% in the future likely due to increased water vapor via the Clausius-Clapeyron relationship (Trenberth et al., 2003) and increased average IVT of $100 \text{ kg m}^{-1} \text{ s}^{-1}$. Thus, the ARs associated with floods will likely become more intense in a future climate, leading to enhanced precipitation. However, due to the approximately 4° C warmer temperatures in these storms (Table 5.2), flood-producing storm SWE decreases by 32–90% in the future, mostly over the Sierra Nevada Mountains. Only at the highest elevations (i.e., above 3000 m) does SWE increase in the future, due to temperatures staying below freezing. The overall increase (decrease) in flood-producing precipitation (SWE) results in increased future runoff between 15–34%.

Increases in future precipitation and runoff suggests that flood-producing storms will become more intense in a future climate in California. Decreases in future SWE imply decreased available water resources available for California, given that this provides approximately 60% of the state's developed water (Huang et al., 2018). While extending this analysis through the entire year would allow for a more accurate determination of changes in future SWE (especially snowmelt during

May and June) and water resources, the results of the present study have serious implications for California. More intense future flood-producing storms and less future water resources in California are two detrimental impacts of climate change that must be taken into account in future water management strategies. Vano et al. (2019) specifically highlighted the need of water managers to understand how flood-producing storms will change in the future, and this study directly addresses those needs. Thus, such results should be considered in water management plans in California in order to effectively capture the excessive precipitation and runoff projected in future flood-producing storms, especially since the main current water source—snowpack—might not be able to provide for the state’s ever-growing population in a warmer climate.

Chapter 6

Flash Flood-Producing Storms in a Current and Future Climate in the Mississippi River Basin

6.1 Introduction

In the continental United States (CONUS), floods are the second deadliest weather-related natural disaster (Ashley & Ashley, 2008b) and accounted for over \$123.5 billion in adjusted losses between 1980–2018 (A. B. Smith, 2019). Deadly flash flooding in Texas and Arkansas from 9–11 June 2010 resulted in over \$10 million in damage along the Guadalupe River in Texas and 20 fatalities at the Albert Pike Recreational Area in western Arkansas (Schumacher et al., 2013). This devastating flood was due to a mesoscale convective vortex (MCV) associated with a series of heavy rainfall-producing mesoscale convective systems (MCSs; R. A. Houze Jr, 2004; Schumacher et al., 2013). Such high intensity flash flood-producing storms are common to the Mississippi River Basin (MRB), which are the most frequent and have the highest average rainfall accumulation of any region in the United States (Chapter 2). This region has thus been identified as a flash flood hotspot (Saharia et al., 2017a), with flash floods occurring year-round (Saharia et al., 2017a). The deadliest of these flash floods in the MRB occur mainly due to fronts and MCSs (Ashley & Ashley, 2008b), particularly in the warm season (Ashley & Ashley, 2008b; Saharia et al., 2017a; Schumacher & Johnson, 2006). The risk posed by warm-season flooding in the MRB is exacerbated by the poor predictability of extreme rainfall events (Herman & Schumacher, 2018a; Sukovich et al., 2014) due to issues representing moist convection in operational models (J. M. Fritsch & Carbone, 2004). Given the frequency and intensity with which flash floods impact the MRB, it is critical better understand the factors causing these events in order to improve the predictability of such events in order to protect human life.

To help improve flash flood forecasting, Doswell et al. (1996) produced a seminal paper on the ingredients necessary for flash floods to occur, as summarized by the following equation:

$$P = \bar{R}D \quad (6.1)$$

where P is precipitation, \bar{R} is the average rainfall rate, and D is the rainfall duration. This equation shows that for heavy precipitation and flash flooding to occur, high rain rates must be sustained over a long duration. Expanding 6.1 based on terms related to \bar{R} and D :

$$P = EwqL_s (|C_s^{-1}|) \quad (6.2)$$

where E is precipitation efficiency, w is vertical motion, q is moisture, L_s is the system size, and C_s is the system motion vector. Most storms do not have all of these ingredients maximized, but MCSs often have many, making them major flood-producers in the Midwest and the MRB (Ashley & Ashley, 2008b; J. Fritsch et al., 1986; Kunkel et al., 2012; Schumacher & Johnson, 2006). MCSs typically occur in environments with a deep saturated layer, high relative humidity, moderate convective available potential energy (CAPE), little convective inhibition (CIN; Schumacher & Johnson, 2009), and sometimes exhibit back-building—the repeated formation of convective cells upstream of their predecessors (Schumacher & Johnson, 2005). Similarly, tropical cyclones are large systems with high moisture content that can sometimes move slowly, depending on the synoptic conditions. These same ingredients in tropical cyclones lead to flooding that affects the MRB in summer and fall (Ashley & Ashley, 2008b; Schumacher & Johnson, 2006; Villarini et al., 2014). Convective airmass thunderstorms that are generated due to strong daytime surface heating in the summer also lead to flooding in the MRB (Ashley & Ashley, 2008b; Kunkel et al., 2012), but they tend to be smaller, more isolated, and more transient than other types of flood-producing storms in the MRB.

An understanding of the storm dynamics associated with flash floods in the MRB in the current climate is helpful, but it is also critical to investigate how a changing climate could affect storm

behavior and precipitation in the future. This subject is even less well-understood than the storm dynamics leading to flooding in the MRB region in the present climate. Previous studies have explored aspects of future floods in the MRB using hydrologic models and regional and global climate models (RCMs and GCMs, respectively). Using a GCM to drive a global river routing model, Hirabayashi et al. (2013) showed that the MRB will have less frequent future floods, but there was a large spread in the frequency of the 100 year-return period from 5–3000 years. Similarly, Van der Wiel et al. (2018) found little to no decreasing trend in the occurrence of flood events along the lower Mississippi River at various return intervals in a future climate using a GCM coupled to a river routing model. Interestingly, the decreasing frequency of future flood events is despite a projected increase in future precipitation, which Van der Wiel et al. (2018) attributes to decreases in future snowmelt being more important than non-frozen precipitation changes. In contrast to Hirabayashi et al. (2013) and Van der Wiel et al. (2018), Jha et al. (2004) found a 50% projected increase in streamflow in the upper MRB in a future climate. Jha et al. (2004) used a regional climate model to drive a hydrologic model and Soil and Water Assessment Tool (SWAT), which at 50 km horizontal resolution, is higher resolution than the GCMs used in Hirabayashi et al. (2013) and Van der Wiel et al. (2018). The increased future streamflow in the upper MRB was attributed to the 51% increase in runoff due to more intense extreme precipitation in a future climate (Van der Wiel et al., 2018). This is corroborated by Frans et al. (2013), who used a hydrologic model in the upper MRB to show that increased precipitation from 1918–2007 was the main reason for increased runoff and streamflow, rather than other factors like changes in land-use.

Despite the conflicting results of the prior studies, none use high-resolution convection-permitting models that more accurately simulate precipitation and storm characteristics by explicitly resolving convection that obviates the need for a convective parameterization. Given the complex storm dynamics and morphology that lead to the wide variety of storms producing floods, it is necessary to use such high-resolution simulations to understand future changes in flood-producing storms in the MRB. Recently, studies have used high-resolution convection-permitting climate simulations over the CONUS to examine changes in precipitation in a future climate. Such simula-

tions more accurately depict the diurnal cycle, structure, and intensity of precipitation (especially convectively-driven) on regional scales compared to coarser GCMs (Kendon et al., 2017, 2012; Prein et al., 2017b; K. L. Rasmussen et al., 2017). These simulations show that in a future warmer climate, precipitation in convective storms (Prein et al., 2017b, 2017c; K. L. Rasmussen et al., 2017), heavy rainfall events (Dai et al., 2017; Prein et al., 2017a), and hurricanes (Gutmann et al., 2018) will become more intense. In 584 flash flood-producing storms specifically, work in Chapter 4 used high-resolution climate simulations to show that the accumulated flash-flood rainfall over the whole CONUS increases by 21%, on average, in a future warmer climate. Notably, the greatest future increase in the rainfall per storm was located in the MRB, where rainfall increased up to 50 mm per storm.

Motivated by the results from Chapter 4, the goal of the present study is to understand the detailed changes in precipitation characteristics and storm dynamics in flash flood-producing storms in the MRB in a future warmer climate. Specifically, the role that flash flood-producing storm intensity changes have on modulating future precipitation changes will be examined by separating strongly and weakly vertically forced precipitating systems. This examination may help better prepare the flood-prone region of the MRB for the impacts of climate change on flash flood-producing storms of varying intensities. Additionally, understanding how storm dynamics in flood-producing storms may change and modulate future precipitation behavior in a warmer climate may provide a greater understanding of how convection might change in a future warmer climate in general.

6.2 Data and Methods

6.2.1 *Convection-permitting simulations*

High-resolution convection-permitting simulations run by scientists at the National Center for Atmospheric Research (NCAR) are utilized to analyze flash floods in the Mississippi River Basin (MRB) in a current and future climate. Though Liu et al. (2017) describes these simulations in detail, here, a brief overview of the simulations is discussed. The simulations were run using the Weather Research and Forecasting (WRF) model V3.4.1 over a 1360 x 1016 grid point domain

covering North America, centered on the CONUS. Due to the domain covered, these simulations will hereafter be referred to as the WRF-CONUS simulations. The horizontal resolution is 4-km and the vertical resolution is comprised of 51 levels up to 50 hPa, with the highest resolution in the boundary layer. The parameterization schemes used in the simulations include the Thompson aerosol-aware microphysics (Thompson & Eidhammer, 2014), the Yonsei University (YSU) planetary boundary scheme (Hong et al., 2006), the rapid radiative transfer model (RRTMG) (Iacono et al., 2008), and the Noah-MP land-surface model (Niu et al., 2011) which was specifically improved for these simulations. On horizontal scales greater than 2,000 km above the boundary layer, spectral nudging was applied in order to avoid long-term climate drift (Feser et al., 2011) and to minimize deviations from the forcing data. However, on horizontal scales less than 2,000 km and within the boundary level, the flow was allowed to freely evolve, thus enabling changes in sub-synoptic scale weather to occur.

The WRF-CONUS simulations were comprised of two sets of simulations—one of the current climate and the other representing the future climate. The current climate simulations (CTRL) were forced with ERA-Interim (ERA-I) reanalysis data every 6 h over a continuous 13-year period from 2000–2013. The future simulations were also forced every 6 h by ERA-I over the same 13-year period, except a “pseudo-global warming” (PGW) signal was added to represent a future warmer climate, as given by the following:

$$WRF_{input} = ERA - Interim + \Delta CMIP5_{RCP8.5} \quad (6.3)$$

where $\Delta CMIP5_{RCP8.5}$ is the climate delta signal, which is the 95-year multi-model ensemble-mean monthly change in CMIP5 under the RCP8.5 emission scenario:

$$\Delta CMIP5_{RCP8.5} = CMIP5_{2071-2100} - CMIP5_{1976-2005} \quad (6.4)$$

The perturbed fields in the PGW simulations include horizontal wind, geopotential, temperature, specific humidity, sea surface temperature, soil temperature, sea level pressure, and sea ice.

Over the CONUS, this PGW approach results in a +3–6° C warming and increase in water vapor mixing ratio of ~20–40%, consistent with the Clausius-Clapeyron theory (Liu et al., 2017; Trenberth et al., 2003). This PGW approach has been similarly utilized in future regional climate change studies all over the world (Ban et al., 2015; Dai et al., 2017; Gutmann et al., 2018; Liu et al., 2017; Prein et al., 2015, 2017b, 2017c, 2017a; K. L. Rasmussen et al., 2017; R. Rasmussen et al., 2014, 2011; Schär et al., 1996), including case studies of floods in a future climate (Lackmann, 2013; Mahoney et al., 2018).

The Liu et al. (2017) simulations are particularly well-suited to study changes to flood-producing storms in a future climate over the CONUS. In the CTRL simulations, precipitation totals over the mountainous West outperform 25 other gridded precipitation datasets and show the best precipitation variability compared to uncorrected datasets (Beck et al., 2019). Results from Chapter 4 also showed that the CTRL precipitation compares well to that observed by the Stage-IV precipitation dataset (Lin & Mitchell, 2005) within 584 of the most intense historical flash flood-producing storms over the CONUS. A structural similarity index (SSIM; Wang et al., 2004) quantified the structural differences in rainfall accumulation within these flash flood-producing storms between Stage-IV and CTRL, as well as CTRL and PGW (see Chapter 4). The mean SSIM between Stage-IV and CTRL CONUS flash flood-producing storms was 0.88, and between CTRL and PGW the mean SSIM was 0.89. A SSIM value of 1 indicates exact similarity, so mean values of 0.88 and 0.89 between Stage-IV and CTRL as well as CTRL and PGW simulations indicate that rainfall accumulation structure and amount is similar within the same floods, both compared to observations and simulations in a future, warmer climate. The adequate representation of rainfall in both CTRL and PGW simulations is likely due to the spectral nudging used in the simulations, which reproduces the synoptic environment associated with floods in the current and future climate, as shown in Chapter 4. Reproducing the synoptic environment is particularly important in flash floods, as they tend to be associated with specific synoptic patterns as Maddox et al. (1980, 1979) highlighted. The only major difference between the CTRL and PGW simulations of flash floods is increased moisture in the PGW simulations, which is expected due to warmer temper-

atures. Thus, there is confidence that the WRF-CONUS simulations adequately represent flood rainfall in both the current and future climate under similar future synoptic conditions.

However, the WRF-CONUS simulations cannot explore all aspects of a future climate. Due to their high-resolution and the computational constraint this poses, uncertainty from a generation of multi-member ensembles cannot be assessed, unlike some GCMs (K. L. Rasmussen et al., 2017). Such a limitation was mitigated in part by taking the mean of a 19-member ensemble from the CMIP5 simulations used to force the PGW simulations, rather than use a single model run as in (R. Rasmussen et al., 2014, 2011). Additionally, while the use of spectral nudging in the WRF-CONUS simulations is beneficial for reproducing specific weather events, it does not allow for substantial future changes in large-scale synoptic dynamics. This large-scale dynamical change is more uncertain than the thermodynamic change in a future climate, which is why the WRF-CONUS simulations do not attempt to simulate this (Liu et al., 2017). Instead, the primary focus and utility of the WRF-CONUS simulations is to understand how today's weather would change in a warmer, moister future environment. Therefore, these simulations are well suited to understand how historical flash flood-producing storms will change in a warmer, moister climate in the MRB.

6.2.2 *Flash flood cases*

Historical flash flood-producing storms in the MRB are identified based on the Chapter 2 climatology of flood-producing storms over the CONUS from 2002–2013. This climatology merges National Center for Environmental Information (NCEI) storm reports with flooded stream gauges (Shen et al., 2017) and Stage-IV precipitation data (Lin & Mitchell, 2005) to analyze the rainfall characteristics associated with flood-producing storms that had a notable hydrologic response. Stage-IV precipitation is analyzed over a $\pm 5^\circ$ latitude/longitude domain from the flood centroid over the whole duration of the flood (plus a buffer of several hours). To isolate the likely flood-contributing rainfall, only the largest contiguous object with rainfall accumulations that met or exceeded the 75th percentile is utilized for each flood.

Using the above methodology, Chapter 2 identified 3436 flash flood-producing storms (including the hybrid category of floods) over the CONUS. Any flash flood report that occurred in states directly along the Mississippi River—Minnesota, Wisconsin, Iowa, Illinois, Missouri, Kentucky, Tennessee, Arkansas, Mississippi, and Louisiana—are utilized in the current study. However, flash flood rainfall associated with the flood reports sometimes extends into bordering states, which are also included in the analysis. Not including the entire MRB in the present study is due to the different character of flood-producing storms, especially in the western part of the basin (i.e., the Missouri River Basin), in which floods generated by rain-on-snow/snowmelt comprise a large portion of floods (Chapter 2). Based on these criteria, 1182 flash flood-producing storms in the MRB are identified (Figure 6.1). These flash floods are well distributed in the MRB, occurring both in the northern and southern portion of the basin. They mainly occur in the warm-season from April–July (Figure 6.2), consistent with previous work, and are thus likely associated with convective storms, like MCSs (Maddox et al., 1979; Schumacher & Johnson, 2006).

To ensure that only cases well-represented in the WRF-CONUS simulations are utilized, flash floods in which the rainfall difference between Stage-IV and CTRL exceeded 30% are excluded. This results in 484 flash flood-producing storms in the MRB in which CTRL and PGW rainfall differences are examined. Prior work in Chapter 4 included many of these flash flood cases in a study of flash flood-producing storms over the entire CONUS and showed that the SSIM of rainfall between Stage-IV and CTRL and CTRL and PGW was high. Therefore, using the same time and location of flood rainfall as the observations results in well-represented flash flood-producing storms in the MRB in both the CTRL and PGW simulations. However, while the flash flood-producing storm rainfall compares well between CTRL and PGW simulations and it is likely this rainfall will result in a flood in the future, it cannot be said with certainty, as future changes in land-use, soil moisture content, and streamflow were not examined and could influence the occurrence of a flash flood in the future. Such a caveat is important to consider and could only be specifically addressed by coupling the simulations with a more detailed hydrologic model, which will occur in future work.

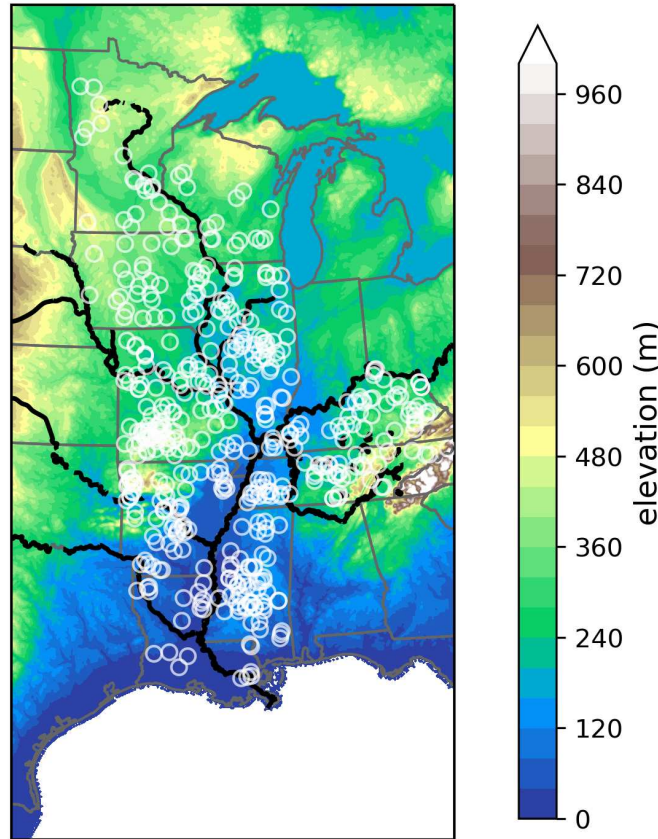


Figure 6.1: Location of 484 flash flood-producing storms (white circles) in the Mississippi River Basin from 2002–2013 identified by Chapter 2 from a combination of NCEI storm reports, flooded stream gauges from Shen et al. (2017), and Stage-IV precipitation data. The Mississippi River and its major tributaries are indicated by the thick black lines, while shading shows elevation.

6.2.3 Identification of tropical cyclone-related floods

A non-negligible source of flooding in the MRB is due to land-falling tropical cyclones (TCs), especially in the lower MRB near the Gulf of Mexico (Ashley & Ashley, 2008b; Schumacher & Johnson, 2006). Therefore, among the 484 flash floods included in this study, all are examined to see if a TC contributed to the flood. Note that the Chapter 2 climatology from which the flash floods in this study are based excludes coastal flood reports due to the non-meteorological factors that could contribute to those flood types (i.e., high-tide, on-shore wind, etc.). The Chapter 2 dataset also excludes tropical cyclone reports, since those were not directly associated with floods and could be impactful due to high wind and not purely heavy rainfall and flooding. Thus, the TC influence is only considered in respect to flash floods.

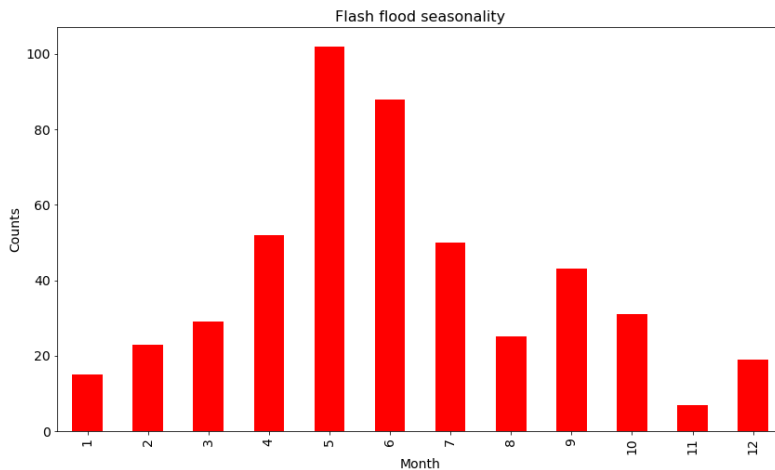


Figure 6.2: The seasonality of flash flood-producing storms shown in Figure 6.1.

The Extended Best Track dataset, which contains 6 hourly data of Atlantic TC pressure, winds, and location coordinates (Demuth et al., 2006), is utilized to identify floods with a TC influence. Specifically, any flood in which the 34 kt wind radii of a TC overlaps with the flood domain ($\pm 5^\circ$ latitude/longitude) and occurs within 24 h of the TC entering the flood domain is classified as having a TC influence. An example of this identification is shown in Figure 6.3, which shows Hurricane Katrina’s 34 kt wind radii squarely in the flood domain of a particular flash flood. Using these criteria, 25 MRB flash floods are associated with 11 unique TCs—Isidore (2002), Bill (2003), Ivan (2004), Katrina (2005), Rita (2005), Humberto (2007), Gustav (2008), Ike (2008), Lee (2011), Isaac (2012), and Andrea (2013). However, after a manual inspection of the overlap between the 34 kt wind radii and the flood domain, three TCs (Ike, Lee, and Andrea) are removed, due to barely being located in the flood domain. This leaves 19 MRB flash floods associated with 8 unique TCs (Table 6.1), with a majority of the flash floods associated with Hurricane Gustav (2008), followed by Isidore (2003), and Bill (2003).

To ensure that the TCs were well-represented in the WRF-CONUS simulations, the 8 TCs in Table 6.1 are compared to observations and between CTRL and PGW simulations. The TC track and the minimum pressure from the Best Track dataset is plotted over the CTRL surface pressure and reflectivity to ensure that CTRL simulations produced a TC-looking structure at the right

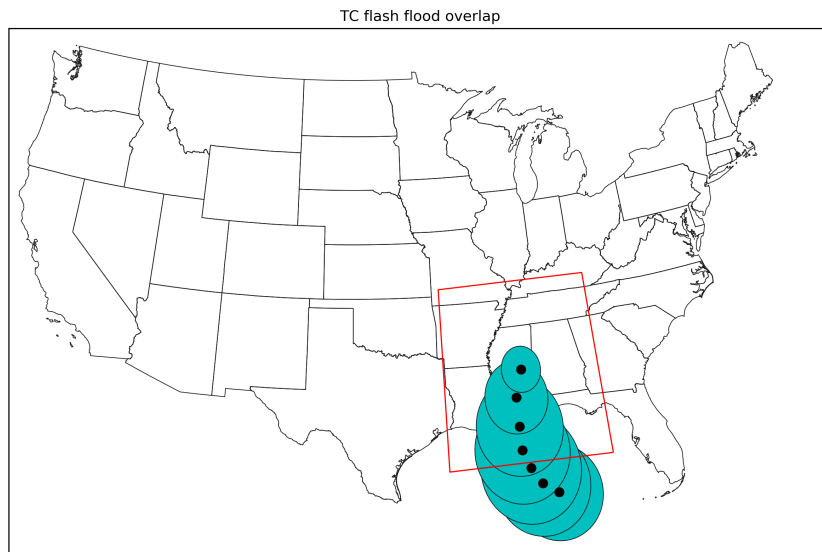


Figure 6.3: Example of the methodology used to classify a flash flood-producing storm as having a tropical storm influence. In this case, the domain of a flash flood-producing storm is outlined by the red box, while the 34-kt wind radii (storm center) of Hurricane Katrina (2005) are shown by the turquoise ellipses (black dots). Any flash flood-producing storm, such as this example, where the 34-kt wind radii intersects the flood domain <24 h prior to the flood was classified as having a tropical influence.

location and intensity. The CTRL reflectivity and pressure is then compared to that in the PGW simulations for each TC to ensure the TCs are captured in the future simulations. Most of the 8 TCs are well captured in the CTRL and PGW simulations, except for Bill (2003), Katrina (2005), and Humberto (2007), which were questionable (Table 1). However, when comparing the CTRL and PGW rainfall in the flash floods associated with these 3 TCs, they are similar enough to include in the analysis. These results are consistent with Gutmann et al. (2018) who used the WRF-CONUS simulations to specifically study future changes to 22 land falling TCs. They included all TCs in Table 6.1 except for Bill, Katrina, and Humberto, based on not being well represented in the simulations. However, the criteria in Gutmann et al. (2018) were stricter since they specifically focused on changes to TCs, whereas the present study allows some leeway in the representation of TCs since the main focus is on flooding. In general, these 8 TCs are adequately represented in the

Table 6.1: Names and years of hurricanes that were associated with flash flood events in the Mississippi River Basin from the Chapter 2 climatology. The number of unique flood events associated with the hurricane is shown, as well as an indication if the CTRL simulations of the hurricane compared well to both observations from the Extended Best Track dataset and PGW simulations.

Hurricane name	Year	# of flood episodes	Well -simulated?
Isidore	2002	3	yes
Bill	2003	3	no
Ivan	2004	1	yes
Katrina	2005	1	yes
Rita	2005	1	yes
Humberto	2007	1	ok
Gustav	2008	7	yes
Isaac	2012	2	yes

WRF-CONUS simulations, especially in regard to the flash flood rainfall associated with the TCs, which is the main interest of the study.

6.2.4 *Categorization of flash flood convective strength*

To further understand changes in flash flood-producing storms in the MRB in a future climate, storms were categorized by convective strength. This was motivated by the “ingredients-based approach” of forecasting flash floods by (Doswell et al., 1996). Recall, that among other factors being equal, stronger vertical velocity results in heavier rainfall (Eqn.6.1-6.2). This led to the hypothesis that flash flood-producing storms in the MRB, which are largely convective in nature (Figure 6.2), will produce different rainfall amounts in a future climate based on their convective strength. In this case, convective strength is defined by the average vertical velocity (\bar{w}) over a flash flood-producing storm’s lifetime and heavy rainfall area (see Section 6.2.2) in CTRL simulations. Vertical velocity was averaged over the entire storm’s lifetime, like \bar{R} in 6.1, in order to quantify the overall convective strength of the storm. This provides just one metric for categorizing the convective strength of flash flood-producing storms, and thus one aspect of quantifying the role of storm dynamics in modulating future changes in rainfall. However, it is recognized that there are

other dynamical metrics that are related to convective strength and precipitation potential, such as low-level vertical wind shear (Nielsen & Schumacher, 2018).

After calculating \bar{w} in the 484 flash flood-producing storms in the MRB, three different \bar{w} categories are created based on percentiles of the \bar{w} distribution in the CTRL simulations. The weak \bar{w} flash floods include 125 flash floods below the 25th percentile (0.03 m s^{-1}) of \bar{w} (Fig. 4), moderate includes 224 flash floods between the 25th–75th percentile ($0.03\text{--}0.06 \text{ m s}^{-1}$), and strong \bar{w} flash floods are the 135 floods with \bar{w} over the 75th percentile (0.06 m s^{-1}). Note that the relatively low values of \bar{w} are due to spatial and temporal averaging.

Weak flash flood-producing storms have a summertime maximum, smaller updraft and downdraft areas, a smaller area of heavy rainfall, and higher maximum instantaneous rain rates in both the CTRL and PGW simulations. These general characteristics imply that weakly vertically forced flash flood-producing storms are likely isolated summertime convective systems, though a full radar analysis would be needed to confirm this result. Strong flash flood-producing storms display a springtime maximum, larger updraft and downdraft areas, a larger area of heavy rainfall, and lower maximum instantaneous rain rates in the CTRL and PGW simulations compared to weak and moderate storms, though moderate storm characteristics are more similar to strong storms. Additionally, moderate storms include 10 out of 19 floods associated with TCs, while 8 out of 19 strong flash floods are associated with TCs. In general, these storm characteristics suggest that moderately and strongly vertically forced flash flood-producing storms are due to larger, more organized convection. While a more detailed analysis of the relationship between future changes in vertical velocity and rainfall in storms is needed, examining the broad changes within the heavy rainfall region of flash flood-producing storms provides a foundation for understanding these changes.

Using these categories of flash flood-producing storm intensity, future changes in rainfall are addressed to understand how different storm dynamics might change in a future climate and how this plays a role in modulating future changes in rainfall, which has not been examined before. Such an examination is motivated by future increases in rainfall exceeding the theoretical Clausius-Clapeyron rate of increase of $7\% \text{ K}^{-1}$ (Trenberth et al., 2003), which (Trenberth, 1999) hypoth-

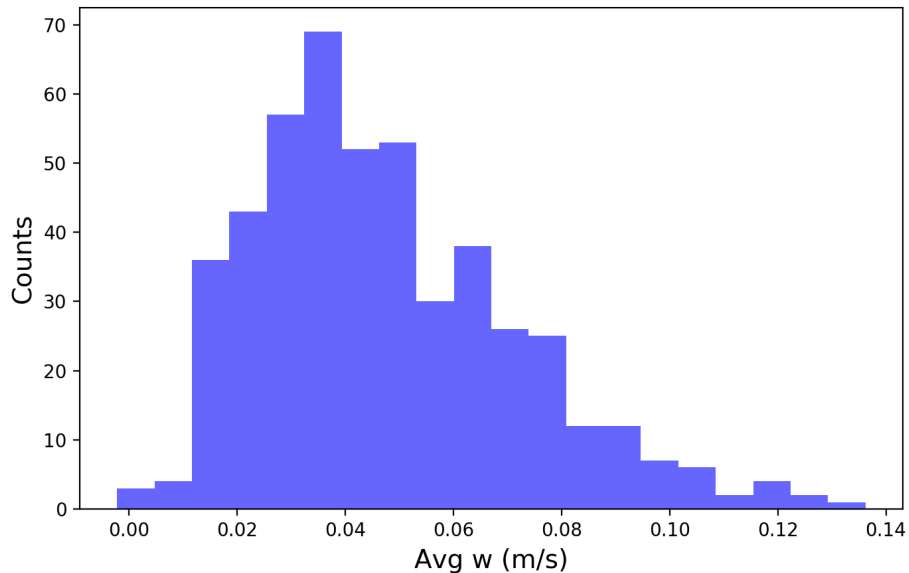


Figure 6.4: Distribution of the spatially and temporally averaged vertical velocity (w) within the heavy rainfall region of flash flood-producing storms in the Mississippi River Basin. Weakly forced flash flood producing storms have their average $w < 0.03 \text{ m s}^{-1}$, moderately forced $>0.03 \text{ m s}^{-1}$ and $<0.06 \text{ m s}^{-1}$, and strongly forced storms $>0.06 \text{ m s}^{-1}$.

esized could be possible in intense convective storms with additional latent heat release. An observed increase in hourly maximum rainrates above the Clausius-Clapeyron rate of increase in some flash flood-producing storms over the CONUS in a future warmer climate is seen in Chapter 4. The reason for this increase and dependence on convective strength thus warrants further investigation.

6.3 Results

6.3.1 *Future changes in all flash flood-producing storms*

In a future climate, the location of rainfall associated with flash flood-producing storms in the MRB does not change noticeably (Figure 6.5). The flash flood rainfall is slightly more concentrated in Missouri and Arkansas in the PGW simulations, but over most of the basin, there is no obvious change. Such a result is likely due the similar synoptic conditions in the PGW simulations, which results in similar flash flood-producing storms in the future in terms of duration, location, and

rainfall structure as mentioned in Section 6.2.2. However, changes in rainfall characteristics do occur in the MRB flash flood-producing storms in a future climate, due to the warmer and moister environment.

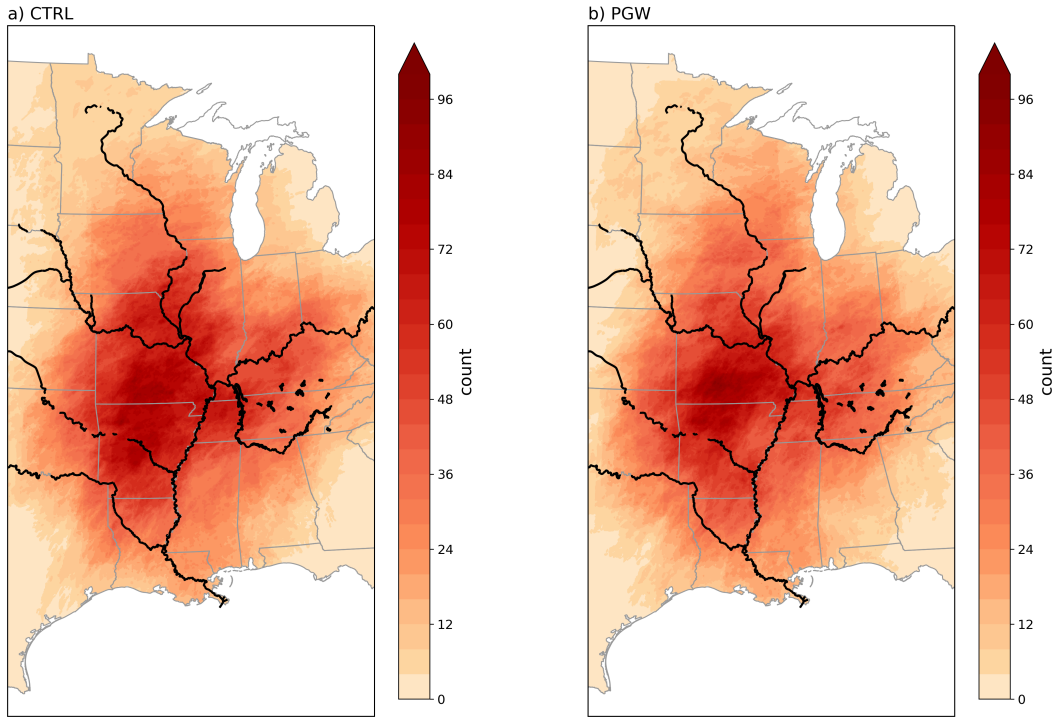


Figure 6.5: Distribution of the occurrence of flash flood-producing storm precipitation in the a) CTRL simulations and b) the PGW simulations.

The amount of rainfall per storm increases over most of the MRB, especially in the lower part of the basin near the Gulf of Mexico. Here, flash flood rainfall increases up to 50 mm per storm in the PGW simulations (Figure 6.6). This result is consistent with large increases in future precipitable water amounts in the Gulf of Mexico (K. L. Rasmussen et al., 2017). As will be shown later, some of this increased rainfall in the lower MRB is attributable to TCs. Elsewhere, flash flood rainfall increases exceed 20 mm per storm, though areas of slight decrease are observed. Some of these decreases are due to less rainfall from flash floods in a future climate, while another contribution is due to slight shifts in the heavy rainfall area associated with flash floods in the PGW simulations.

Overall, the dominant signal is increased flash flood rainfall, which increases by 16.6% ($5.7\% \text{ K}^{-1}$ of warming) in the future (Table 6.2).

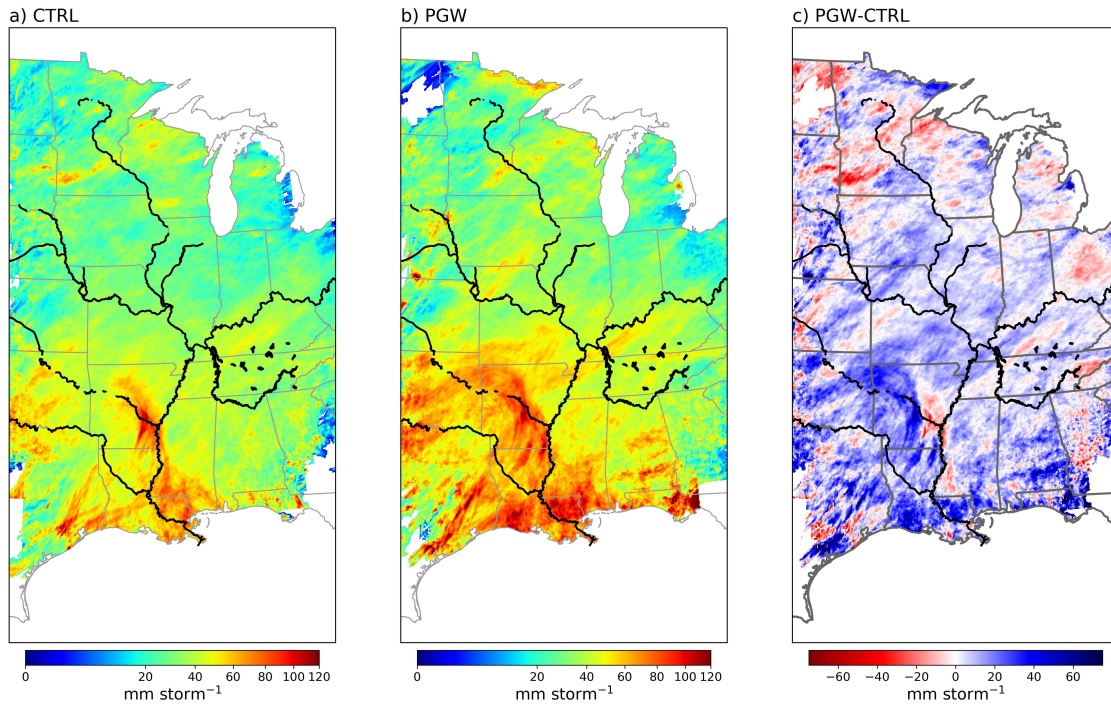


Figure 6.6: Rainfall per flash flood-producing storm (mm storm^{-1}) in the a) CTRL simulations, b) PGW simulations, and c) PGW-CTRL difference, where blue (red) indicates a future increase (decrease) in mm storm^{-1} .

Consistent with future increased flash flood rainfall is an increase in flash flood runoff, which increases by 31.8% in the PGW simulations (Table 6.2). These increases generally follow the spatial patterns of increased future flash flood rainfall, with the greatest future increase in the lower MRB where future runoff increases up to 40 mm per storm (Figure 6.7). Similarly, the locations of future decreased flash flood rainfall, such as western Wisconsin and central Minnesota, also exhibit decreased flash flood runoff. The average increase in future runoff exceeding the average increase in future rainfall in flash flood-producing storms implies more efficient runoff generation, as found in Chapter 4, which could be due to more intense rainfall rates that promote more runoff via the precipitation excess mechanism. Other factors, such as changes in evaporation and soil moisture could influence this result as well, but a detailed hydrologic model would be needed to

Table 6.2: Mean values of rainfall characteristics for all 484 flash flood-producing storms in the Mississippi River basin for CTRL and PGW simulations, the future difference (PGW-CTRL), future percent difference (% change), and future percent difference per degree of warming (% change K⁻¹). Also shown is the % change K⁻¹ for storms with the highest and lowest area-average rainfall accumulation (top 25% and lowest 25%, respectively; last two columns).

	CTRL	PGW	PGW-CTRL	% change	% change K ⁻¹	% change K ⁻¹ (top 25%)	% change K ⁻¹ (lower 25%)
Area averaged rainfall (mm)	34.1	40.2	6.1	16.6	5.7	6	1.4
Average rain rate (mm/h)	2.4	2.9	0.4	16.3	5.6	6	1.2
Max rain rate (mm/h)	72	86.7	14.7	26.9	8	9.6	6.3
Duration (h)	17.8	17.8	0	0	0	0	0
Area (km ²)	1.5*10 ⁵	1.4*10 ⁵	-9753	-4	0.22	-0.1	0.6
Runoff (mm)	1.7	2.2	0.5	31.8	—	—	—

investigate such changes. Generally, an increase in both flash flood-producing storm rainfall and runoff suggest more intense flood-producing storms and hydrologic response in a future climate over most of the MRB.

When separating out the flash flood rainfall contributed by TCs, most of the rainfall occurs in the lower MRB (Figure 6.8). The occurrence of the flash flood rainfall from TCs is similar in the CTRL and PGW simulations, except for slight shifts. This is particularly noticeable in the western shift of flash flood rainfall over Arkansas, which is due to the shift of Hurricane Gustav in the PGW simulations—the dominant TC signal associated with seven different flash floods (Table 6.1). This shift in Hurricane Gustav in the PGW simulations is also evident in the future change in mm storm⁻¹, with a dipole of increasing (decreasing) rainfall over western (eastern) Arkansas (Figure 6.9). However, the change in rainfall due to Gustav in the PGW simulations is not just a pure shift, as there is a 27.6% increase in flash flood rainfall associated with Gustav in the future (not shown), consistent with Gutmann et al.’s (2018) findings that that Gustav’s rain rate increased by 21 mm h⁻¹ in the future. An increase in future flash flood rainfall is also observed in all other

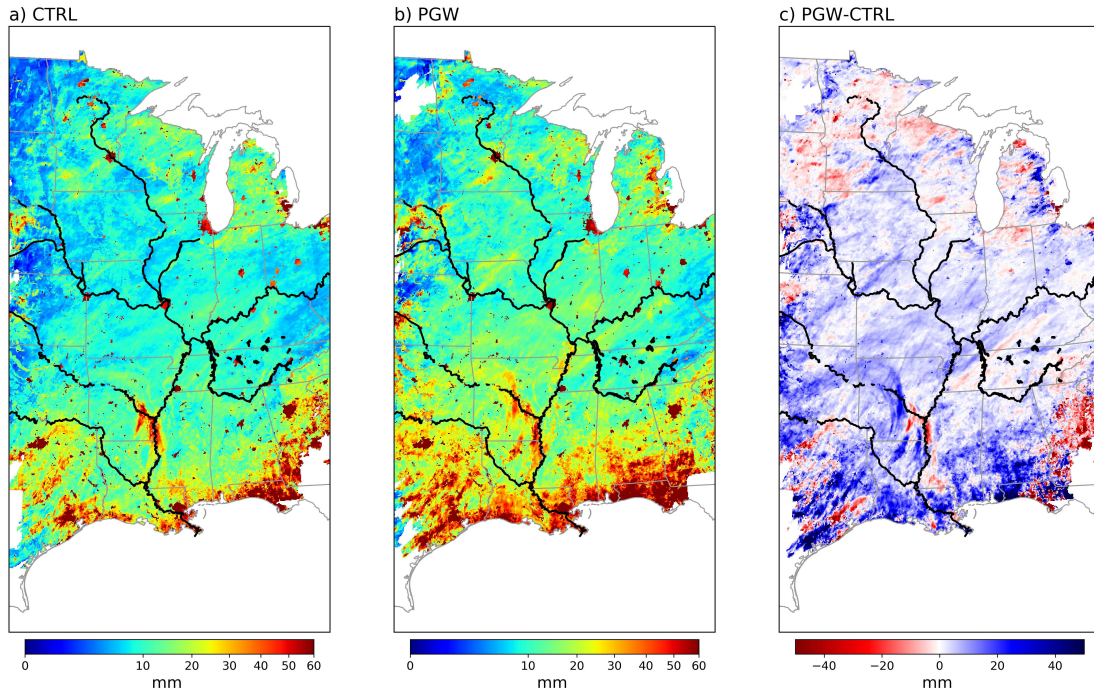


Figure 6.7: As in Figure 6.6, but for runoff per storm.

TCs, with area average rainfall increasing in the PGW simulations from 2.2%–36.8%. Thus, while Hurricane Gustav exhibits a large signal of both increased rainfall and shift in rainfall in the future in the MRB, even after removing Gustav, area-average rainfall in TCs still increases by 17.8% on average, suggesting this is a robust future change.

While this TC signal is evident in the signal of change for all flash floods in the MRB (Figure 6.6), particularly the rainfall produced by Gustav in Arkansas, the TC signal is dampened when averaged with all flash floods in the MRB. This suggests that other types of storms in the MRB dominate the contribution to flash flood rainfall, likely due to warm-season convection as suggested in Figure 6.2. Such a result is evident when comparing changes in future maximum hourly rain rates, which increase at a higher rate of 26.9% ($8.0\% \text{ K}^{-1}$) in all flash flood-producing storms in the MRB (Table 6.2) compared to the 18.9% ($7.2\% \text{ K}^{-1}$) increase in flash floods associated with TCs (Table 6.3). Maximum hourly rain rates increase at an even higher rate of $9.6\% \text{ K}^{-1}$ in the flash flood-producing storms with higher area-average rainfall (i.e., second to last column in Table 6.2). However, flash floods associated with TCs exhibit a greater future increase in area-

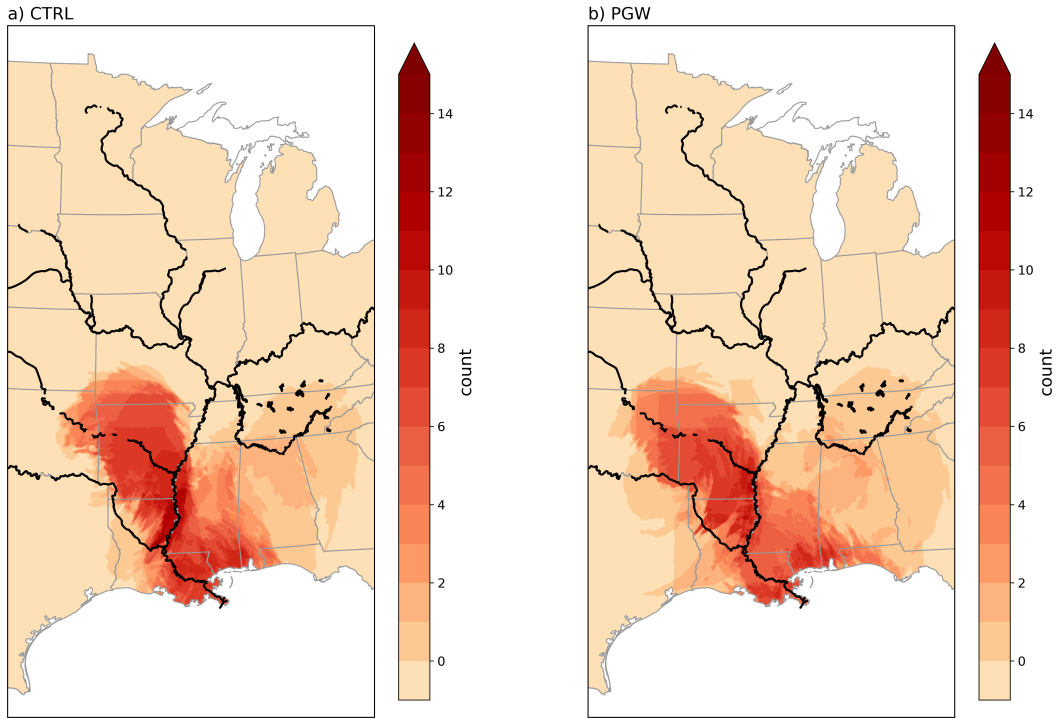


Figure 6.8: As in Figure 6.5, but only for flash flood-producing storms with a tropical storm influence.

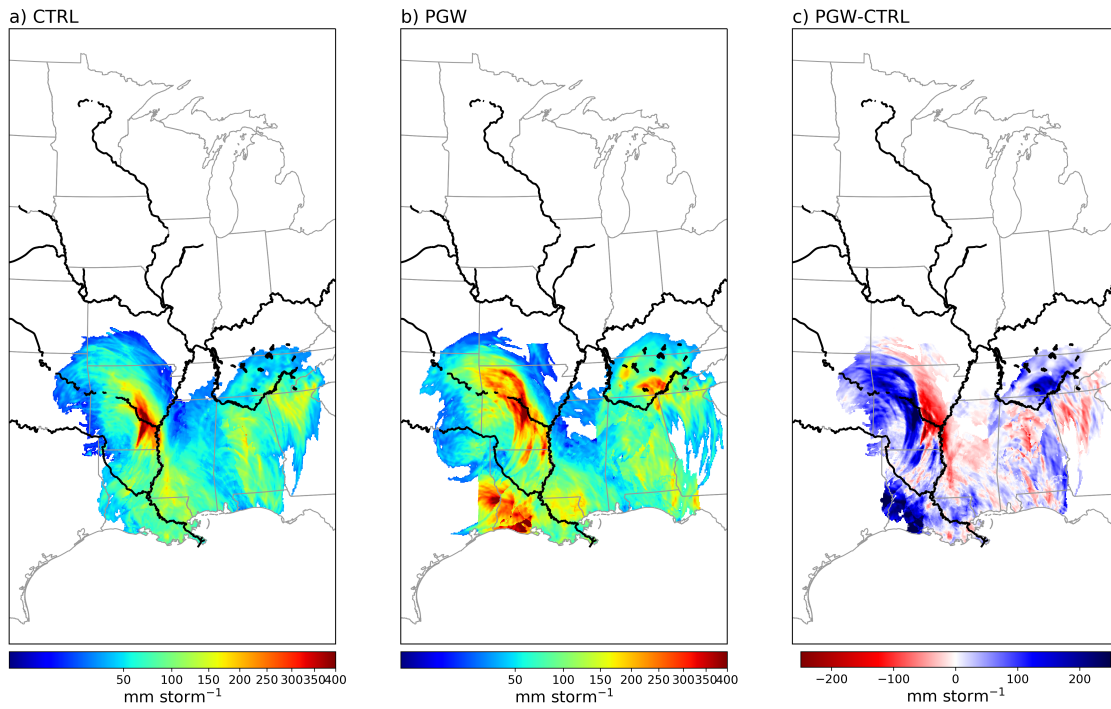


Figure 6.9: As in Figure 6.6, but only for flash flood-producing storms with a tropical storm influence.

average rainfall of 27.4% (8.5% K⁻¹) compared to all flash flood-producing storms in the MRB that increase by 16.6% (5.7% K⁻¹). The different rate of change in rainfall characteristics between TC-related flash floods and all flash flood-producing storms in the MRB suggest that while the increase in TC-related flash flood area-average rainfall is larger and perhaps more robust in the future, changes in other flash flood-producing storms still dominant the spatial changes in flash flood rainfall (Figure 6.6) and intensify at greater rates than TC-related flash floods. This result suggests that different types of flash flood-producing storms, and likely, their intensity, play a role in influencing future changes in rainfall characteristics, as will be explored further in Section 6.3.2.

Table 6.3: As in Table 6.2, but only for flash flood-producing storms associated with the hurricanes listed in Table 6.1 (n=19).

	CTRL	PGW	PGW-CTRL	% change	% change K ⁻¹
Area averaged rainfall (mm)	78	99.4	21.4	27.4	8.5
Average rain rate (mm/h)	4.2	5.3	1.1	26.1	8.5
Max rain rate (mm/h)	114.3	135.9	21.6	18.9	7.2
Duration (h)	20.4	20.4	0	0	0
Area (km ²)	1.8*10 ⁵	1.8*10 ⁵	-1116	-0.6	0.75

Changes in flash flood rainfall area and duration were also examined, both of which showed little future change (Table 6.2). Flash flood rainfall area showed a 4% future decrease, with flash floods with the most (top 25%) area-averaged rainfall displaying a 0.1% future decrease and those with the least rainfall showing a 0.6% increase. Similarly, TC-related flash flood area only slightly decreased by 0.6% in the future, consistent with the findings from Gutmann et al. (2018) that future TC area showed little future change. The lack of duration change among all MRB flash flood-producing storms is partially due to the methodology, which examines floods over the same dates in the CTRL and PGW simulations. This a potential limitation of this study, but as previously

demonstrated, a lack of change in flash flood duration could also be due to the ability of the PGW simulations to reproduce a similar flash flood in the future.

6.3.2 Future changes in flash flood-producing storms by convective strength

Changes between CTRL and PGW simulations among the different \bar{w} categories of flash flood-producing storms show that the mean \bar{w} decreases in all categories in the future (Figure 6.10). Values of \bar{w} are lowest in the CTRL and PGW simulations in the weak storms and also exhibit the greatest percent future decrease of -33% (Table 6.4). Conversely, strong storms display the highest \bar{w} in both CTRL and PGW simulations with the least future decrease of -2.4% (Table 6.4), despite showing a larger range in future \bar{w} values. This large variability could be due to using the CTRL \bar{w} to define the vertical velocity category and comparing how storms in the CTRL-defined category change in the PGW simulations. Moderate storms have moderate \bar{w} values and a future decrease between weak and strong storms. Thus, the greatest (least) future decrease in \bar{w} is in weak (strong) flash flood-producing storms.

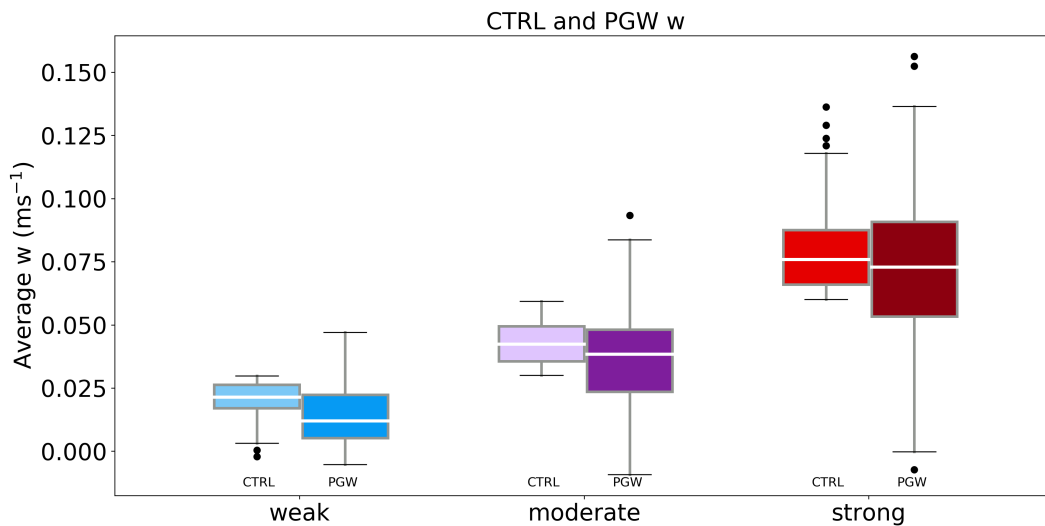


Figure 6.10: Boxplots of average vertical velocity (w) in weak (blue), moderate (purple), and strong (red) flash flood-producing storms. Boxes with lighter (darker) shades indicate storms in the CTRL (PGW) simulations.

Table 6.4: Percent future change (PGW–CTRL/CTRL*100) in storm characteristics among three different categories of average (temporal and spatial) vertical velocity (w) in flash flood-producing storms in the Mississippi River basin. Weak storms have average vertical velocities $<0.03 \text{ ms}^{-1}$, $0.03 \text{ ms}^{-1} < \text{moderate} < 0.06 \text{ ms}^{-1}$ and strong $>0.06 \text{ ms}^{-1}$. Values in parentheses show the future % change per degree of warming and bold numbers indicate the maximum value for each variable.

	Weak w % (% K^{-1})	Moderate w % (% K^{-1})	Strong w % (% K^{-1})
Area average rain	13 (3.9)	17.5 (4.5)	18.4 (5.8)
Volumetric rain	8.2 (3.9)	12.2 (3.8)	7.1 (2.6)
Max rain rate	22.5 (6.5)	25 (6.5)	29.1 (8.6)
Area	-6 (-1.3)	-2.8 (-0.7)	-4.9 (-1.2)
Average w	-33 (-6.2)	-11.4 (-2.8)	-2.4 (0.03)

Table 6.5: As in Table 6.4, except for changes in updraft and downdraft characteristics.

	Weak w % (% K^{-1})	Moderate w % (% K^{-1})	Strong w % (% K^{-1})
Maximum updraft (m s^{-1})	17.9 (3.3)	27.1 (7.4)	19.9 (6.5)
Average updraft (m s^{-1})	1.9 (0.6)	3.9 (1.0)	5.5 (1.3)
Average downdraft (m s^{-1})	3.7 (0.9)	4.0 (1.0)	4.5 (1.5)
Updraft area (km^2)	-1.1 (0.6)	-1.1 (1.0)	3.6 (1.3)
Downdraft area (km^2)	0.2 (0.9)	0.2 (1.0)	0.3 (1.4)

To explain future changes in the average \bar{w} updraft ($> 1 \text{ m s}^{-1}$) and downdraft ($< -1 \text{ m s}^{-1}$) characteristics are examined (Table 6.5). In a warmer climate, the maximum instantaneous updrafts increase in all categories of \bar{w} (Figure 6.11). In strong storms, maximum updrafts are the strongest in both the CTRL and PGW simulations at 25.5 m s^{-1} and 29.8 m s^{-1} , respectively. However, moderate storms exhibit the largest future increase of 27.1% in maximum updrafts in the future. The increase in maximum updrafts in these flash flood-producing storms is consistent with the projected increase in future CAPE in convective storms (Hoogewind et al., 2017; Prein et al., 2017c; K. L. Rasmussen et al., 2017), since CAPE is proportional to the theoretical maximum updraft velocity. Results from Prein et al. (2017c) support these results, finding that MCSs exhibit stronger maximum updrafts above 2 km in a future climate over the CONUS.

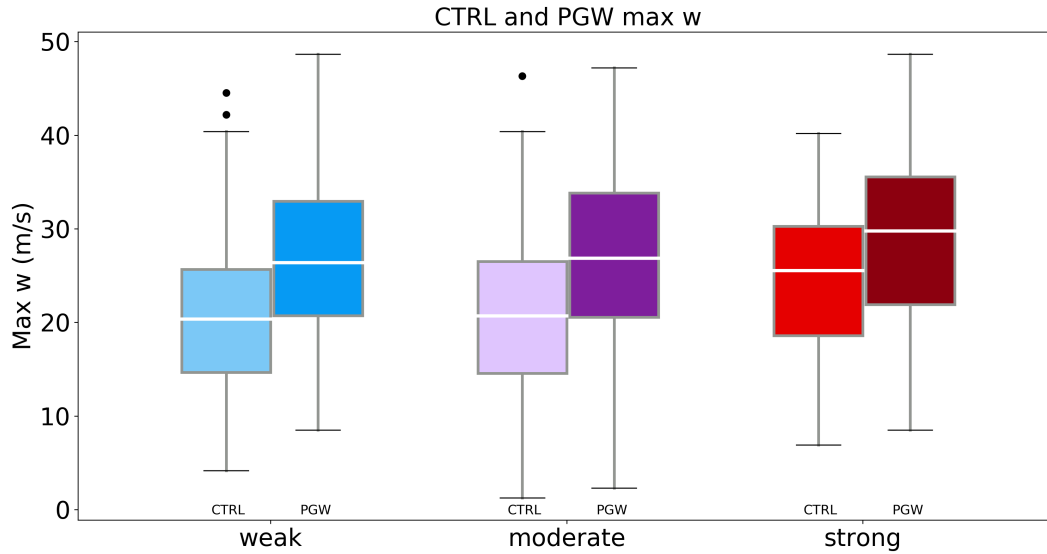


Figure 6.11: As in Figure 6.10, but for maximum instantaneous vertical velocity.

Changes in updrafts and downdrafts averaged over the duration of each flood-producing storm and the heavy rainfall region (the largest contiguous region with rainfall accumulations > 75th percentile) confirm that flash flood-producing storms could intensify in the future in the MRB (Figure 6.12). However, this intensification depends on the category of flash flood-producing storm. Average updraft magnitudes only increase by 1.9% in the future in weak flash flood-producing storms, while they increase by 5.5% in strong flash flood-producing storms (Table 6.5). It is possible that the larger increase in updraft magnitude in strong flash flood-producing storms is related to an increase in updraft area in the future, which increases by 3.6%, yet decreases by -1.1% in both weak and moderate flash flood-producing storms (Table 6.5). Both Prein et al. (2017c) and Trapp et al. (2019) similarly found an increase in future updraft area in MCSs and hail-producing storms, respectively, while Grabowski and Prein (2019) showed stronger updrafts in the future compared to the current climate. While the results from the present study are consistent with previous studies, changes in future updrafts within range of vertically forced flash flood-producing storms has not been documented.

Supporting the future increase in updraft magnitudes in flash flood-producing storms in the MRB are stronger downdrafts within these storms as well (Figure 6.12). Interestingly, weak, mod-

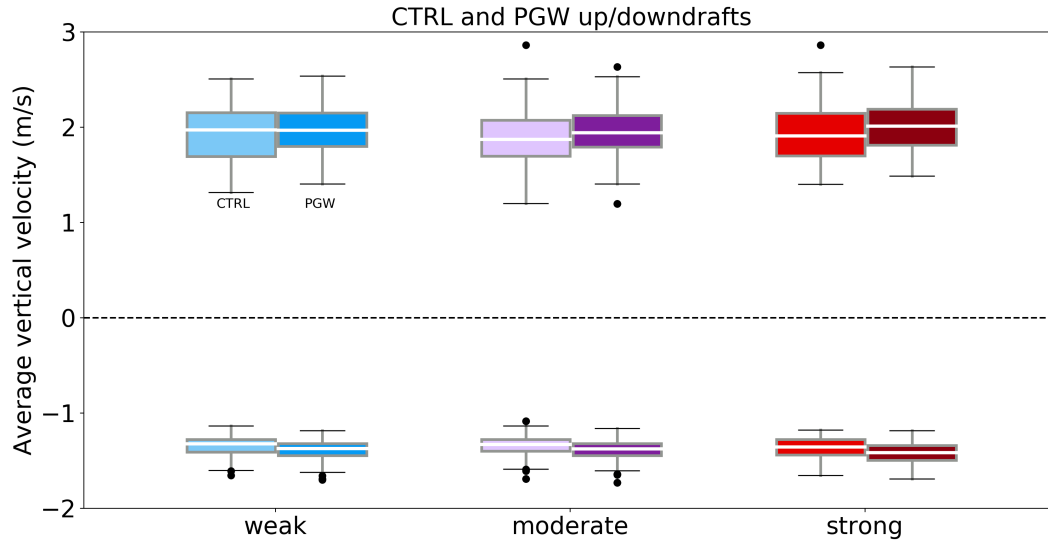


Figure 6.12: As in Figure 6.10, except for spatially and temporally averaged updrafts (defined as $w > 1 \text{ m s}^{-1}$, above the dashed line) and downdrafts ($w < -1 \text{ m s}^{-1}$, below the dashed line).

erate, and strong flash flood-producing storms display similar CTRL and PGW average downdrafts ranging from -1.33 m s^{-1} to -1.42 m s^{-1} , though downdraft magnitudes strengthen most in the future in strong flash flood-producing storms by 4.5% (Table 6.5). The change in downdraft area does not seem to play as much of a role in explaining the change in downdraft magnitude, as it increases only slightly from 0.2 to 0.3% in all categories of flash flood-producing storms (Table 6.5). This is in contrast to Prein et al. (2017c), who found a broadening of downdrafts among MCSs, though they support the finding of stronger downdrafts in a future climate. The strengthening of average downdrafts, average updrafts, and maximum updrafts in flash flood-producing storms, especially in strong storms, suggests more intense dynamics operating in a future, warmer climate.

Future rainfall characteristics also exhibit changes as a function of storm \bar{w} , with weak storms exhibiting the least area-average rainfall in the CTRL and PGW simulations (Figure 6.13) along with the lowest percent future increase of 13% and lowest scaling rate of $3.9\% \text{ K}^{-1}$ (Table 6.4). Strong flash flood-producing storms display the highest CTRL and PGW area-average rainfall and greatest future increase of 18.4 % ($5.8\% \text{ K}^{-1}$), likely due to their stronger vertical forcing (Figure 6.11–Figure 6.12)—an ingredient promoting heavy rainfall (Doswell et al., 1996; Eqn. 6.2). However, all flash flood-producing storms display an overall increase in future area-average rain-

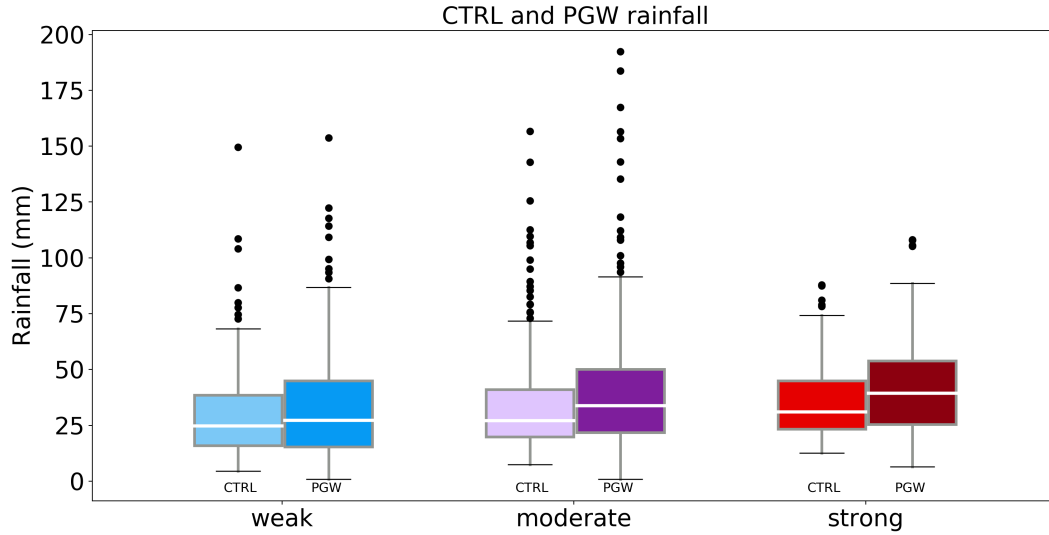


Figure 6.13: As in Figure 6.10, but for area-averaged rainfall.

fall, likely due to the more favorable thermodynamic environment in the PGW simulations that contains more moisture, which is another ingredient necessary to produce more rainfall (Doswell et al., 1996; Eqn. 6.2).

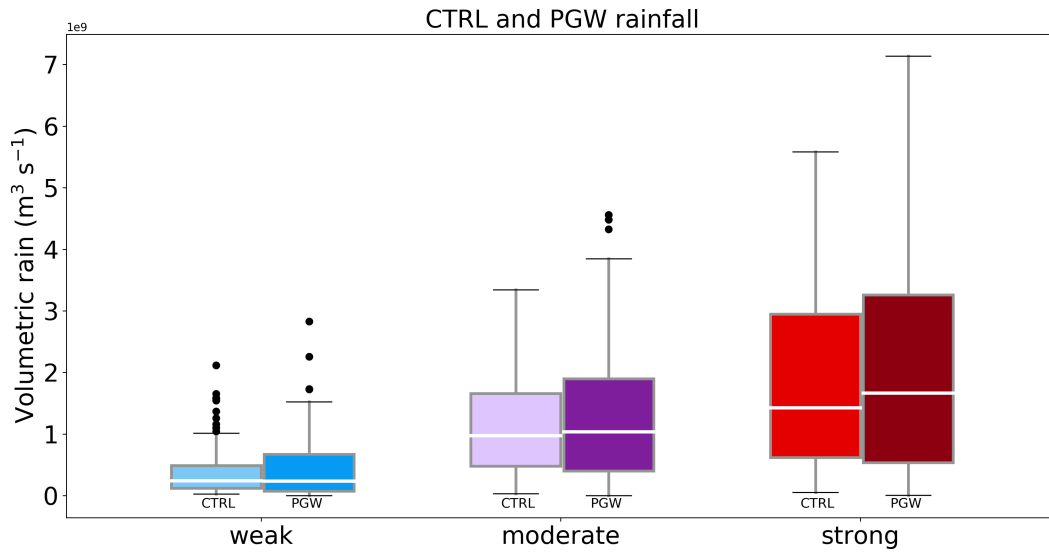


Figure 6.14: As in Figure 6.10, but for volumetric rainfall.

Changes in volumetric rainfall and area by \bar{w} category differ from future trends in \bar{w} and area-average rainfall. While strong storms have the largest volumetric rain in the CTRL and PGW

simulations, the greatest future increase of 12.2% occurs in moderate storms (Figure 6.14). Similar scaling rates in volumetric rainfall are observed in weak and moderate storms of $3.9\% \text{ K}^{-1}$ and $3.8\% \text{ K}^{-1}$, respectively, which is higher than the $2.6\% \text{ K}^{-1}$ increase in strong storms. The future changes in volumetric rainfall are likely due to changes in area, since volumetric rainfall, by definition, is the amount of total rainfall multiplied by area divided by the storm duration. Therefore, since area shows the least future decrease in moderate storms of -2.8% , this is likely the reason for greater increase in volumetric rainfall compared to weak and strong storms (Table 6.4). This is despite similar storm area in moderate and strong storms (not shown).

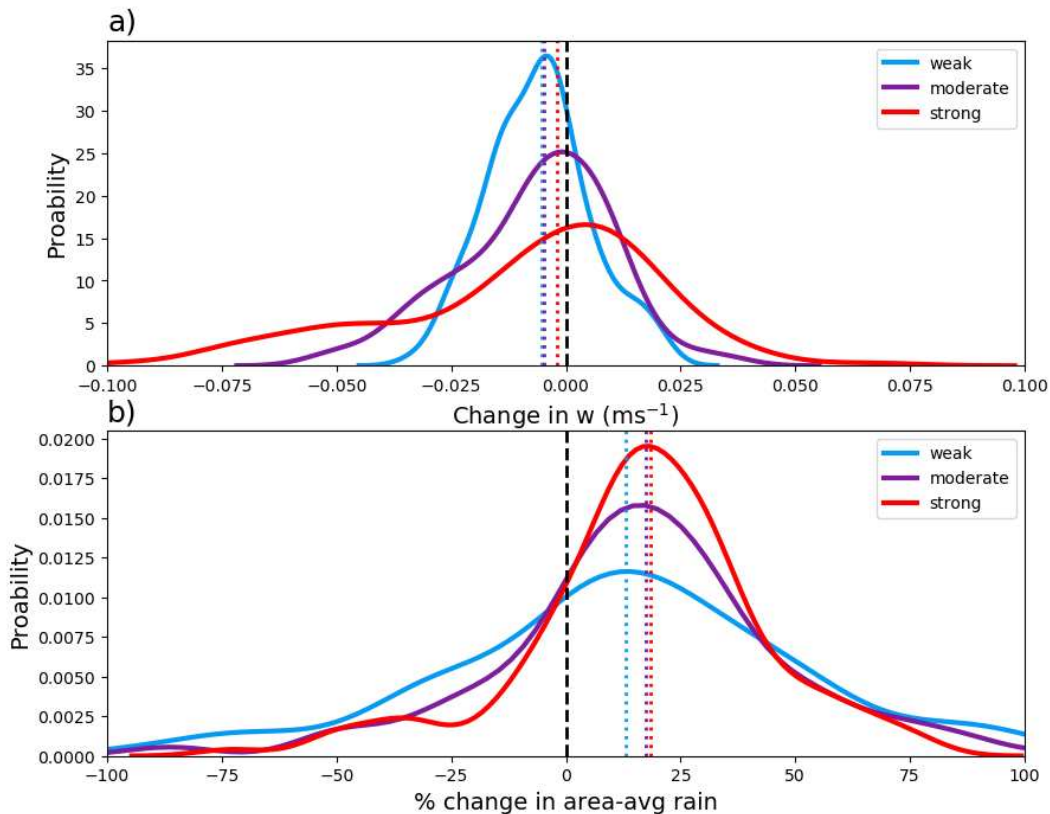


Figure 6.15: PDF of the future (PGW-CTRL) change in a) average vertical velocity (w ; m s^{-1}) and b) area-average rainfall (%) in weak (blue), moderate (purple), and strong (red) flash flood-producing storms. The dashed line at zero distinguishes a future increase/decrease in (w) and rain, with anything to the right of the zero line indicating a future increase. Colored dashed lines indicate the median of the distribution.

The future changes in \bar{w} and rainfall among the different \bar{w} categories of flash flood-producing storms are summarized in Figure 6.15. The future change in \bar{w} (m s^{-1}) and area-average rainfall

(%) is shown in terms of PDFs for each \bar{w} category, where positive values indicate a future increase in \bar{w} or rainfall. The weak storms display a narrow PDF of \bar{w} with a negative skew, and a median value (dashed line) below zero. This indicates that although the weak flash flood-producing storms do not experience much absolute change in future \bar{w} , the median shows a future decrease of 0.005 m s^{-1} . As shown in Figure 6.11–Figure 6.12 and Table 6.5 this is likely due to a greater future increase downdraft magnitude compared to updraft magnitude, and a decrease in updraft area. Strong storms, on the other hand, display a broad PDF, indicating both large changes in future \bar{w} ranging from $\pm 0.1 \text{ m s}^{-1}$, with a median decrease of 0.002 m s^{-1} . However, most of the distribution is centered around zero, likely due to stronger future downdrafts being balanced by stronger future updrafts. Moderate storms exhibit a PDF between values of the weak and strong storms, with a median decrease of 0.005 m s^{-1} . These distributions in future \bar{w} indicate that weak storms mostly experience a decrease in future \bar{w} , while strong storms experience little to a slight decrease in future \bar{w} . These overall changes in future vertical velocity are likely related to future increases in CAPE and CIN that suppress weak convection and promote more frequent strong convection in a future climate over the CONUS (Hoogewind et al., 2017; Prein et al., 2017c; K. L. Rasmussen et al., 2017) and globally (Chen et al., 2020).

Future changes in rainfall show an increase among all \bar{w} categories (Figure 6.15b), similar to results in Figure 6.13. A noticeable positive skew in future rainfall change is displayed by all \bar{w} categories, but strong storms exhibit the largest positive skew and median increase in future rainfall of 18.4%. Therefore, while future rainfall increases in all flash flood-producing storms in the MRB, it increases the most in strong flash flood-producing storms that exhibit the greatest future increase in updraft magnitude, updraft area, and downdraft magnitude that result in the least future decrease in \bar{w} . These results suggest that in a warmer and moister future climate, strong convective storms might dynamically intensify more than weak storms, which could lead to a thermodynamic feedback in which more latent heating occurs to produce more rainfall and higher rain rates above that predicted by Clausius-Clapeyron theory, as suggested by Trenberth (1999) and Trenberth et al. (2003). Such a finding has not been documented before within the context of

varying storm intensities, especially in flood-producing storms, where future changes in dynamics play a non-negligible role in modulating future rainfall behavior.

6.4 Conclusions

This study examines changes in 484 flash flood-producing storms in the MRB in a future climate using high-resolution convection-permitting simulations (Liu et al., 2017) that adequately reproduce the rainfall structure, timing, and location of historical flash flood events in CTRL and PGW simulations. While storms in the current climate are associated with flash floods and are likely associated with flash floods in the future due to increases in rainfall, this cannot be said with certainty, as future changes in soil moisture, land-use, and streamflow could all influence flood occurrence in the future. Thus, the focus of the study is on the storms producing the flash floods, rather than the floods themselves. The flash flood-producing storms in the MRB are mostly due to warm-season convection, but a small proportion (19/484) storms are associated with TCs. The change in future rainfall specifically in floods associated with TCs is separated from the rest of the flash floods, which mainly are confined to the lower MRB.

Flash flood-producing storms in a future climate display a widespread increase in area-average precipitation and runoff, with an average increase of 17% and 32%, respectively. Some of this increase is due to the future increase in flash flood rainfall associated with TCs, which increases at a rate of 27%—higher than the increase in all flash flood-producing storms in the MRB. The overall increase in flash flood rainfall associated with TCs is consistent with Gutmann et al. (2018) who showed that among 22 land-falling hurricanes, the main future change is the 24% projected increase in maximum rain rate. The future increase in flash flood rainfall associated with TCs is mainly due to contributions from Hurricane Gustav (2008), which is associated with 7 out of 19 flash floods. While future rainfall increased in Hurricane Gustav, the main signal is a westward shift in rainfall associated with the hurricane, leading to a dipole of future rainfall increase/decrease over Arkansas. This dipole is evident in the future rainfall change among all flash flood-producing storms, but the signal is diminished, suggesting that the predominant change

in flash flood-producing storm rainfall in the MRB comes from other types of flood-producing storms, like warm-season convection.

Given the convective nature of flash flood-producing storms in the MRB and work by Doswell et al. (1996) who showed that heavy rainfall depends on vertical velocity, the influence of vertical velocity on changes in future rainfall is examined. This is achieved by categorizing flash flood-producing storms as “weak”, “moderate”, or “strong” based on percentiles of spatially and temporally averaged vertical velocity (\bar{w}). While all flash flood-producing storms exhibit increased future area-average rainfall amounts likely due to a more favorable future thermodynamic environment, strong flash flood-producing storms ($\bar{w} > 0.06 \text{ ms}^{-1}$) display the greatest future increase, and weak storms ($\bar{w} < 0.03 \text{ ms}^{-1}$) the least. The strong flash flood-producing storms also exhibit the least decrease in future \bar{w} , decreasing slightly on average (-2.4%), associated with the greatest future increase in average updraft magnitude and updraft area to compensate stronger downdrafts. Weak storms, on the other hand, displayed the largest future decrease in \bar{w} of -33%, likely due to a greater future increase in downdrafts compared to updrafts and decrease in updraft area. These results qualitatively suggest that changes in storm dynamics (\bar{w}) might modulate future changes in rainfall amounts in convective storms in the MRB. However, more future work is necessary to explore these results, in order to more fully understand changes in storm dynamics and thermodynamics (i.e., changes in CAPE, CIN, vertical wind shear, etc.).

Overall, results suggest that flash flood-producing storms might be more intense in a future, warmer climate over the MRB—a flash flood hotspot in the CONUS (Saharia et al., 2017a). The increases in rainfall are due to TCs and warm-season convection, as well synoptically-driven systems like fronts, which were not specifically investigated in this study but are a source of heavy rainfall in the cool-season in this region (Kunkel et al., 2012). Stronger flash flood-producing storms in the MRB display a greater future increase in rainfall in this region and exhibit stronger updrafts and downdraft magnitudes in the future. Stronger storm dynamics in more intense convective storms associated with a greater increase in future rainfall amounts suggests a feedback between future changes in storm dynamics and thermodynamics. Such a relationship was hypothesized by

Trenberth (1999) and Trenberth et al. (2003) and could explain future changes in rainfall and rain rates that exceed that predicted by Clausius-Clapeyron theory, particularly in stronger convective storms. This link between future changes in storm dynamics and its relationship to rainfall changes has not been previously examined within the context of flash flood-producing storms of varying storm intensities. However, this contributes to an important understanding of the range in behavior a warmer, moister climate can have on future convective storm behavior within the context of destructive flood-producing storms. Such insight could improve the prediction and preparation of these climate change impacts to create more resilient communities.

Chapter 7

Conclusions

The objective of this dissertation is to understand precipitation and runoff characteristics within flood-producing storms in a current and future climate in the CONUS. This research fills the existing knowledge gap between projected future changes in fluvial floods worldwide (Hirabayashi et al., 2013) and changes in regional precipitation extremes (Ban et al., 2015; Kendon et al., 2014; Prein et al., 2017a) to test the claim that more intense future rainfall will lead to more intense future floods. An integrated hydrometeorological perspective is utilized to understand the characteristics of different types of flood-producing storms in the current climate over the CONUS and analyze how they might change in a future, warmer climate using high-resolution convection-permitting climate simulations from Liu et al. (2017). This research is the first of its kind to examine these hydrometeorological changes in hundreds of historical flood-producing storms over the CONUS in a future climate, thus providing a more comprehensive picture of possible future changes. Work from this dissertation shows that flood-producing storms display a wide range of precipitation characteristics in the current climate due to the variety of storm types causing these systems (Chapter 2). Despite these different characteristics, however, most flood-producing storms produce more simulated rainfall and runoff in a future, warmer climate in the CONUS (Chapter 4), particularly in flood hotspots in the Mississippi River Basin (Chapter 5) and California (Chapter 6). Specific findings from this dissertation are summarized here:

1. Flash flood-producing storms tend to occur in the warm-season in the Mississippi River Basin, with short duration and high-intensity rainfall.
2. Slow-rise flood-producing storms preferentially occur in the cool-season in the Ohio River Valley and Pacific Northwest, with long-duration and low-intensity rainfall.

3. Hybrid flood-producing storms, which have characteristics of both flash and slow-rise flood-producing storms, occur in the spring and summer concentrated in the central CONUS and Northeast, with moderate duration and intensity rainfall.
4. Sub-basin scale flood rainfall-streamflow correlations are spatially variable but tend to be strong and positive in areas of topographic relief and urban centers. The presence of dams muddles this relationship.
5. The average future change in the most intense 584 flash flood-producing storms from 2002–2013 over the CONUS show a 21% increase in precipitation and 50% increase in runoff.
 - (a) The greater future increase in runoff shows that runoff efficiency increases in flash flood-producing storms.
 - (b) It is hypothesized that the large increase in future runoff is related to the increase in maximum hourly rain rates that is consistent with Clausius-Clapeyron theory.
6. In 45 cool-season flood-producing storms associated with atmospheric rivers in California, future precipitation increases by 21–26% and SWE decreases by 32–90% (except at the highest elevations in the Sierra Nevada Mountains).
 - (a) Changes in precipitation and SWE lead to a future increase in runoff of 15–34%.
 - (b) The integrated water vapor transport associated with these storms increases from 250 $\text{kg m}^{-1} \text{s}^{-1}$ to 350 $\text{kg m}^{-1} \text{s}^{-1}$ in the future, suggesting more intense atmospheric river conditions that specifically lead to flooding.
7. In 484 flash flood-producing storms in the Mississippi River Basin, rainfall increases by 17% and runoff increases by 32%, on average, in a future, warmer climate.
 - (a) Some of the increase in rainfall is due to tropical cyclone-related flooding, but this is not the dominant signal, suggesting that other types of storms (like warm-season convection), are largely responsible for this change.

- (b) Storms with the strongest average vertical velocity in the current climate exhibit the greatest (least) future increase in rainfall (vertical velocity), despite nearly all storms exhibiting greater future rainfall.

This research advances the understanding of the hydrologic cycle in a future climate using convection-permitting simulations that capture the detailed characteristics of flood-producing storms, but more research is necessary to further improve this understanding. More hydrologic analysis is needed in addition to examining changes in runoff, in order to quantify the full scope of impacts from flood-producing storms. The dynamic and thermodynamic processes operating in individual flood-producing storms is also an avenue for future research, in order to better quantify how these processes might change and alter rainfall-production in a future climate. Specifically, the role of storm dynamics in modulating future rainfall is an important, unanswered question that will be explored using high-resolution WRF simulations. Results from flood-producing storms in the Mississippi River Basin and Trenberth (1999) suggests that this could provide critical insights for understanding storm behavior in a future climate.

Overall, this dissertation presents a more comprehensive picture of how the hydrologic cycle could change in a future warmer climate by identifying and analyzing hydrometeorological changes to flood-producing storms. While changes to mean (Allen & Ingram, 2002; Held & Soden, 2006) and extreme precipitation (Ban et al., 2015; Dai et al., 2017; Kendon et al., 2014; Prein et al., 2017a) have been extensively documented using GCMs and more recently, regional convection-permitting simulations, this work is novel by examining precipitation changes coupled with runoff changes in storms that specifically produce floods. Though previous work has examined flood-producing storms in a future climate using the PGW approach, this has been conducted from a case-study perspective (Lackmann, 2013; Mahoney et al., 2018), so this dissertation expands upon prior work to analyze future changes in hundreds of flood-producing storms over the CONUS. Such an analysis provides a more robust indication of the possible changes in a variety of flood-producing storms in a future, warmer climate. Results suggest that these flood-producing storms could intensify in the future, producing more precipitation that is more intense, resulting

in increased runoff. These results have major implications for water managers and policy-makers and should be considered when planning for the impacts of climate change in the CONUS in order to create more resilient communities.

References

- Adams, D. K., & Comrie, A. C. (1997). The north american monsoon. *Bulletin of the American Meteorological Society*, 78(10), 2197–2214.
- Allen, M. R., & Ingram, W. J. (2002). Constraints on future changes in climate and the hydrologic cycle. *Nature*, 419(6903), 228–232.
- Ashley, S. T., & Ashley, W. S. (2008a). Flood fatalities in the united states. *Journal of Applied Meteorology and Climatology*, 47(3), 805–818.
- Ashley, S. T., & Ashley, W. S. (2008b). The storm morphology of deadly flooding events in the united states. *International Journal of Climatology: A Journal of the Royal Meteorological Society*, 28(4), 493–503.
- Ban, N., Schmidli, J., & Schär, C. (2015). Heavy precipitation in a changing climate: Does short-term summer precipitation increase faster? *Geophysical Research Letters*, 42(4), 1165–1172.
- Barthold, F. E., Workoff, T. E., Cosgrove, B. A., Gourley, J. J., Novak, D. R., & Mahoney, K. M. (2015). Improving flash flood forecasts: The hmt-wpc flash flood and intense rainfall experiment. *Bulletin of the American Meteorological Society*, 96(11), 1859–1866.
- Beck, H. E., Pan, M., Roy, T., Weedon, G. P., Pappenberger, F., Van Dijk, A., . . . Wood, E. F. (2019). Daily evaluation of 26 precipitation datasets using stage-iv gauge-radar data for the conus. *Hydrol. Earth Syst. Sci*, 23, 207–224.
- Benner, P. A., & Sedell, J. R. (1997). Upper willamette river landscape: a historic perspective. *River quality: dynamics and restoration*, 23–47.
- Berghuijs, W. R., Woods, R. A., Hutton, C. J., & Sivapalan, M. (2016). Dominant flood generating mechanisms across the united states. *Geophysical Research Letters*, 43(9), 4382–4390.
- Blake, E. S., & Zelinsky, D. A. (2018). National hurricane center tropical cyclone report: Hurricane harvey. *National Hurricane Center, National Oceanographic and Atmospheric Association*.
- Brooks, H. E., & Stensrud, D. J. (2000). Climatology of heavy rain events in the united states from

- hourly precipitation observations. *Monthly Weather Review*, 128(4), 1194–1201.
- Caracena, F., & Fritsch, J. (1983). Focusing mechanisms in the texas hill country flash floods of 1978. *Monthly weather review*, 111(12), 2319–2332.
- Caracena, F., Maddox, R. A., Hoxit, L. R., & Chappell, C. F. (1979). Mesoanalysis of the big thompson storm. *Monthly Weather Review*, 107(1), 1–17.
- Chen, J., Dai, A., Zhang, Y., & Rasmussen, K. L. (2020). Changes in convective available potential energy and convective inhibition under global warming. *Journal of Climate*, 33(6), 2025–2050.
- Corringham, T. W., Ralph, F. M., Gershunov, A., Cayan, D. R., & Talbot, C. A. (2019). Atmospheric rivers drive flood damages in the western united states. *Science Advances*, 5(12), eaax4631.
- Dai, A., Rasmussen, R. M., Liu, C., Ikeda, K., & Prein, A. F. (2017). A new mechanism for warm-season precipitation response to global warming based on convection-permitting simulations. *Climate Dynamics*, 1–26.
- Daly, C., Halbleib, M., Smith, J. I., Gibson, W. P., Doggett, M. K., Taylor, G. H., . . . Pasteris, P. P. (2008). Physiographically sensitive mapping of climatological temperature and precipitation across the conterminous united states. *International Journal of Climatology: a Journal of the Royal Meteorological Society*, 28(15), 2031–2064.
- Daly, C., Neilson, R. P., & Phillips, D. L. (1994). A statistical-topographic model for mapping climatological precipitation over mountainous terrain. *Journal of applied meteorology*, 33(2), 140–158.
- Das, T., Dettinger, M. D., Cayan, D. R., & Hidalgo, H. G. (2011). Potential increase in floods in california’s sierra nevada under future climate projections. *Climatic Change*, 109(1), 71–94.
- Davenport, F. V., Herrera-Estrada, J. E., Burke, M., & Diffenbaugh, N. S. (2020). Flood size increases nonlinearly across the western united states in response to lower snow-precipitation ratios. *Water Resources Research*, 56(1), e2019WR025571.
- Davis, R. S. (2001). Flash flood forecast and detection methods. In *Severe convective storms* (pp.

- 481–525). Springer.
- Demuth, J. L., DeMaria, M., & Knaff, J. A. (2006). Improvement of advanced microwave sounding unit tropical cyclone intensity and size estimation algorithms. *Journal of applied meteorology and climatology*, *45*(11), 1573–1581.
- Dettinger, M. (2011b). Climate change, atmospheric rivers, and floods in california—a multimodel analysis of storm frequency and magnitude changes 1. *JAWRA Journal of the American Water Resources Association*, *47*(3), 514–523.
- Dettinger, M. D., Ralph, F. M., Das, T., Neiman, P. J., & Cayan, D. R. (2011a). Atmospheric rivers, floods and the water resources of california. *Water*, *3*(2), 445–478.
- Donegan, B. (2019). *2019 mississippi river flood the longest-lasting since the great flood of 1927*. https://weather.com/news/weather/news/2019-05-14-one-of-longest-livedmississippi-river-floods-since-great-flood-1927?cm_ven=wu_videos?cm_ven=hp-slot-2.
- Doswell, C. A. I., Brooks, H. E., & Maddox, R. A. (1996). Flash flood forecasting: An ingredients-based methodology. *Weather and Forecasting*, *11*(4), 560–581.
- Dougherty, E., & Rasmussen, K. L. (2019). Climatology of flood-producing storms and their associated rainfall characteristics in the united states. *Monthly Weather Review*, *147*(11), 3861–3877.
- Ferguson, A. P., & Ashley, W. S. (2017). Spatiotemporal analysis of residential flood exposure in the atlanta, georgia metropolitan area. *Natural Hazards*, *87*(2), 989–1016.
- Feser, F., Rockel, B., von Storch, H., Winterfeldt, J., & Zahn, M. (2011). Regional climate models add value to global model data: a review and selected examples. *Bulletin of the American Meteorological Society*, *92*(9), 1181–1192.
- Frans, C., Istanbuloglu, E., Mishra, V., Munoz-Arriola, F., & Lettenmaier, D. P. (2013). Are climatic or land cover changes the dominant cause of runoff trends in the upper mississippi river basin? *Geophysical Research Letters*, *40*(6), 1104–1110.
- Freeman, A. C., & Ashley, W. S. (2017). Changes in the us hurricane disaster landscape: the

- relationship between risk and exposure. *Natural hazards*, 88(2), 659–682.
- Fritsch, J., Kane, R., & Chelius, C. (1986). The contribution of mesoscale convective weather systems to the warm-season precipitation in the united states. *Journal of climate and applied meteorology*, 25(10), 1333–1345.
- Fritsch, J. M., & Carbone, R. (2004). Improving quantitative precipitation forecasts in the warm season: A uswrp research and development strategy. *Bulletin of the American Meteorological Society*, 85(7), 955–966.
- Funk, T. W. (1991). Forecasting techniques utilized by the forecast branch of the national meteorological center during a major convective rainfall event. *Weather and forecasting*, 6(4), 548–564.
- Gao, Y., Lu, J., Leung, L. R., Yang, Q., Hagos, S., & Qian, Y. (2015). Dynamical and thermodynamical modulations on future changes of landfalling atmospheric rivers over western north america. *Geophysical Research Letters*, 42(17), 7179–7186.
- Gochis, D., Schumacher, R., Friedrich, K., Doesken, N., Kelsch, M., Sun, J., . . . others (2015). The great colorado flood of september 2013. *Bulletin of the American Meteorological Society*, 96(9), 1461–1487.
- Gourley, J. J., Hong, Y., Flamig, Z. L., Arthur, A., Clark, R., Calianno, M., . . . others (2013). A unified flash flood database across the united states. *Bulletin of the American Meteorological Society*, 94(6), 799–805.
- Grabowski, W. W., & Prein, A. F. (2019). Separating dynamic and thermodynamic impacts of climate change on daytime convective development over land. *Journal of Climate*, 32(16), 5213–5234.
- Guan, B., Molotch, N. P., Waliser, D. E., Fetzer, E. J., & Neiman, P. J. (2010). Extreme snowfall events linked to atmospheric rivers and surface air temperature via satellite measurements. *Geophysical Research Letters*, 37(20).
- Gutmann, E. D., Rasmussen, R. M., Liu, C., Ikeda, K., Bruyere, C. L., Done, J. M., . . . Veldore, V. (2018). Changes in hurricanes from a 13-yr convection-permitting pseudo–global warming

- simulation. *Journal of Climate*, 31(9), 3643–3657.
- Hagos, S. M., Leung, L. R., Yoon, J.-H., Lu, J., & Gao, Y. (2016). A projection of changes in land-falling atmospheric river frequency and extreme precipitation over western north america from the large ensemble cesm simulations. *Geophysical Research Letters*, 43(3), 1357–1363.
- Hatchett, B. J., Daudert, B., Garner, C. B., Oakley, N. S., Putnam, A. E., & White, A. B. (2017). Winter snow level rise in the northern sierra nevada from 2008 to 2017. *Water*, 9(11), 899.
- Held, I. M., & Soden, B. J. (2006). Robust responses of the hydrological cycle to global warming. *Journal of climate*, 19(21), 5686–5699.
- Herman, G. R., & Schumacher, R. S. (2018a). Flash flood verification: Pondering precipitation proxies. *Journal of Hydrometeorology*, 19(11), 1753–1776.
- Herman, G. R., & Schumacher, R. S. (2018b). Money doesn't grow on trees, but forecasts do: Forecasting extreme precipitation with random forests. *Monthly Weather Review*, 146(5), 1571–1600.
- Hirabayashi, Y., Mahendran, R., Koirala, S., Konoshima, L., Yamazaki, D., Watanabe, S., ... Kanae, S. (2013). Global flood risk under climate change. *Nature Climate Change*, 3(9), 816–821.
- Hong, S.-Y., Noh, Y., & Dudhia, J. (2006). A new vertical diffusion package with an explicit treatment of entrainment processes. *Monthly weather review*, 134(9), 2318–2341.
- Hoogewind, K. A., Baldwin, M. E., & Trapp, R. J. (2017). The impact of climate change on hazardous convective weather in the united states: Insight from high-resolution dynamical downscaling. *Journal of Climate*, 30(24), 10081–10100.
- Houze Jr, R., McMurdie, L., Rasmussen, K., Kumar, A., & Chaplin, M. (2017). Multiscale aspects of the storm producing the june 2013 flooding in uttarakhand, india. *Monthly Weather Review*, 145(11), 4447–4466.
- Houze Jr, R., Rasmussen, K., Medina, S., Brodzik, S., & Romatschke, U. (2011). Anomalous atmospheric events leading to the summer 2010 floods in pakistan. *Bulletin of the American*

- Meteorological Society*, 92(3), 291–298.
- Houze Jr, R. A. (2004). Mesoscale convective systems. *Reviews of Geophysics*, 42(4).
- Huang, X., Hall, A. D., & Berg, N. (2018). Anthropogenic warming impacts on today's sierra nevada snowpack and flood risk. *Geophysical Research Letters*, 45(12), 6215–6222.
- Huang, X., Swain, D. L., Walton, D. B., Stevenson, S., & Hall, A. D. (2020). Simulating and evaluating atmospheric river-induced precipitation extremes along the us pacific coast: Case studies from 1980–2017. *Journal of Geophysical Research: Atmospheres*, 125(4), e2019JD031554.
- Iacono, M. J., Delamere, J. S., Mlawer, E. J., Shephard, M. W., Clough, S. A., & Collins, W. D. (2008). Radiative forcing by long-lived greenhouse gases: Calculations with the aer radiative transfer models. *Journal of Geophysical Research: Atmospheres*, 113(D13).
- Jha, M., Pan, Z., Takle, E. S., & Gu, R. (2004). Impacts of climate change on streamflow in the upper mississippi river basin: A regional climate model perspective. *Journal of Geophysical Research: Atmospheres*, 109(D9).
- Junker, N. W., Grumm, R. H., Hart, R., Bosart, L. F., Bell, K. M., & Pereira, F. J. (2008). Use of normalized anomaly fields to anticipate extreme rainfall in the mountains of northern california. *Weather and forecasting*, 23(3), 336–356.
- Kendon, E. J., Ban, N., Roberts, N. M., Fowler, H. J., Roberts, M. J., Chan, S. C., . . . Wilkinson, J. M. (2017). Do convection-permitting regional climate models improve projections of future precipitation change? *Bulletin of the American Meteorological Society*, 98(1), 79–93.
- Kendon, E. J., Roberts, N. M., Fowler, H. J., Roberts, M. J., Chan, S. C., & Senior, C. A. (2014). Heavier summer downpours with climate change revealed by weather forecast resolution model. *Nature Climate Change*, 4(7), 570–576.
- Kendon, E. J., Roberts, N. M., Senior, C. A., & Roberts, M. J. (2012). Realism of rainfall in a very high-resolution regional climate model. *Journal of Climate*, 25(17), 5791–5806.
- Kirtman, B., Power, S. B., Adedoyin, A. J., Boer, G. J., Bojariu, R., Camilloni, I., . . . others (2013).

Near-term climate change: projections and predictability.

- Kumar, A., Houze Jr, R. A., Rasmussen, K. L., & Peters-Lidard, C. (2014). Simulation of a flash flooding storm at the steep edge of the himalayas. *Journal of Hydrometeorology*, *15*(1), 212–228.
- Kunkel, K. E., Easterling, D. R., Kristovich, D. A., Gleason, B., Stoecker, L., & Smith, R. (2012). Meteorological causes of the secular variations in observed extreme precipitation events for the conterminous united states. *Journal of Hydrometeorology*, *13*(3), 1131–1141.
- Lackmann, G. M. (2013). The south-central us flood of may 2010: Present and future. *Journal of Climate*, *26*(13), 4688–4709.
- Lehner, F., Wahl, E. R., Wood, A. W., Blatchford, D. B., & Llewellyn, D. (2017). Assessing recent declines in upper rio grande runoff efficiency from a paleoclimate perspective. *Geophysical Research Letters*, *44*(9), 4124–4133.
- Lin, Y., & Mitchell, K. E. (2005). 1.2 the ncep stage ii/iv hourly precipitation analyses: Development and applications. In *19th conf. hydrology, american meteorological society, san diego, ca, usa*.
- Liu, C., Ikeda, K., Rasmussen, R., Barlage, M., Newman, A. J., Prein, A. F., ... others (2017). Continental-scale convection-permitting modeling of the current and future climate of north america. *Climate Dynamics*, *49*(1-2), 71–95.
- Lorente-Plazas, R., Mitchell, T. P., Mauger, G., & Salathé Jr, E. P. (2018). Local enhancement of extreme precipitation during atmospheric rivers as simulated in a regional climate model. *Journal of Hydrometeorology*, *19*(9), 1429–1446.
- Maddox, R. A., Canova, F., & Hoxit, L. R. (1980). Meteorological characteristics of flash flood events over the western united states. *Monthly Weather Review*, *108*(11), 1866–1877.
- Maddox, R. A., Chappell, C. F., & Hoxit, L. R. (1979). Synoptic and meso- α scale aspects of flash flood events. *Bulletin of the American Meteorological Society*, *60*(2), 115–123.
- Maddox, R. A., Hoxit, L. R., Chappell, C. F., & Caracena, F. (1978). Comparison of meteorological aspects of the big thompson and rapid city flash floods. *Monthly Weather Review*, *106*(3),

375–389.

- Mahoney, K., Swales, D., Mueller, M. J., Alexander, M., Hughes, M., & Malloy, K. (2018). An examination of an inland-penetrating atmospheric river flood event under potential future thermodynamic conditions. *Journal of Climate*, *31*(16), 6281–6297.
- Mallakpour, I., & Villarini, G. (2015). The changing nature of flooding across the central united states. *Nature Climate Change*, *5*(3), 250–254.
- McCabe, G. J., Clark, M. P., & Hay, L. E. (2007). Rain-on-snow events in the western united states. *Bulletin of the American Meteorological Society*, *88*(3), 319–328.
- Mei, Y., & Anagnostou, E. N. (2015). A hydrograph separation method based on information from rainfall and runoff records. *Journal of Hydrology*, *523*, 636–649.
- Michaud, J. D., Hirschboeck, K. K., & Winchell, M. (2001). Regional variations in small-basin floods in the united states. *Water Resources Research*, *37*(5), 1405–1416.
- Moore, B. J., Neiman, P. J., Ralph, F. M., & Barthold, F. E. (2012). Physical processes associated with heavy flooding rainfall in nashville, tennessee, and vicinity during 1–2 may 2010: The role of an atmospheric river and mesoscale convective systems. *Monthly Weather Review*, *140*(2), 358–378.
- Musselman, K. N., Lehner, F., Ikeda, K., Clark, M. P., Prein, A. F., Liu, C., . . . Rasmussen, R. (2018). Projected increases and shifts in rain-on-snow flood risk over western north america. *Nature Climate Change*, *8*(9), 808–812.
- Neiman, P. J., Martin Ralph, F., Persson, P. O. G., White, A. B., Jorgensen, D. P., & Kingsmill, D. E. (2004). Modification of fronts and precipitation by coastal blocking during an intense landfalling winter storm in southern california: Observations during caljet. *Monthly weather review*, *132*(1), 242–273.
- Neiman, P. J., Ralph, F. M., Moore, B. J., Hughes, M., Mahoney, K. M., Cordeira, J. M., & Dettinger, M. D. (2013). The landfall and inland penetration of a flood-producing atmospheric river in arizona. part i: Observed synoptic-scale, orographic, and hydrometeorological characteristics. *Journal of Hydrometeorology*, *14*(2), 460–484.

- Neiman, P. J., Ralph, F. M., White, A., Kingsmill, D., & Persson, P. (2002). The statistical relationship between upslope flow and rainfall in California's coastal mountains: Observations during CalJET. *Monthly Weather Review*, *130*(6), 1468–1492.
- Neiman, P. J., Ralph, F. M., Wick, G. A., Lundquist, J. D., & Dettinger, M. D. (2008). Meteorological characteristics and overland precipitation impacts of atmospheric rivers affecting the west coast of North America based on eight years of SSM/I satellite observations. *Journal of Hydrometeorology*, *9*(1), 22–47.
- Nelson, B. R., Prat, O. P., Seo, D.-J., & Habib, E. (2016). Assessment and implications of NCEP Stage IV quantitative precipitation estimates for product intercomparisons. *Weather and Forecasting*, *31*(2), 371–394.
- NHC. (2018). *National hurricane center tropical cyclone report: Hurricane Harvey*. https://www.nhc.noaa.gov/data/tcr/AL092017_Harvey.pdf.
- Nielsen, E. R., Herman, G. R., Tournay, R. C., Peters, J. M., & Schumacher, R. S. (2015). Double impact: When both tornadoes and flash floods threaten the same place at the same time. *Weather and Forecasting*, *30*(6), 1673–1693.
- Nielsen, E. R., & Schumacher, R. S. (2018). Dynamical insights into extreme short-term precipitation associated with supercells and mesovortices. *Journal of the Atmospheric Sciences*, *75*(9), 2983–3009.
- Nielsen, E. R., Schumacher, R. S., & Kecklik, A. M. (2016). The effect of the Balcones escarpment on three cases of extreme precipitation in central Texas. *Monthly Weather Review*, *144*(1), 119–138.
- Niu, G.-Y., Yang, Z.-L., Mitchell, K. E., Chen, F., Ek, M. B., Barlage, M., ... others (2011). The community Noah land surface model with multiparameterization options (Noah-MP): 1. Model description and evaluation with local-scale measurements. *Journal of Geophysical Research: Atmospheres*, *116*(D12).
- NOAA. (2019). *National center for environmental information*. <https://www.ncdc.noaa.gov/stormevents/>.

- Nowak, K., Hoerling, M., Rajagopalan, B., & Zagona, E. (2012). Colorado river basin hydroclimatic variability. *Journal of Climate*, 25(12), 4389–4403.
- NWS. (2007). *National weather service instruction 10-1605: Storm data preparation*. <http://www.nws.noaa.gov/directives/>.
- NWS. (2011). *Record floods of greater nashville: Including flooding in middle tennessee and western kentucky, may 1–4, 2010*. https://www.nws.noaa.gov/os/assessments/pdfs/Tenn_flooding.pdf.
- NWS. (2019). *Spring flooding summary 2019*. https://www.weather.gov/dvn/summary_SpringFlooding_2019.
- NWS St. Louis, MO. (2019). *Significant weather event reviews: Flood event march 2008*. <https://www.weather.gov/lx/events>.
- of Engineers, U. A. C. (n.d.). *The willamette valley project*. <https://www.nwp.usace.army.mil/Locations/Willamette-Valley/>.
- Padrón, R. S., Gudmundsson, L., Greve, P., & Seneviratne, S. I. (2017). Large-scale controls of the surface water balance over land: Insights from a systematic review and meta-analysis. *Water Resources Research*, 53(11), 9659–9678.
- Prein, A. F., Langhans, W., Fosser, G., Ferrone, A., Ban, N., Goergen, K., ... others (2015). A review on regional convection-permitting climate modeling: Demonstrations, prospects, and challenges. *Reviews of geophysics*, 53(2), 323–361.
- Prein, A. F., Liu, C., Ikeda, K., Bullock, R., Rasmussen, R. M., Holland, G. J., & Clark, M. (2017b). Simulating north american mesoscale convective systems with a convection-permitting climate model. *Climate Dynamics*, 1–16.
- Prein, A. F., Liu, C., Ikeda, K., Trier, S. B., Rasmussen, R. M., Holland, G. J., & Clark, M. P. (2017c). Increased rainfall volume from future convective storms in the us. *Nature Climate Change*, 7(12), 880–884.
- Prein, A. F., Rasmussen, R. M., Ikeda, K., Liu, C., Clark, M. P., & Holland, G. J. (2017a). The future intensification of hourly precipitation extremes. *Nature Climate Change*, 7(1), 48–52.

- Qiang, Y., Lam, N. S., Cai, H., & Zou, L. (2017). Changes in exposure to flood hazards in the united states. *Annals of the American Association of Geographers*, 107(6), 1332–1350.
- Ralph, F., Coleman, T., Neiman, P., Zamora, R., & Dettinger, M. (2013). Observed impacts of duration and seasonality of atmospheric-river landfalls on soil moisture and runoff in coastal northern california. *Journal of Hydrometeorology*, 14(2), 443–459.
- Ralph, F., & Dettinger, M. (2012). Historical and national perspectives on extreme west coast precipitation associated with atmospheric rivers during december 2010. *Bulletin of the American Meteorological Society*, 93(6), 783–790.
- Ralph, F., Neiman, P. J., Wick, G. A., Gutman, S. I., Dettinger, M. D., Cayan, D. R., & White, A. B. (2006). Flooding on california's russian river: Role of atmospheric rivers. *Geophysical Research Letters*, 33(13).
- Ralph, F. M., Neiman, P. J., Kiladis, G. N., Weickmann, K., & Reynolds, D. W. (2010). A multi-scale observational case study of a pacific atmospheric river exhibiting tropical-extratropical connections and a mesoscale frontal wave. *Monthly Weather Review*.
- Ralph, F. M., Rutz, J. J., Cordeira, J. M., Dettinger, M., Anderson, M., Reynolds, D., . . . Smallcomb, C. (2019). A scale to characterize the strength and impacts of atmospheric rivers. *Bulletin of the American Meteorological Society*, 100(2), 269–289.
- Rasmussen, K. L., Chaplin, M., Zuluaga, M., & Houze Jr, R. (2016). Contribution of extreme convective storms to rainfall in south america. *Journal of Hydrometeorology*, 17(1), 353–367.
- Rasmussen, K. L., & Houze Jr, R. A. (2012). A flash-flooding storm at the steep edge of high terrain: disaster in the himalayas. *Bulletin of the American Meteorological Society*, 93(11), 1713–1724.
- Rasmussen, K. L., Prein, A. F., Rasmussen, R. M., Ikeda, K., & Liu, C. (2017). Changes in the convective population and thermodynamic environments in convection-permitting regional climate simulations over the united states. *Climate Dynamics*, 1–26.
- Rasmussen, R., Ikeda, K., Liu, C., Gochis, D., Clark, M., Dai, A., . . . others (2014). Climate

- change impacts on the water balance of the colorado headwaters: high-resolution regional climate model simulations. *Journal of Hydrometeorology*, 15(3), 1091–1116.
- Rasmussen, R., Liu, C., Ikeda, K., Gochis, D., Yates, D., Chen, F., ... others (2011). High-resolution coupled climate runoff simulations of seasonal snowfall over colorado: a process study of current and warmer climate. *Journal of Climate*, 24(12), 3015–3048.
- Rienecker, M. M., Suarez, M. J., Gelaro, R., Todling, R., Bacmeister, J., Liu, E., ... others (2011). Merra: Nasa's modern-era retrospective analysis for research and applications. *Journal of climate*, 24(14), 3624–3648.
- Robins, W. (2019). *Willamette river (essay)*. https://oregonencyclopedia.org/articles/willamette_river/#.XTYsF-JKgUG.
- Rutz, J. J., Steenburgh, W. J., & Ralph, F. M. (2014). Climatological characteristics of atmospheric rivers and their inland penetration over the western united states. *Monthly Weather Review*, 142(2), 905–921.
- Saharia, M., Kirstetter, P.-E., Vergara, H., Gourley, J. J., & Hong, Y. (2017b). Characterization of floods in the united states. *Journal of hydrology*, 548, 524–535.
- Saharia, M., Kirstetter, P.-E., Vergara, H., Gourley, J. J., Hong, Y., & Giroud, M. (2017a). Mapping flash flood severity in the united states. *Journal of Hydrometeorology*, 18(2), 397–411.
- Schär, C., Ban, N., Fischer, E. M., Rajczak, J., Schmidli, J., Frei, C., ... others (2016). Percentile indices for assessing changes in heavy precipitation events. *Climatic Change*, 137(1-2), 201–216.
- Schär, C., Frei, C., Lüthi, D., & Davies, H. C. (1996). Surrogate climate-change scenarios for regional climate models. *Geophysical Research Letters*, 23(6), 669–672.
- Schroeder, A., Basara, J., Shepherd, J. M., & Nelson, S. (2016b). Insights into atmospheric contributors to urban flash flooding across the united states using an analysis of rawinsonde data and associated calculated parameters. *Journal of Applied Meteorology and Climatology*, 55(2), 313–323.
- Schroeder, A. J., Gourley, J. J., Hardy, J., Henderson, J. J., Parhi, P., Rahmani, V., ... Taraldsen,

- M. J. (2016a). The development of a flash flood severity index. *Journal of Hydrology*, *541*, 523–532.
- Schumacher, R. S. (2009). Mechanisms for quasi-stationary behavior in simulated heavy-rain-producing convective systems. *Journal of the atmospheric sciences*, *66*(6), 1543–1568.
- Schumacher, R. S., Clark, A. J., Xue, M., & Kong, F. (2013). Factors influencing the development and maintenance of nocturnal heavy-rain-producing convective systems in a storm-scale ensemble. *Monthly weather review*, *141*(8), 2778–2801.
- Schumacher, R. S., & Johnson, R. H. (2005). Organization and environmental properties of extreme-rain-producing mesoscale convective systems. *Monthly weather review*, *133*(4), 961–976.
- Schumacher, R. S., & Johnson, R. H. (2006). Characteristics of us extreme rain events during 1999–2003. *Weather and Forecasting*, *21*(1), 69–85.
- Schumacher, R. S., & Johnson, R. H. (2008). Mesoscale processes contributing to extreme rainfall in a midlatitude warm-season flash flood. *Monthly Weather Review*, *136*(10), 3964–3986.
- Schumacher, R. S., & Johnson, R. H. (2009). Quasi-stationary, extreme-rain-producing convective systems associated with midlevel cyclonic circulations. *Weather and forecasting*, *24*(2), 555–574.
- Schwartz, M., Hall, A., Sun, F., Walton, D., & Berg, N. (2017). Significant and inevitable end-of-twenty-first-century advances in surface runoff timing in california’s sierra nevada. *Journal of Hydrometeorology*, *18*(12), 3181–3197.
- Shearman, J. O. (1976). *Reservoir-system model for the willamette river basin, oregon*. US Department of Interior, Geological Survey.
- Shen, X., Mei, Y., & Anagnostou, E. N. (2017). A comprehensive database of flood events in the contiguous united states from 2002 to 2013. *Bulletin of the American Meteorological Society*, *98*(7), 1493–1502.
- Shields, C. A., Rutz, J. J., Leung, L.-Y., Ralph, F. M., Wehner, M., Kawzenuk, B., ... others (2018). Atmospheric river tracking method intercomparison project (artmip): project

- goals and experimental design. *Geoscientific Model Development (Online)*, 11(PNNL-SA-130655).
- Slater, L. J., & Villarini, G. (2016). Recent trends in us flood risk. *Geophysical Research Letters*, 43(24), 12–428.
- Smith, A. B. (2019). *2018's billion dollar disasters in context*. <https://www.climate.gov/news-features/blogs/beyond-data/2018s-billion-dollar-disasters-context>.
- Smith, B. K., & Smith, J. A. (2015). The flashiest watersheds in the contiguous united states. *Journal of Hydrometeorology*, 16(6), 2365–2381.
- Smith, J. A., Baeck, M. L., Morrison, J. E., & Sturdevant-Rees, P. (2000). Catastrophic rainfall and flooding in texas. *Journal of Hydrometeorology*, 1(1), 5–25.
- Stephens, E., Day, J. J., Pappenberger, F., & Cloke, H. (2015). Precipitation and floodiness. *Geophysical Research Letters*, 42(23), 10–316.
- Stevenson, S. N., & Schumacher, R. S. (2014). A 10-year survey of extreme rainfall events in the central and eastern united states using gridded multisensor precipitation analyses. *Monthly Weather Review*, 142(9), 3147–3162.
- Sukovich, E. M., Ralph, F. M., Barthold, F. E., Reynolds, D. W., & Novak, D. R. (2014). Extreme quantitative precipitation forecast performance at the weather prediction center from 2001 to 2011. *Weather and forecasting*, 29(4), 894–911.
- Tan, J., Jakob, C., Rossow, W. B., & Tselioudis, G. (2015). Increases in tropical rainfall driven by changes in frequency of organized deep convection. *Nature*, 519(7544), 451–454.
- Thompson, G., & Eidhammer, T. (2014). A study of aerosol impacts on clouds and precipitation development in a large winter cyclone. *Journal of the atmospheric sciences*, 71(10), 3636–3658.
- Trapp, R. J., Hoogewind, K. A., & Lasher-Trapp, S. (2019). Future changes in hail occurrence in the united states determined through convection-permitting dynamical downscaling. *Journal of Climate*, 32(17), 5493–5509.

- Trenberth, K. E. (1999). Conceptual framework for changes of extremes of the hydrological cycle with climate change. In *Weather and climate extremes* (pp. 327–339). Springer.
- Trenberth, K. E., Dai, A., Rasmussen, R. M., & Parsons, D. B. (2003). The changing character of precipitation. *Bulletin of the American Meteorological Society*, *84*(9), 1205–1218.
- Trigg, M., Birch, C., Neal, J., Bates, P., Smith, A., Sampson, C., . . . others (2016). The credibility challenge for global fluvial flood risk analysis. *Environmental Research Letters*, *11*(9), 094014.
- Van der Wiel, K., Kapnick, S. B., Vecchi, G. A., Smith, J. A., Milly, P. C., & Jia, L. (2018). 100-year lower mississippi floods in a global climate model: characteristics and future changes. *Journal of Hydrometeorology*, *19*(10), 1547–1563.
- Vano, J. A., Miller, K., Dettinger, M. D., Cifelli, R., Curtis, D., Dufour, A., . . . Wilson, A. M. (2019). Hydroclimatic extremes as challenges for the water management community: Lessons from oroville dam and hurricane harvey. *Bulletin of the American Meteorological Society*, *100*(1), S9–S14.
- Villarini, G. (2016). On the seasonality of flooding across the continental united states. *Advances in Water Resources*, *87*, 80–91.
- Villarini, G., Goska, R., Smith, J. A., & Vecchi, G. A. (2014). North atlantic tropical cyclones and us flooding. *Bulletin of the American Meteorological Society*, *95*(9), 1381–1388.
- Villarini, G., & Slater, L. J. (2018). Examination of changes in annual maximum gauge height in the continental united states using quantile regression. *Journal of Hydrologic Engineering*, *23*(3), 06017010.
- Wang, Z., Bovik, A. C., Sheikh, H. R., & Simoncelli, E. P. (2004). Image quality assessment: from error visibility to structural similarity. *IEEE transactions on image processing*, *13*(4), 600–612.
- White, A. B., Moore, B. J., Gottas, D. J., & Neiman, P. J. (2019). Winter storm conditions leading to excessive runoff above california’s oroville dam during january and february 2017. *Bulletin of the American Meteorological Society*, *100*(1), 55–70.

- Wing, O. E., Bates, P. D., Smith, A. M., Sampson, C. C., Johnson, K. A., Fargione, J., & Morefield, P. (2018). Estimates of present and future flood risk in the conterminous united states. *Environmental Research Letters*, *13*(3), 034023.
- Woodhouse, C. A., & Pederson, G. T. (2018). Investigating runoff efficiency in upper colorado river streamflow over past centuries. *Water Resources Research*, *54*(1), 286–300.
- Young, A. M., Skelly, K. T., & Cordeira, J. M. (2017). High-impact hydrologic events and atmospheric rivers in california: An investigation using the ncei storm events database. *Geophysical Research Letters*, *44*(7), 3393–3401.